

Washington University in St. Louis

## Washington University Open Scholarship

---

Arts & Sciences Electronic Theses and  
Dissertations

Arts & Sciences

---

Winter 12-15-2015

### Solid-State NMR Study of the Tertiary Structure of the Peptidoglycan of *Enterococcus faecalis* and the Structures of Phorbol Diacetate and Bryostatin Bound to Protein Kinase C $\delta$ C1b Domain

Hao Yang

*Washington University in St. Louis*

Follow this and additional works at: [https://openscholarship.wustl.edu/art\\_sci\\_etds](https://openscholarship.wustl.edu/art_sci_etds)

---

#### Recommended Citation

Yang, Hao, "Solid-State NMR Study of the Tertiary Structure of the Peptidoglycan of *Enterococcus faecalis* and the Structures of Phorbol Diacetate and Bryostatin Bound to Protein Kinase C $\delta$  C1b Domain" (2015).

*Arts & Sciences Electronic Theses and Dissertations*. 693.

[https://openscholarship.wustl.edu/art\\_sci\\_etds/693](https://openscholarship.wustl.edu/art_sci_etds/693)

This Dissertation is brought to you for free and open access by the Arts & Sciences at Washington University Open Scholarship. It has been accepted for inclusion in Arts & Sciences Electronic Theses and Dissertations by an authorized administrator of Washington University Open Scholarship. For more information, please contact [digital@wumail.wustl.edu](mailto:digital@wumail.wustl.edu).

WASHINGTON UNIVERSITY IN ST. LOUIS

Department of Chemistry

Dissertation Examination Committee:

Jacob Schaefer, Chair

Sophia Hayes

Richard Loomis

Garland Marshall

Jay Ponder

Solid-State NMR Study of the Tertiary Structure of the Peptidoglycan of *Enterococcus faecalis*  
and the Structures of Phorbol Diacetate and Bryostatin Bound to Protein Kinase C $\delta$  C1b Domain

by

Hao Yang

A dissertation presented to the  
Graduate School of Arts & Sciences  
of Washington University in  
partial fulfillment of the  
requirements for the degree  
of Doctor of Philosophy

December 2015  
St. Louis, Missouri

© 2015, Hao Yang

# Table of Contents

List of Figures .....	v
List of Tables .....	x
Acknowledgments.....	xi
Abstract.....	xv
Chapter 1: Basic Concepts .....	1
1.1 Cross Polarization .....	1
1.2 Magic Angle Spinning .....	4
1.2.1 MAS Averages Dipolar Couplings to Zero .....	5
1.2.2 MAS Averages First Order Quadrupolar Couplings to Zero.....	7
1.2.3 MAS Averages CSA to Isotropic Value.....	8
1.3 CPMAS .....	11
1.4 Rotational-Echo Double-Resonance (REDOR).....	12
1.5 References .....	19
Chapter 2: Solid-State NMR Study of the Structures of Phorbol Diacetate and Bryostatin Bound to PKC $\delta$ C1b Domain .....	21
2.1 Introduction .....	21
2.2 Materials and Methods .....	26
2.2.1 NMR Sample Preparation .....	26
2.2.2 Solid-State NMR Experiments .....	27
2.2.3 REDOR Calculations .....	27

2.3	Results and Discussion for Phorbol Diacetate .....	30
2.3.1	Design of [ <sup>13</sup> C, <sup>2</sup> H <sub>3</sub> ]Phorbol-12, 13-Diacetate for REDOR Analysis .....	30
2.3.2	Preparation and NMR Characterization of Ligand-Bound PKCδ C1b in a Membrane Microenvironment .....	31
2.3.3	The <sup>13</sup> C-CD <sub>3</sub> Distance Determination for PKC-Bound [ <sup>13</sup> C, <sup>2</sup> H <sub>3</sub> ]Phorbol-12, 13- Diacetate.....	34
2.3.4	Partitioning of [ <sup>13</sup> C, <sup>2</sup> H <sub>3</sub> ]Phorbol-12, 13-Diacetate into a Mobile Phase.....	37
2.3.5	Conclusion for Phorbol Diacetate .....	40
2.4	Results and Discussion for Bryostatin .....	41
2.4.1	Introduction to Bryostatin .....	41
2.4.2	Bryostatin is Predominantly Immobile .....	43
2.4.3	The <sup>19</sup> F-CD <sub>3</sub> Distance Determination for PKC-Bound [ <sup>19</sup> F, <sup>13</sup> C, <sup>2</sup> H <sub>3</sub> ]Bryostatin.....	44
2.4.4	The <sup>19</sup> F- <sup>13</sup> C Distance Determination for PKC-Bound [ <sup>19</sup> F, <sup>13</sup> C, <sup>2</sup> H <sub>3</sub> ]Bryostatin.....	46
2.4.5	The <sup>13</sup> C-CD <sub>3</sub> Distance Determination for PKC-Bound [ <sup>19</sup> F, <sup>13</sup> C, <sup>2</sup> H <sub>3</sub> ]Bryostatin.....	48
2.4.6	Conclusion for Bryostatin .....	50
2.5	References .....	52
Chapter 3: Characterization of the Peptidoglycan Tertiary Structures of <i>E. faecalis</i> .....		61
3.1	Introduction .....	61
3.2	Materials and Methods.....	65
3.2.1	Preparation of <i>E. faecalis</i> Whole-Cell Samples .....	65
3.2.2	Cell-Wall Isolation.....	67
3.2.3	Solid-State NMR Spectrometer and Dante-Select Spin-Diffusion Pulse Sequence .....	69
3.3	Results and Discussion.....	71

3.3.1	<i>E. faecalis</i> Growth with Alaphosphin.....	71
3.3.2	Solid-State NMR Characterization of <i>E. faecalis</i> PG Tertiary Structue .....	76
3.4	Conclusion.....	92
3.5	References .....	95
Chapter 4: Reversible CO <sub>2</sub> Capture Mechanism of a Humidity-Swing Polymeric Sorbent.....		99
4.1	Introduction .....	99
4.2	Materials and Methods .....	105
4.2.1	The Polymeric Sorbent.....	105
4.2.2	Solid-State NMR Experiments.....	105
4.3	Results and Discussion.....	107
4.4	Conclusion.....	115
4.5	References .....	116

# List of Figures

Figure 1.1:	Pulse sequence for $^1\text{H}$ to $^{13}\text{C}$ CP and subsequent carbon detection .....	1
Figure 1.2:	I and S spins are spin-locked by $B_{1I}$ and $B_{1S}$ RF pulses on the xy-plane in the double rotating frame .....	2
Figure 1.3:	A rotor spinning at the magic angle ( $\theta_m$ ).....	4
Figure 1.4:	Relative positions of the rotor spinning axis, the internuclear vector, and the external magnetic field $B_0$ in the laboratory frame .....	5
Figure 1.5:	The relative positions of the rotor spinning axis, the internuclear vector, and the external magnetic field $B_0$ in the tilted laboratory frame .....	6
Figure 1.6:	The relative positions of the rotor spinning axis, the principal Z axis of the electric field gradient tensor, and the external magnetic field $B_0$ .....	8
Figure 1.7:	The relative positions of the rotor spinning axis, the principal X axis of the chemical shift tensor, and the external magnetic field $B_0$ .....	10
Figure 1.8:	The first CPMAS experiment.....	11
Figure 1.9:	A typical REDOR pulse sequence.....	13
Figure 1.10:	REDOR curves for a pair of dipolar-coupled $^{13}\text{C}$ - $^{19}\text{F}$ nuclei with an internuclear distance of 4 and 5 Å, respectively.....	14
Figure 1.11:	REDOR detection limits.....	14
Figure 1.12:	A single rotor cycle containing one dephasing pulse .....	16
Figure 1.13:	A simulation of REDOR dephasing as a function of $t_1$ , dipolar coupling constant ( $D$ ), and dephasing time .....	17

Figure 2.1:	(a) The domain composition of PKC isoforms. (b) The crystal structure of PKC $\theta$ C1b domain. (c) The model of PKC $\gamma$ C1b domain interacting with the activator DAG and phosphatidylserine (PS) in lipid bilayers .....	22
Figure 2.2:	The structure of some PKC activators.....	23
Figure 2.3:	[ $^{13}\text{C}$ , $^2\text{H}_3$ ]PDAc structure.....	26
Figure 2.4:	$^{13}\text{C}$ CPMAS echo spectrum of the [ $^{13}\text{C}$ , $^2\text{H}_3$ ]PDAc-PKC-lipid complex.....	33
Figure 2.5:	$160 T_r$ (22.4 ms) $^{13}\text{C}\{^2\text{H}\}$ REDOR $S_0$ spectra of [ $^{13}\text{C}$ , $^2\text{H}_3$ ]PDAc-PKC-lipid complex and [ $^2\text{H}_3$ ]PDAc-PKC-lipid complex .....	34
Figure 2.6:	$160 T_r$ (22.4 ms) $^{13}\text{C}\{^2\text{H}\}$ REDOR spectra of [ $^{13}\text{C}$ , $^2\text{H}_3$ ]PDAc-PKC-lipid complex and [ $^2\text{H}_3$ ]PDAc-PKC-lipid complex.....	35
Figure 2.7:	$^{13}\text{C}\{^2\text{H}\}$ REDOR data points and fitting curve of [ $^{13}\text{C}$ , $^2\text{H}_3$ ]PDAc-PKC-lipid complex .....	36
Figure 2.8:	$^2\text{H}$ Hahn echo spectra of [ $^{13}\text{C}$ , $^2\text{H}_3$ ]PDAc-PKC-lipid complex .....	38
Figure 2.9:	The isotopically labeled bryostatin analogue for REDOR NMR studies.....	42
Figure 2.10:	The deuterium Hahn echo spectrum of [ $^{19}\text{F}$ , $^{13}\text{C}$ , $^2\text{H}_3$ ]bryostatin-PKC-lipid complex with 8 s recycle delay .....	43
Figure 2.11:	$^2\text{H}\{^{19}\text{F}\}$ REDOR spectra of [ $^{19}\text{F}$ , $^{13}\text{C}$ , $^2\text{H}_3$ ]bryostatin-PKC-lipid complex at $128 T_r$ (17.92 ms).....	44
Figure 2.12:	$^2\text{H}\{^{19}\text{F}\}$ REDOR data and fitting curves.....	45
Figure 2.13:	$^{13}\text{C}\{^{19}\text{F}\}$ REDOR spectra of [ $^{19}\text{F}$ , $^{13}\text{C}$ , $^2\text{H}_3$ ]bryostatin-PKC-lipid complex and [ $^2\text{H}_3$ ]PDAc-PKC-lipid complex at $128 T_r$ (17.92 ms).....	46
Figure 2.14:	$^{13}\text{C}\{^{19}\text{F}\}$ REDOR data and fitting curves.....	47

Figure 2.15:	$^{13}\text{C}\{^2\text{H}\}$ REDOR spectra of [ $^{19}\text{F}$ , $^{13}\text{C}$ , $^2\text{H}_3$ ]bryostatin-PKC-lipid complex and [ $^2\text{H}_3$ ]PDAC-PKC-lipid complex at 128 $T_r$ (17.92 ms) .....	48
Figure 2.16:	$^{13}\text{C}\{^2\text{H}\}$ REDOR data and fitting curves .....	49
Figure 2.17:	Distances between the spin pairs in [ $^{19}\text{F}$ , $^{13}\text{C}$ , $^2\text{H}_3$ ]bryostatin from modeling and REDOR measurements, respectively .....	51
Figure 3.1:	Transmission electron microscopy (TEM) of <i>E. faecalis</i> (ATCC 29212) .....	62
Figure 3.2:	Chemical structures of wall teichoic acid and peptidoglycan of <i>E. faecalis</i> .....	63
Figure 3.3:	Pulse sequence for determination of $^{13}\text{C}$ - $^{13}\text{C}$ proximities by spin diffusion .....	70
Figure 3.4:	<i>E. faecalis</i> growth curves in 100 ml of EDM with 10 $\mu\text{g}/\text{ml}$ alaphosphin at different concentrations of D-alanine .....	72
Figure 3.5:	Growth curves for <i>E. faecalis</i> with alaphosphin, sample #4 with alaphosphin and selectively isotopical labeled D-alanine, L-alanine, and L-lysine as shown in the figure, and <i>E. faecalis</i> without alaphosphin .....	75
Figure 3.6:	CPMAS $^{15}\text{N}$ NMR spectra of isolated cell walls of <i>E. faecalis</i> labeled by L- $[\epsilon$ - $^{15}\text{N}]$ lysine (sample #1) as a function of the proton-nitrogen contact time .....	77
Figure 3.7:	CPMAS $^{15}\text{N}$ NMR spectra of whole cells of <i>E. faecalis</i> labeled by L- $[1$ - $^{13}\text{C}]$ lysine and D- $^{15}\text{N}$ alanine (sample #2) before and after extraction by ethanol to remove low molecular-weight metabolites .....	78
Figure 3.8:	$\text{N}\{\text{C}\}$ REDOR $^{15}\text{N}$ NMR spectra of whole cells of <i>E. faecalis</i> labeled by L- $[1$ - $^{13}\text{C}]$ alanine, D- $[3$ - $^{13}\text{C}]$ alanine, and L- $[\epsilon$ - $^{15}\text{N}]$ lysine (sample #4) .....	80
Figure 3.9:	$\text{C}\{\text{N}\}$ REDOR $^{13}\text{C}$ NMR spectra of whole cells of <i>E. faecalis</i> labeled by L- $[1$ - $^{13}\text{C}]$ lysine and D- $^{15}\text{N}$ alanine (sample #2) .....	82

Figure 3.10: N{C} REDOR $^{15}\text{N}$ NMR spectra of cell walls of <i>E. faecalis</i> labeled by D-[1- $^{13}\text{C}$ ]alanine and L-[ $^{15}\text{N}$ ] alanine (sample #3) .....	84
Figure 3.11: C{N} REDOR $^{13}\text{C}$ NMR spectra of cell walls of <i>E. faecalis</i> labeled by D-[1- $^{13}\text{C}$ ]alanine and L-[ $^{15}\text{N}$ ]alanine (sample #3) .....	85
Figure 3.12: Dante difference $^{13}\text{C}$ NMR spectra of whole cells of <i>E. faecalis</i> labeled by L-[1- $^{13}\text{C}$ ]alanine, D-[3- $^{13}\text{C}$ ]alanine, and L-[ $\epsilon$ - $^{15}\text{N}$ ]lysine (sample #4) with and without 8 rotor periods of C{N} dipolar evolution following $^{13}\text{C}$ - $^{13}\text{C}$ spin diffusion.....	87
Figure 3.13: Dante difference $^{13}\text{C}$ NMR spectra of whole cells of <i>E. faecalis</i> labeled by L-[1- $^{13}\text{C}$ ]alanine, D-[3- $^{13}\text{C}$ ]alanine, and L-[ $\epsilon$ - $^{15}\text{N}$ ]lysine (sample #4) with and without 128 rotor periods of C{N} dipolar evolution following $^{13}\text{C}$ - $^{13}\text{C}$ spin diffusion.....	88
Figure 3.14: C{N} REDOR $^{13}\text{C}$ NMR spectra of whole cells of <i>E. faecalis</i> labeled by L-[1- $^{13}\text{C}$ ]alanine, D-[3- $^{13}\text{C}$ ]alanine, and L-[ $\epsilon$ - $^{15}\text{N}$ ]lysine (sample #4) after 8 and 128 rotor periods of $^{13}\text{C}$ - $^{15}\text{N}$ dipolar evolution .....	89
Figure 3.15: Double-difference C{N} REDOR $^{13}\text{C}$ NMR spectra of whole cells of <i>E. faecalis</i> labeled by L-[1- $^{13}\text{C}$ ]alanine, D-[3- $^{13}\text{C}$ ]alanine, and L-[ $\epsilon$ - $^{15}\text{N}$ ]lysine (sample #4) ..	91
Figure 3.16: Three-dimensional representation of the hybrid model for a short-bridge peptidoglycan lattice.....	92
Figure 3.17: Lattice model for the peptidoglycan of short-bridged <i>E. faecalis</i> .....	94
Figure 4.1: Atmospheric $\text{CO}_2$ concentration measured at Mauna Loa Observatory in Hawaii .....	100
Figure 4.2: 800,000 year record of atmospheric $\text{CO}_2$ concentration .....	101
Figure 4.3: The chemical structure of the sorbent's monomeric unit.....	103

Figure 4.4:	The scheme of the sorbent's CO <sub>2</sub> capture/release cycle driven by the humidity swing .....	104
Figure 4.5:	<sup>13</sup> C CPMAS echo spectra of the sorbent before and after the absorption of <sup>13</sup> CO <sub>2</sub> . Bubbling humidified N <sub>2</sub> gas through the <sup>13</sup> CO <sub>2</sub> absorbed sorbent for 25 minutes led to CO <sub>2</sub> desorption .....	108
Figure 4.6:	The pulse sequence of the <sup>13</sup> C CPMAS echo <sup>1</sup> H interrupted decoupling experiment .....	109
Figure 4.7:	<sup>13</sup> C CPMAS echo <sup>1</sup> H interrupted decoupling spectra of the <sup>13</sup> CO <sub>2</sub> absorbed sorbent and a NaHCO <sub>3</sub> standard with an interrupted decoupling duration of 80 μs .....	110
Figure 4.8:	<sup>13</sup> C{ <sup>15</sup> N} REDOR spectra of the <sup>13</sup> CO <sub>2</sub> absorbed sorbent with 4.48 ms dephasing time and ~ 200,000 scans .....	111
Figure 4.9:	The deuterium Hahn echo spectrum of the CO <sub>2</sub> desorbed sorbent .....	113
Figure 4.10:	The chemical equation of the sorbent's CO <sub>2</sub> capture/release cycle driven by the humidity swing .....	114
Figure 4.11:	The scheme of the CO <sub>2</sub> capture/release mechanism for the humidity-swing sorbent .....	114

# List of Tables

Table 2.1: REDOR analytical expressions for spin pairs containing spin-1 .....	28
Table 2.2: D <sub>3</sub> spin states .....	29
Table 3.1: The components of enterococcal defined media (EDM) on a per liter basis .....	66
Table 3.2: <i>E. faecalis</i> labeling strategy.....	73

# Acknowledgments

This dissertation could not have been completed without countless help from others. I considered myself extremely lucky when Jake offered me a place in his lab about six and a half years ago, likely as his last student. I have learned more than I could imagine in his lab: quantum theory, hardware, biochemistry, microbiology, polymers, *etc.* The discussions I've had with Jake over the years are invaluable. They were not only about my research specifically, but also about every aspect of science and the interconnections between seemingly unrelated science phenomenon. I especially enjoyed the science history stories from Jake. In addition to science, what influenced me most was his passion and devotion towards research, which demonstrates the old saying: actions speak louder than words. The years I spent in Schaefer Lab certainly prepared me to be a better scientist. Thank you Jake!

Manmilan is an important figure in our lab and not only because he makes all the figures. He is a true genius across the board, from computer programming to growing bacteria. His help to me over the years is countless, and I deeply appreciate it. Greg is our hardware and electronics specialist. He is very good at explaining formidable hardware concepts in an understandable way, helping me to become confident with the equipment. He has built many of our lab devices, and guided me through trouble-shooting hardware problems. I am very thankful for all of his help. My years in Schaefer Lab partially overlapped with Joon and Bobo. Joon is an expert on bacteria who offered me valuable advice on my research with bacterial cell walls. Bobo is a mathematics and computer genius who helped me a great deal with pulse programming and calculations in Mathematica. I am grateful for all their help.

I thank all of my collaborators. Professor Paul Wender and Professor Lynette Cegelski of Stanford University provided the isotopically labeled phorbol diacetate and bryostatin bound to protein kinase C in lipid bilayers. Professor Krzysztof Matyjaszewski and Professor Tomas Kowalewski at Carnegie Mellon University provided the CO<sub>2</sub> sorbent.

Washington University has a wonderful NMR community. I have greatly enjoyed my discussions with Professor Mark Conradi on spin physics. I also gained invaluable insights through conversations with my peers: Dustin, Andy, Jeremy, Sam, Chao, and many others. Special thanks are given to Sam Emery who strictly examined the English grammar of my dissertation.

I appreciate all the feedback and comments obtained from Professor Jay Ponder and Professor Richard Loomis at my committee meetings. They certainly improved this dissertation. I thank Professor Sophia Hayes and Professor Garland Marshall for serving on my defense committee, and for spending time to examine my work over the past six and a half years.

I am indebted to Dr. Ed Hiss and Rachel who helped me with various difficulties over the years. I thank Jimmy and Larry for machining parts for us, Nancy, Gerry, and JoAnn for helping with all of our orders, and Greg and Jason for printing posters and maintaining our computers.

This dissertation could not have been done without the countless help of others. Though I could not name all of them here, I am deeply grateful. It is really by working together that we enlarge the boundaries of the sciences and benefit human beings. My Ph.D. training in Schaefer Lab is

not an end, but a beginning to my research career. Thanks to all of you for making it a wonderful start.

Hao Yang

*Washington University in St. Louis*

*December 2015*

Dedicated to my family and friends.

## ABSTRACT OF THE DISSERTATION

Solid-State NMR Study of the Tertiary Structure of the Peptidoglycan of *Enterococcus faecalis* and the Structures of Phorbol Diacetate and Bryostatin Bound to Protein Kinase C $\delta$  C1b Domain

by

Hao Yang

Doctor of Philosophy in Chemistry

Washington University in St. Louis, 2015

Professor Jacob Schaefer, Chair

Solid-state NMR was used to study the structures of phorbol diacetate and bryostatin bound to protein kinase C $\delta$  C1b domain in lipid bilayers. The interaction of protein kinase C (PKC) with native physiological ligands drives fundamental cellular signal transductions, and aberrant PKC signaling is associated with cancer, cardiovascular disease, neurological disorders, stroke, pain, *etc.* Bryostatin modulates PKC and exhibits remarkable potential in treating cancer, Alzheimer's disease, and HIV/AIDS. However, the structural information and dynamics of this modulation, which are crucial for better understanding of PKC-ligand interactions in the membrane microenvironment to drive the development of new drugs, remain elusive. REDOR NMR was used to measure the distances between spin pairs in [ $^{13}\text{C}$ ,  $^2\text{H}_3$ ]phorbol diacetate and [ $^{19}\text{F}$ ,  $^{13}\text{C}$ ,  $^2\text{H}_3$ ]bryostatin bound to PKC $\delta$  C1b domain in lipid bilayers to report on the bio-active bound conformation of the ligands. A single distance was obtained between the  $^{13}\text{C}$  and  $\text{CD}_3$  group in phorbol diacetate, indicating a single conformation, whereas Gaussian distributions of distances were obtained for the three spin pairs in bryostatin, indicating a distribution of conformations. The REDOR results suggest that the binding site of the PKC C1b domain complexed with

bryostatin but not with phorbol diacetate is probably dynamic in solution, and the lyophilized sample therefore contains a distribution of trapped conformations and a distribution of distances. Solid-state NMR experiments also revealed ~60% of phorbol diacetate is peptide bound, and the rest ~40% is lipid associated, whereas almost all bryostatin is peptide bound. This observation is consistent with the fact that bryostatin has a much higher binding affinity to PKC than phorbol diacetate.

Solid-state NMR was also used to study the tertiary structure of the peptidoglycan of *Enterococcus faecalis*. Enterococci have emerged as leading hospital-acquired pathogens in recent years. They are intrinsically resistant to several commonly used antibiotics, and are able to acquire resistance to almost all currently available antibiotics, including the drug of last resort, vancomycin. The *E. faecalis* bacterial cell wall is crucial to maintaining the integrity of the cell structure, and is an important target of antibiotics. Solid-state NMR study revealed ~ 50% cross-linking of *E. faecalis* peptidoglycan and the presence of an active carboxypeptidase that modifies uncross-linked stems. NMR results support the conclusion that the peptidoglycan of *E. faecalis* has the same short-bridge architecture as that of the FemA mutant of *S. aureus*.

Solid-state NMR was used to study the reversible CO<sub>2</sub> capture mechanism of a humidity-swing polymeric sorbent. The CO<sub>2</sub> concentration in the atmosphere has increased from ~280 ppm before the industrial revolution to over 400 ppm in 2015, and is projected to increase to 550 ppm to 900 ppm by the end of this century. This rapid atmospheric CO<sub>2</sub> concentration increase causes global warming and climate change. Together, they pose unprecedented challenges to humans and our environment, calling for our immediate actions to capture and sequester CO<sub>2</sub>

from the atmosphere. The sorbent, containing quaternary ammonium cations, has been shown to absorb CO<sub>2</sub> selectively from dry air and release CO<sub>2</sub> when exposed to humidified air. This could be an inexpensive and recyclable means to capture atmospheric CO<sub>2</sub>. The solid-state NMR investigation here unambiguously reveals the humidity-driven CO<sub>2</sub> absorption and release processes, and suggests that CO<sub>3</sub><sup>2-</sup> is formed upon CO<sub>2</sub> absorption and replaced by OH<sup>-</sup> upon CO<sub>2</sub> release when exposed to humidified air. Based on the NMR evidence, a capture mechanism is proposed which involves electrostatic interactions between the quaternary ammonium cations and CO<sub>3</sub><sup>2-</sup>. This mechanism relies on chemical equilibria to explain why humidity is the driving force for CO<sub>2</sub> absorption and release.

# Chapter 1

## Basic Concepts

### 1.1 Cross Polarization

In solid state NMR, cross polarization (CP) is often used to transfer polarization from high- $\gamma$  and abundant spins (*e.g.*  $^1\text{H}$ ) to low- $\gamma$  and dilute spins (*e.g.*  $^{13}\text{C}$ ), thus enhancing the sensitivity when observing the dilute spins [1, 2]. Figure 1.1 illustrates a pulse sequence involving the polarization transfer from  $^1\text{H}$  to  $^{13}\text{C}$  by CP, followed by detection on the carbon channel.

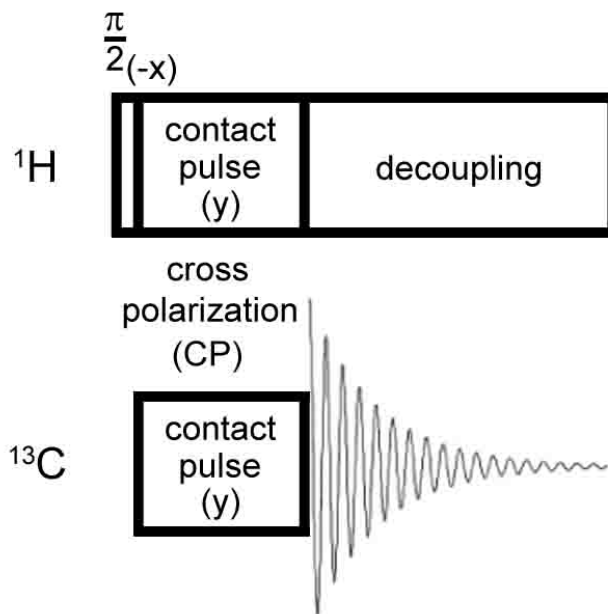


Figure 1.1 Pulse sequence for  $^1\text{H}$  to  $^{13}\text{C}$  CP and subsequent carbon detection.

To have effective CP between I and S spins, the amplitudes of the two contact pulses ( $B_{1I}$  and  $B_{1S}$ ) must satisfy the Hartmann-Hahn condition (Equation 1.1), where  $\gamma_I$  and  $\gamma_S$  are the gyromagnetic ratios of spin I and S, respectively .

$$\gamma_I B_{1I} = \gamma_S B_{1S} \quad (1.1)$$

To illustrate the polarization transfer mechanism in a qualitatively way, consider CP between I and S spins in a double rotating frame during the contact pulse: The magnetization  $M_I$  of spin I and S spins in a double rotating frame during the contact pulse: The magnetization  $M_I$  of spin I precesses about the radio frequency (RF) field  $B_{1I}$  at a frequency  $\Omega_I$  where  $\Omega_I = \gamma_I B_{1I}$  , and  $M_S$  precesses about  $B_{1S}$  at a frequency  $\Omega_S$  where  $\Omega_S = \gamma_S B_{1S}$  (Figure 1.2).

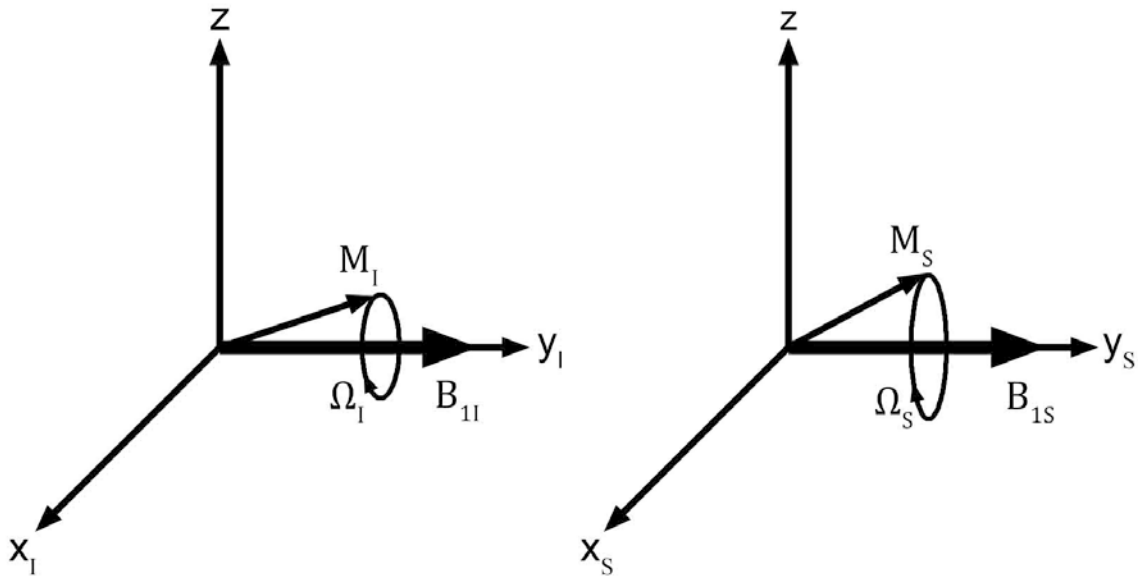


Figure 1.2 I and S spins are spin-locked by  $B_{1I}$  and  $B_{1S}$  RF pulses on the  $xy$ -plane in the double rotating frame.

I and S spins are coupled according to the heteronuclear dipolar coupling Hamiltonian (Equation 1.2), where  $\mu_0$  is the magnetic constant,  $r_{IS}$  is the distance between the coupled I and S spins,  $\theta$  is the angle between the IS internuclear vector and the external magnetic field  $B_0$ .

$$H_{IS} = \frac{\mu_0 \gamma_I \gamma_S \hbar}{4\pi r_{IS}^3} (1 - 3\cos^2\theta) I_Z S_Z \quad (1.2)$$

In a static sample, both  $r_{IS}$  and  $\theta$  are fixed. Thus the heteronuclear dipolar coupling Hamiltonian can be rewritten as  $H_{IS} = C I_Z S_Z$ , where C is a constant. Since the z component of  $M_I$  is oscillating at a frequency of  $\Omega_I$ , the dipolar coupling Hamiltonian is acting like a linearly-oscillating magnetic field along the z direction for spin S. The fact that  $\Omega_I$  matches the S spin precession frequency  $\Omega_S$ , results in a resonance condition and causes the S spin to flip. By the same principle, the I spin is readily flipped too.

In a spin ensemble with many I and S spins, the resonance-induced spin flips will eventually cause the I and S spins to have the same spin temperature. If the I spins are abundant and S spins are dilute, the change of the I spin temperature is negligible. In this case, the S spin polarization enhancement by CP is  $\gamma_I/\gamma_S$ . For  $^1\text{H}$  and  $^{13}\text{C}$  CP, the  $^{13}\text{C}$  polarization enhancement is about 4. The experimental sensitivity gain is even better than 4 because the  $T_1$  of  $^1\text{H}$  is usually shorter than that of  $^{13}\text{C}$ , thus a smaller recycle delay can be used which increases the number of scans in a unit time.

## 1.2 Magic Angle Spinning

Magic Angle Spinning (MAS) is commonly used in solid state NMR to average many anisotropic interactions to their isotropic values. This includes dipolar couplings, first order quadrupolar couplings, and chemical shift anisotropy (CSA), thus improving the spectral resolution [3, 4]. When MAS is performed, the rotor rotates about its cylindrical axis, which is aligned at an angle  $\theta_m$  ( $\approx 54.7^\circ$ ) to  $B_0$  (Figure 1.3).  $\theta_m$  is known as magic angle and satisfies Equation 1.3.

$$1 - 3\cos^2\theta_m = 0 \quad (1.3)$$

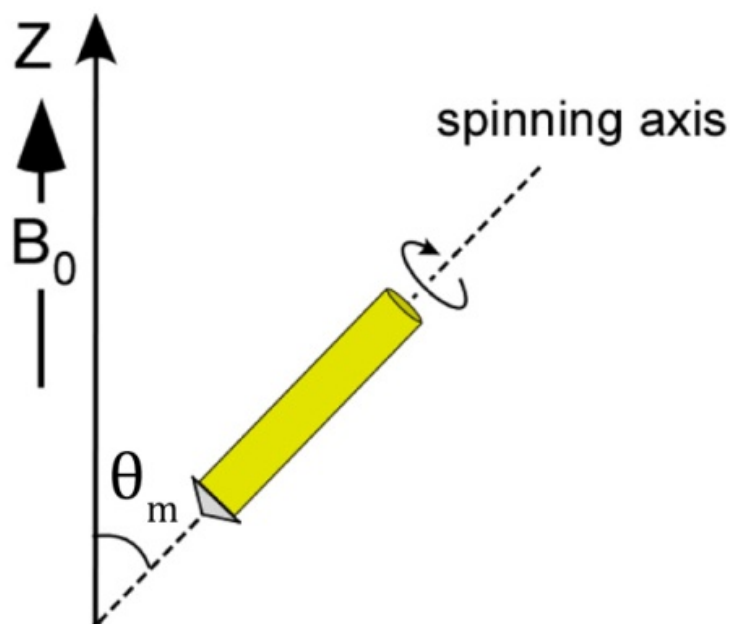


Figure 1.3 A rotor spinning at the magic angle ( $\theta_m$ ).

### 1.2.1 MAS Averages Dipolar Couplings To Zero

MAS removes dipolar couplings by averaging the  $(1 - 3\cos^2\theta)$  term to 0 over one complete rotor cycle in both the heteronuclear (Equation 1.2) and homonuclear (Equation 1.4) dipolar coupling Hamiltonians.  $\theta$  is the angle between the internuclear vector and the external magnetic field  $B_0$ .

$$H_{jk} = \frac{\mu_0 \gamma_j \gamma_k \hbar}{4\pi r_{jk}^3} \frac{1}{2} (1 - 3\cos^2\theta) (3I_{jz}I_{kz} - \mathbf{I}_j \cdot \mathbf{I}_k) \quad (1.4)$$

To theoretically demonstrate the removal of dipolar couplings by MAS, the relative positions of the rotor spinning axis, the internuclear vector, and the external magnetic field  $B_0$  in the laboratory frame are depicted in Figure 1.4 where  $\omega_r$  is the rotor's spinning angular frequency.

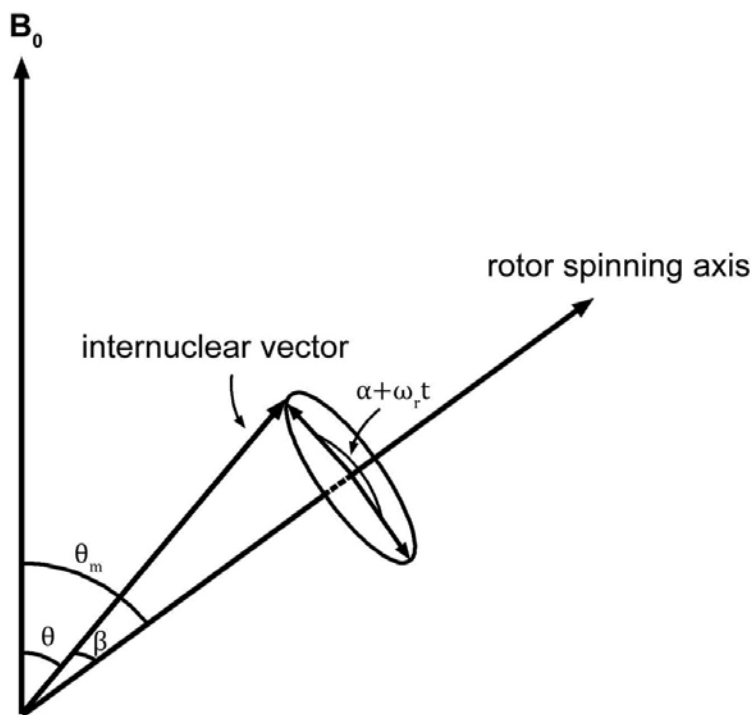


Figure 1.4 Relative positions of the rotor spinning axis, the internuclear vector, and the external magnetic field  $B_0$  in the laboratory frame.

To facilitate the theoretical analysis, the laboratory frame is tilted as shown in Figure 1.5 where  $\mathbf{i}$ ,  $\mathbf{j}$ ,  $\mathbf{k}$ ,  $\mathbf{h}$ ,  $\mathbf{r}_1$ ,  $\mathbf{r}_2$  are unit vectors along each of their defined directions.

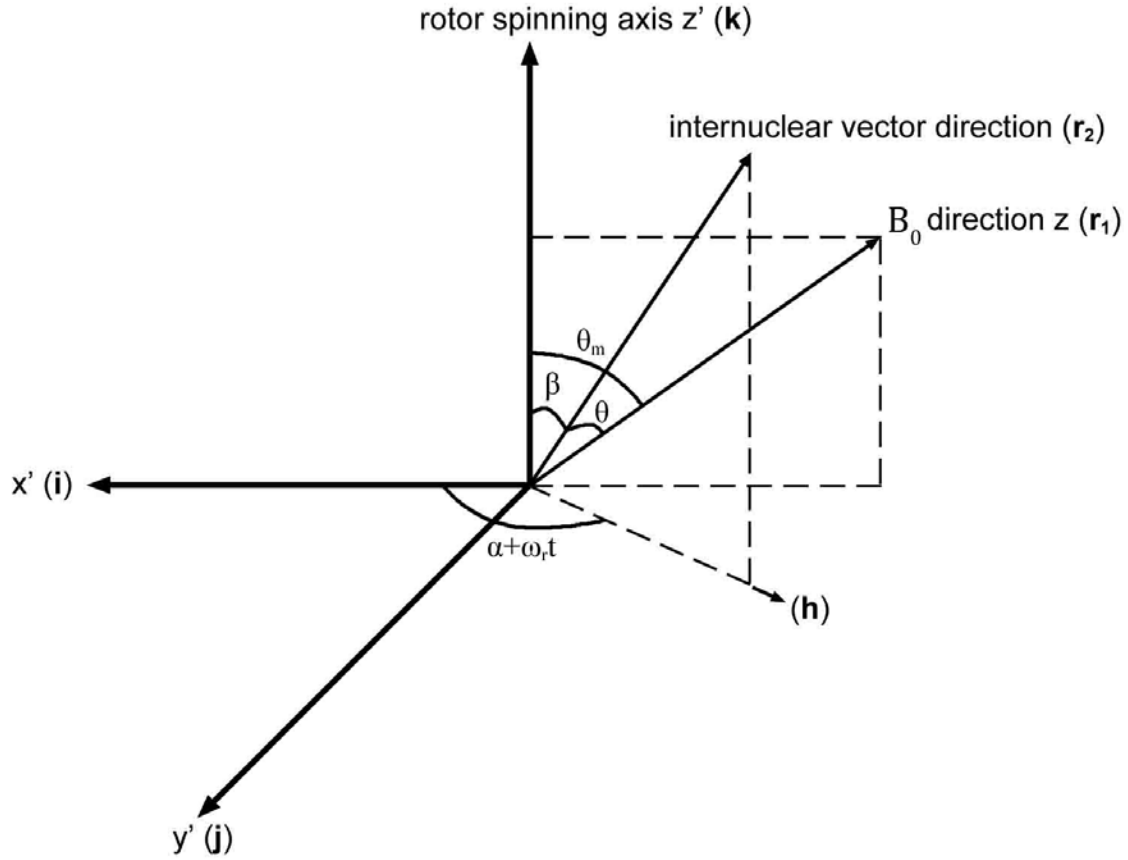


Figure 1.5 The relative positions of the rotor spinning axis, the internuclear vector, and the external magnetic field  $B_0$  in the tilted laboratory frame.

Equation 1.5 through 1.10 below detail the derivation of the value of  $\overline{1 - 3\cos^2\theta}$  over one complete rotor cycle.

$$\mathbf{h} = \mathbf{i}\cos(\alpha + \omega_r t) + \mathbf{j}\sin(\alpha + \omega_r t) \quad (1.5)$$

$$\mathbf{r}_2 = \mathbf{h}\sin\beta + \mathbf{k}\cos\beta = \mathbf{i}\sin\beta\cos(\alpha + \omega_r t) + \mathbf{j}\sin\beta\sin(\alpha + \omega_r t) + \mathbf{k}\cos\beta \quad (1.6)$$

$$\mathbf{r}_1 = -\mathbf{i}\sin\theta_m + \mathbf{k}\cos\theta_m = -\sqrt{\frac{2}{3}}\mathbf{i} + \sqrt{\frac{1}{3}}\mathbf{k} \quad (1.7)$$

$$\cos\theta = \mathbf{r}_1 \cdot \mathbf{r}_2 = -\sqrt{\frac{2}{3}}\sin\beta\cos(\alpha + \omega_r t) + \sqrt{\frac{1}{3}}\cos\beta \quad (1.8)$$

$$1 - 3\cos^2\theta = -[\sin^2\beta\cos 2(\alpha + \omega_r t) - \sqrt{2}\sin 2\beta\cos(\alpha + \omega_r t)] \quad (1.9)$$

$$\begin{aligned} \overline{1 - 3\cos^2\theta} &= -\frac{1}{T_r} \int_0^{T_r} [\sin^2\beta\cos 2(\alpha + \omega_r t) - \sqrt{2}\sin 2\beta\cos(\alpha + \omega_r t)] dt \\ &= -\frac{1}{T_r} \left[ \frac{\sin^2\beta\sin 2(\alpha + \omega_r t)}{2\omega_r} - \frac{\sqrt{2}\sin 2\beta\sin(\alpha + \omega_r t)}{\omega_r} \right] \Bigg|_0^{T_r} = 0 \end{aligned} \quad (1.10)$$

Since  $\overline{1 - 3\cos^2\theta} = 0$  over one complete rotor cycle (Equation 1.10), the average heteronuclear (Equation 1.2) and homonuclear (Equation 1.4) dipolar Hamiltonians are also 0 over one complete rotor cycle.

## 1.2.2 MAS Averages First Order Quadrupolar Couplings To Zero

Equation 1.11 and 1.12 show the first order quadrupolar coupling Hamiltonian where  $C_Q$  is the quadrupolar coupling constant, and  $\theta_Q$  is the angle between the principal axis  $Z$  of the electric field gradient tensor and the external magnetic field  $B_0$ . MAS removes the first order quadrupolar couplings by averaging the  $(1 - 3\cos^2\theta_Q)$  term to 0 in one complete rotor. The proof is the same as that for dipolar coupling (Section 1.2.1) except the internuclear vector is replaced by the principal axis  $Z$  of the electric field gradient tensor.

$$H_Q = \frac{\omega_Q}{6} [3I_z^2 - I(I + 1)\mathbf{1}] \quad (1.11)$$

$$\omega_Q = \frac{3\pi C_Q}{2I(2I-1)} (3\cos^2\theta_Q - 1) \quad (1.12)$$

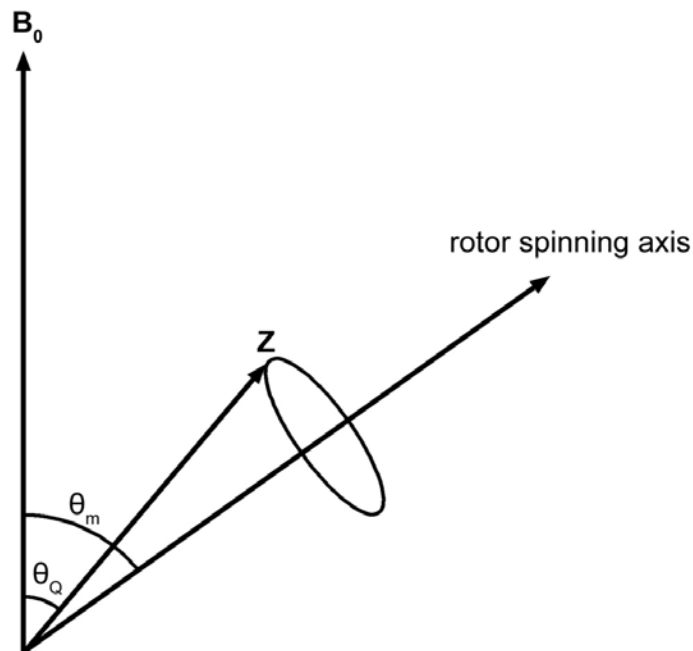


Figure 1.6 The relative positions of the rotor spinning axis, the principal Z axis of the electric field gradient tensor, and the external magnetic field  $B_0$ .

### 1.2.3 MAS Averages CSA To Isotropic Value

In solid state NMR, the chemical shift interaction is anisotropic, and depends on the orientation of the electronic configuration around the nucleus with respect to the direction of  $B_0$ . It is characterized by the chemical shift tensor  $\sigma$  (Equation 1.13 and 1.14).

$$\mathbf{B}_n = \mathbf{B}_0 + \boldsymbol{\sigma}\mathbf{B}_0 \quad (1.13)$$

$$\begin{aligned} \mathbf{B}_n = \begin{pmatrix} B_{nx} \\ B_{ny} \\ B_{nz} \end{pmatrix} &= \begin{pmatrix} 1 & 0 & 0 \\ 0 & 1 & 0 \\ 0 & 0 & 1 \end{pmatrix} \begin{pmatrix} B_{0x} \\ B_{0y} \\ B_{0z} \end{pmatrix} + \begin{pmatrix} \sigma_{xx} & \sigma_{xy} & \sigma_{xz} \\ \sigma_{yx} & \sigma_{yy} & \sigma_{yz} \\ \sigma_{zx} & \sigma_{zy} & \sigma_{zz} \end{pmatrix} \begin{pmatrix} B_{0x} \\ B_{0y} \\ B_{0z} \end{pmatrix} \\ &= \begin{pmatrix} 1 + \sigma_{xx} & \sigma_{xy} & \sigma_{xz} \\ \sigma_{yx} & 1 + \sigma_{yy} & \sigma_{yz} \\ \sigma_{zx} & \sigma_{zy} & 1 + \sigma_{zz} \end{pmatrix} \begin{pmatrix} B_{0x} \\ B_{0y} \\ B_{0z} \end{pmatrix} \end{aligned} \quad (1.14)$$

In the principal axes frame, the off-diagonal elements vanish in the chemical shift tensor (Equation 1.15). Physically, this means in the principal axes frame, the induced field is only along the X, Y, or Z direction when the external magnetic field is along the X, Y, or Z direction.

$$\begin{pmatrix} B_{nX} \\ B_{nY} \\ B_{nZ} \end{pmatrix} = \begin{pmatrix} 1 + \sigma_{XX} & 0 & 0 \\ 0 & 1 + \sigma_{YY} & 0 \\ 0 & 0 & 1 + \sigma_{ZZ} \end{pmatrix} \begin{pmatrix} B_{0X} \\ B_{0Y} \\ B_{0Z} \end{pmatrix} = \begin{pmatrix} (1 + \sigma_{XX})B_{0X} \\ (1 + \sigma_{YY})B_{0Y} \\ (1 + \sigma_{ZZ})B_{0Z} \end{pmatrix} \quad (1.15)$$

Equation 1.16 through 1.27 detail the derivation of the resonance frequency,  $\omega$ , for a nucleus experiencing the chemical shift interaction (Equation 1.27). Here,  $\theta_X$ ,  $\theta_Y$ , and  $\theta_Z$  refer to the angles between the external magnetic field  $B_0$ , and the principal axes X, Y, and Z, respectively.

$$B_n^2 = \mathbf{B}_n \cdot \mathbf{B}_n = (1 + \sigma_{XX})^2 B_{0X}^2 + (1 + \sigma_{YY})^2 B_{0Y}^2 + (1 + \sigma_{ZZ})^2 B_{0Z}^2 \quad (1.16)$$

$$\omega = \gamma |B_n| \quad (1.17)$$

$$\omega^2 = \gamma^2 B_n^2 \quad (1.18)$$

$$B_{0X} = B_0 \cos \theta_X \quad (1.19)$$

$$B_{0Y} = B_0 \cos \theta_Y \quad (1.20)$$

$$B_{0Z} = B_0 \cos \theta_Z \quad (1.21)$$

$$\omega^2 = \gamma^2 B_n^2 = \gamma^2 [(1 + \sigma_{XX})^2 B_0^2 \cos^2 \theta_X + (1 + \sigma_{YY})^2 B_0^2 \cos^2 \theta_Y + (1 + \sigma_{ZZ})^2 B_0^2 \cos^2 \theta_Z] \quad (1.22)$$

$$(1 + \sigma_{XX})^2 = 1 + 2\sigma_{XX} + \sigma_{XX}^2 \approx 1 + 2\sigma_{XX} \quad (1.23)$$

$$\cos^2 \theta_X + \cos^2 \theta_Y + \cos^2 \theta_Z = 1 \quad (1.24)$$

$$\omega^2 = \gamma^2 B_0^2 [(1 + 2\sigma_{XX} \cos^2 \theta_X + 2\sigma_{YY} \cos^2 \theta_Y + 2\sigma_{ZZ} \cos^2 \theta_Z)] \quad (1.25)$$

$$(1 + x)^{\frac{1}{2}} \approx 1 + \frac{1}{2}x \quad (1.26)$$

$$\omega = \gamma B_0 (1 + \sigma_{XX} \cos^2 \theta_X + \sigma_{YY} \cos^2 \theta_Y + \sigma_{ZZ} \cos^2 \theta_Z) \quad (1.27)$$

When MAS is performed (Figure 1.7), Equation 1.28 holds true for one complete rotor cycle. The proof is the same as that for dipolar coupling (Section 1.2.1) except the internuclear vector is replaced by the principal X, Y and Z axes of the chemical shift tensor.

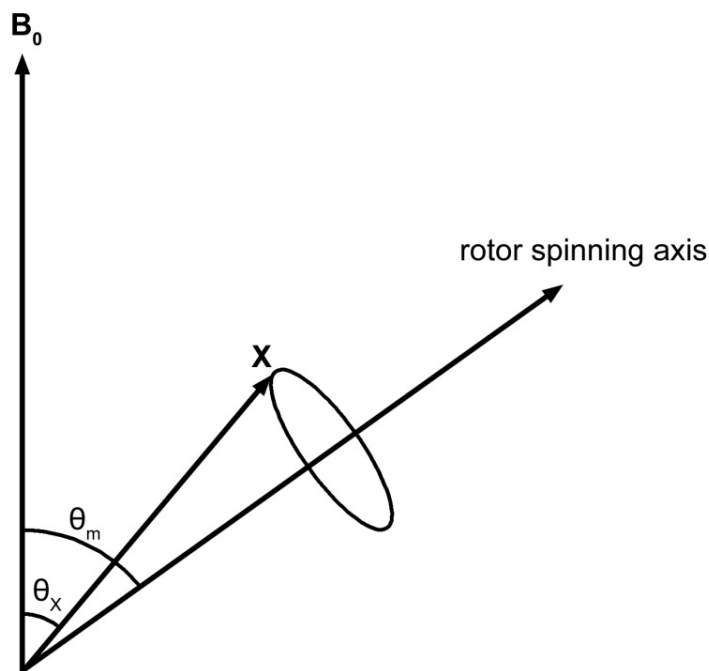


Figure 1.7 The relative positions of the rotor spinning axis, the principal X axis of the chemical shift tensor, and the external magnetic field  $B_0$ .

$$\overline{\cos^2\theta_X} = \overline{\cos^2\theta_Y} = \overline{\cos^2\theta_Z} = \frac{1}{3} \quad (1.28)$$

By substituting Equation 1.28 into Equation 1.27, the resonance frequency under MAS is obtained (Equation 1.29), and found to be the isotropic chemical shift.

$$\bar{\omega} = \gamma B_0 \left( 1 + \frac{\sigma_{XX} + \sigma_{YY} + \sigma_{ZZ}}{3} \right) = \gamma B_0 (1 + \sigma_{iso}) \quad (1.29)$$

In liquid state, where molecules tumble fast isotropically, Equation 1.28 also holds true. Thus Equation 1.29 is valid. This is why only the isotropic chemical shifts are observed in solution-state NMR.

## 1.3 CPMAS

In solid-state NMR, CP enhances sensitivity, and MAS enhances resolution. A combination of CP and MAS to gain high-sensitivity and high-resolution at the same time is desirable. However, CP and MAS seem naturally contradictory to one another because CP relies on dipolar couplings, whereas MAS removes dipolar couplings. Despite the shadow cast by this apparent contradiction, the first attempt of CPMAS proved to be a great success, and CPMAS spectra resembling that of the solution-state were obtained (Figure 1.8) [5].

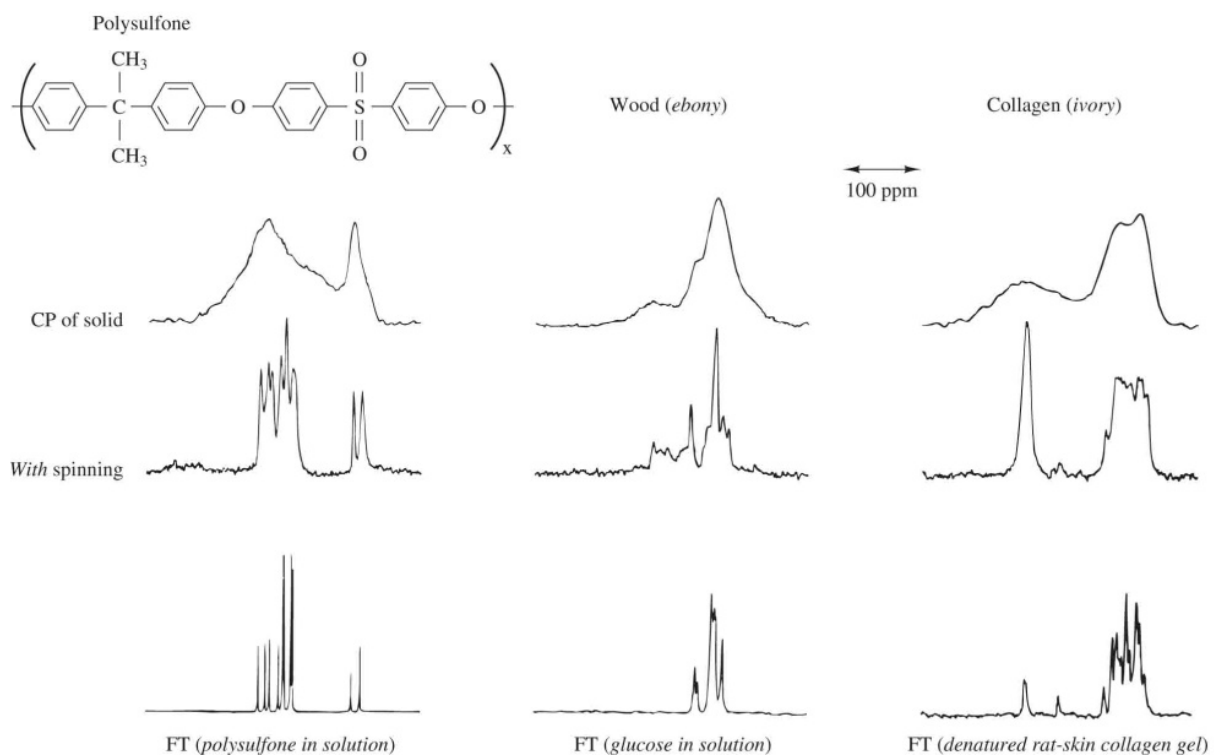


Figure 1.8 The first CPMAS experiment [5]. Top row: CP without MAS. Middle row: CPMAS. Bottom row: solution-state.

Detailed studies later revealed [6] that CP remains effective under MAS as long as the spinning frequency is lower than the dipolar couplings among abundant spins, which are protons for most organic and biological samples. Thus under this regime, CP can be effectively combined with MAS and high-power proton decoupling pulses, where CP transfers polarization from protons to low- $\gamma$  and dilute spins, MAS removes CSA and dipolar couplings between dilute spins, and high-power proton decoupling pulses remove dipolar couplings to protons. This approach has gained great popularity and become one of the fundamental methods in the field of solid-state NMR.

## 1.4 Rotational-Echo Double-Resonance (REDOR)

REDOR measures the distance between a pair of dipolar-coupled IS spins [7, 8]. The measurement accuracy can be up to 0.1 Å. A typical REDOR pulse sequence contains two parts:  $S_0$  and S. Dephasing pulses are present in the middle of each rotor cycle in the S sequence, and result in peak intensity reduction due to dipolar coupling evolution (Figure 1.9). Since dipolar coupling strength depends on  $\frac{1}{r_{IS}^3}$  (Equation 1.2), the internuclear distance  $r_{IS}$  can be obtained by fitting the plot of  $\Delta S/S_0$  versus dephasing time (Figure 1.10). Figure 1.11 shows the REDOR detection limits of some commonly-studied nuclei in organic and biological samples.

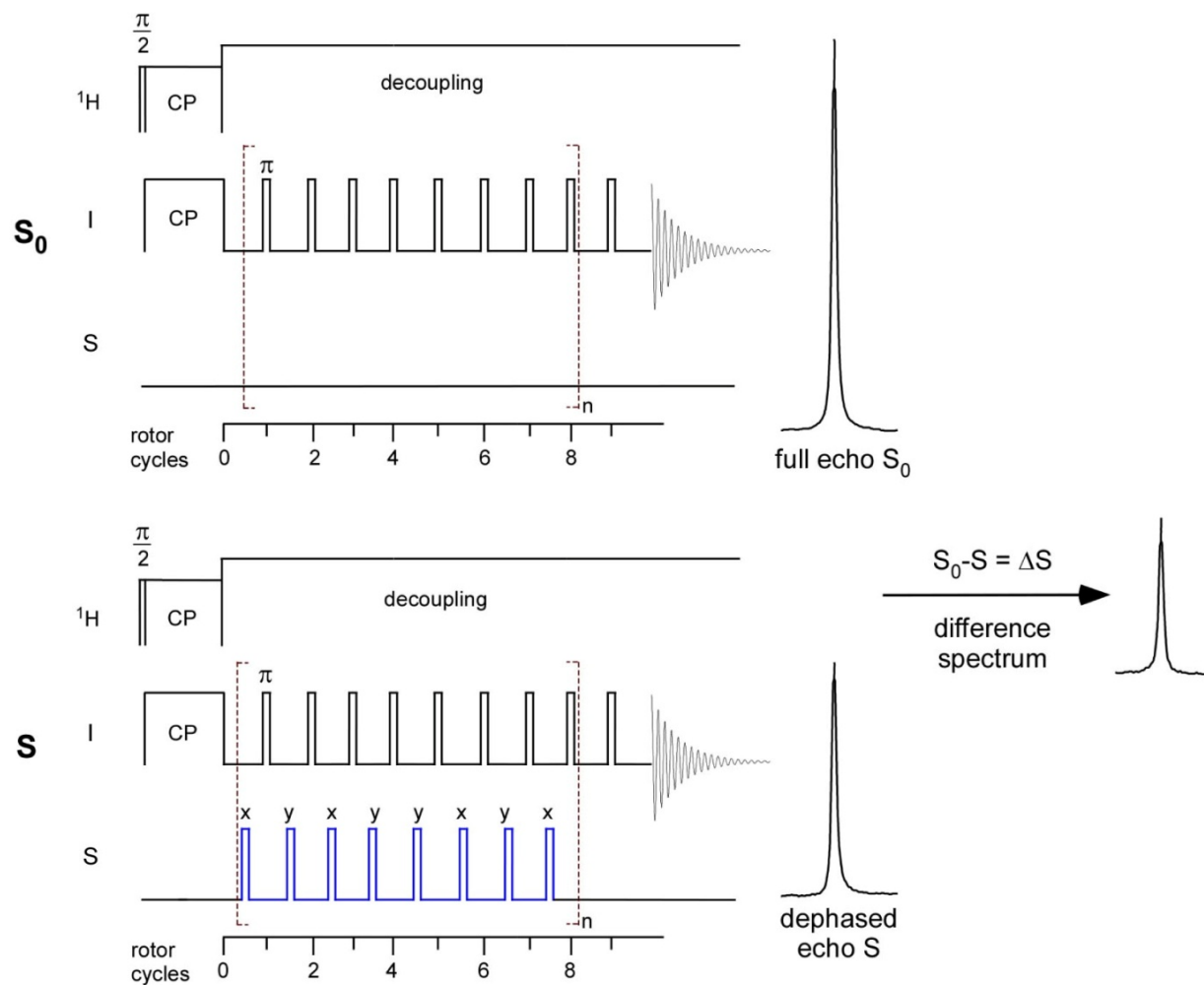


Figure 1.9 A typical REDOR pulse sequence.

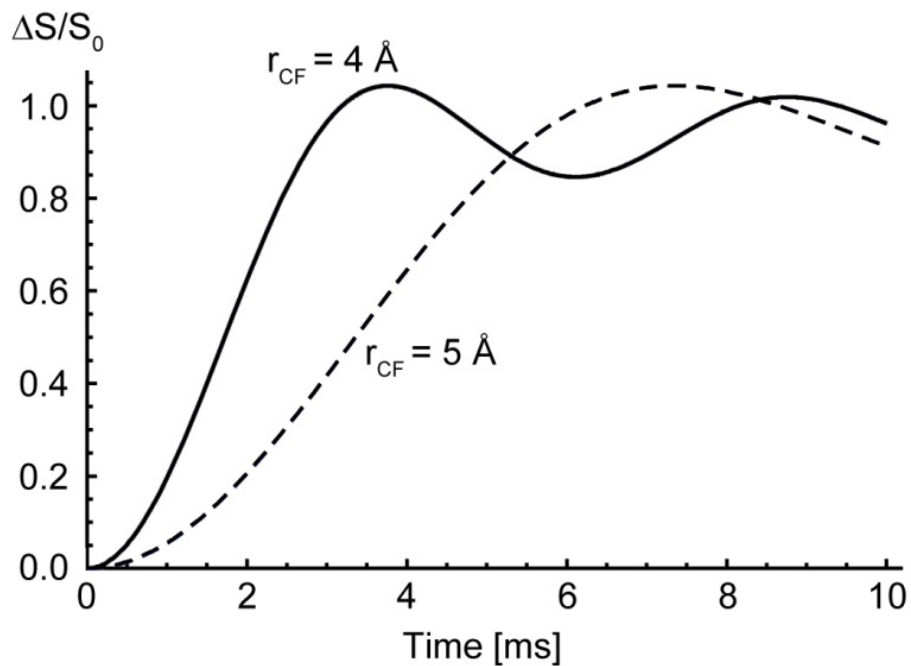


Figure 1.10 REDOR curves for a pair of dipolar-coupled  $^{13}\text{C}$ - $^{19}\text{F}$  nuclei with an internuclear distance of 4 and 5 Å, respectively.

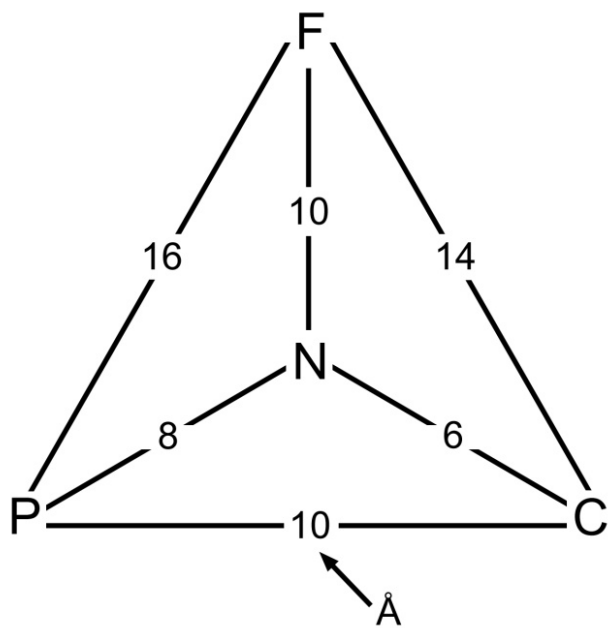


Figure 1.11 REDOR detection limits.

To understand how REDOR works, a theoretical demonstration is provided below. First the heteronuclear dipolar Hamiltonian is given in detail (Equation 1.30 to 1.32), then  $\omega_D$  (Equation 1.33) is rewritten by substituting Equation 1.9 into Equation 1.31.

$$H_{IS} = 2\omega_D I_z S_z = D(1 - 3\cos^2\theta) I_z S_z \quad (1.30)$$

$$\omega_D = \frac{1}{2}D(1 - 3\cos^2\theta) \quad (1.31)$$

$$D = \frac{\mu_0}{4\pi} \cdot \frac{\gamma_I \gamma_S \hbar}{(r_{IS})^3} \text{rad} \cdot \text{s}^{-1} = \frac{\mu_0}{4\pi} \cdot \frac{\gamma_I \gamma_S \hbar}{2\pi(r_{IS})^3} \text{Hz} \quad (1.32)$$

$$\omega_D = \frac{1}{2}D(1 - 3\cos^2\theta) = -\frac{1}{2}D[\sin^2\beta\cos 2(\alpha + \omega_r t) - \sqrt{2}\sin 2\beta\cos(\alpha + \omega_r t)] \quad (1.33)$$

The general equation to calculate the spin density matrix after time evolution under a Hamiltonian (Equation 1.34) is modified specifically to calculate the density matrix stroboscopically in REDOR (Equation 1.35 and 1.36). The key is to calculate the average Hamiltonian in one of the repeating rotor cycles (Equation 1.37). The average Hamiltonian in one complete rotor cycle is 0 if there is no dephasing pulse (Equation 1.38) implying there is no dipolar evolution.

$$\rho(t) = e^{-i \int_0^t H(t) dt} \rho(0) e^{i \int_0^t H(t) dt} \quad (1.34)$$

$$\rho(T_r) = e^{-i \bar{H} T_r} \rho(0) e^{i \bar{H} T_r} \quad (1.35)$$

$$\rho(N T_r) = e^{-i \bar{H} N T_r} \rho(0) e^{i \bar{H} N T_r} \quad (1.36)$$

$$\bar{H} = \frac{1}{T_r} \int_0^{T_r} H_{IS}(t) dt = \frac{2}{T_r} I_z S_z \int_0^{T_r} \omega_D(t) dt = 2\bar{\omega}_D I_z S_z \quad (1.37)$$

$$\begin{aligned} \bar{\omega}_D &= \frac{1}{T_r} \int_0^{T_r} \omega_D(t) dt = -\frac{D}{2T_r} \int_0^{T_r} [\sin^2\beta\cos 2(\alpha + \omega_r t) - \sqrt{2}\sin 2\beta\cos(\alpha + \omega_r t)] dt \\ &= -\frac{D}{2T_r} \left[ \frac{\sin^2\beta\cos 2(\alpha + \omega_r t)}{2\omega_r} - \frac{\sqrt{2}\sin 2\beta\cos(\alpha + \omega_r t)}{\omega_r} \right] \Bigg|_0^{T_r} = 0 \end{aligned} \quad (1.38)$$

When a dephasing pulse is placed in a rotor cycle (Figure 1.12), the average Hamiltonian is non-zero (Equation 1.39), and dipolar evolution occurs leading to dephasing (Equation 1.40 to 1.43). For most organic and biological samples, which are not single crystals, the powder average is needed (Equation 1.44).

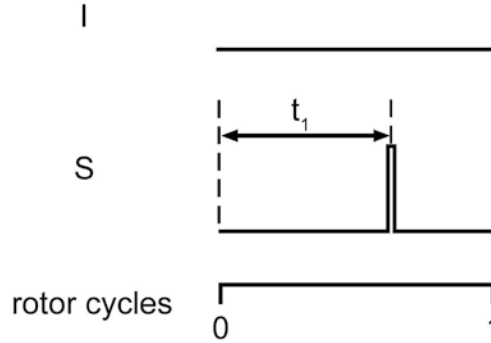


Figure 1.12 A single rotor cycle containing one dephasing pulse.

$$\begin{aligned}
 \bar{\omega}_D &= \frac{1}{T_r} \left[ \int_0^{t_1} \omega_D(t) dt - \int_{t_1}^{T_r} \omega_D(t) dt \right] \\
 &= -\frac{D}{4\omega_r T_r} \left\{ [\sin^2 \beta \sin 2(\alpha + \omega_r t) - 2\sqrt{2} \sin 2\beta \sin(\alpha + \omega_r t)] \Big|_0^{t_1} \right. \\
 &\quad \left. - [\sin^2 \beta \sin 2(\alpha + \omega_r t) - 2\sqrt{2} \sin 2\beta \sin(\alpha + \omega_r t)] \Big|_{t_1}^{T_r} \right\} \\
 &= -\frac{D}{4\pi} \{ \sin^2 \beta [\sin 2(\alpha + \omega_r t_1) - \sin 2\alpha] - 2\sqrt{2} \sin 2\beta [\sin(\alpha + \omega_r t_1) - \sin \alpha] \} \quad (1.39)
 \end{aligned}$$

$$e^{-i\bar{H}NT_r} = e^{-i2NT_r \bar{\omega}_D I_z S_z} = e^{-i2\Delta\Phi I_z S_z} \quad (1.40)$$

$$\Delta\Phi = NT_r \bar{\omega}_D \quad (1.41)$$

$$S_x \xrightarrow{2\Delta\Phi I_z S_z} \cos\Delta\Phi \cdot S_x + \sin\Delta\Phi \cdot 2I_z S_z \quad (1.42)$$

$$\frac{S}{S_0} = \cos\Delta\Phi \quad (1.43)$$

$$\frac{S}{S_0} = \frac{1}{4\pi} \int_0^{2\pi} \left( \int_0^\pi \cos\Delta\Phi \sin\beta d\beta \right) d\alpha \quad (1.44)$$

Dephasing increases with a bigger dipolar coupling constant and more rotor cycles (Figure 1.13).

The position of the dephasing pulse is also important. The simulation below indicates that the largest dephasing is obtained when the dephasing pulse is placed in the center of the rotor cycle

( $\frac{t_1}{T_r} = \frac{1}{2}$ ) (Figure 1.13).

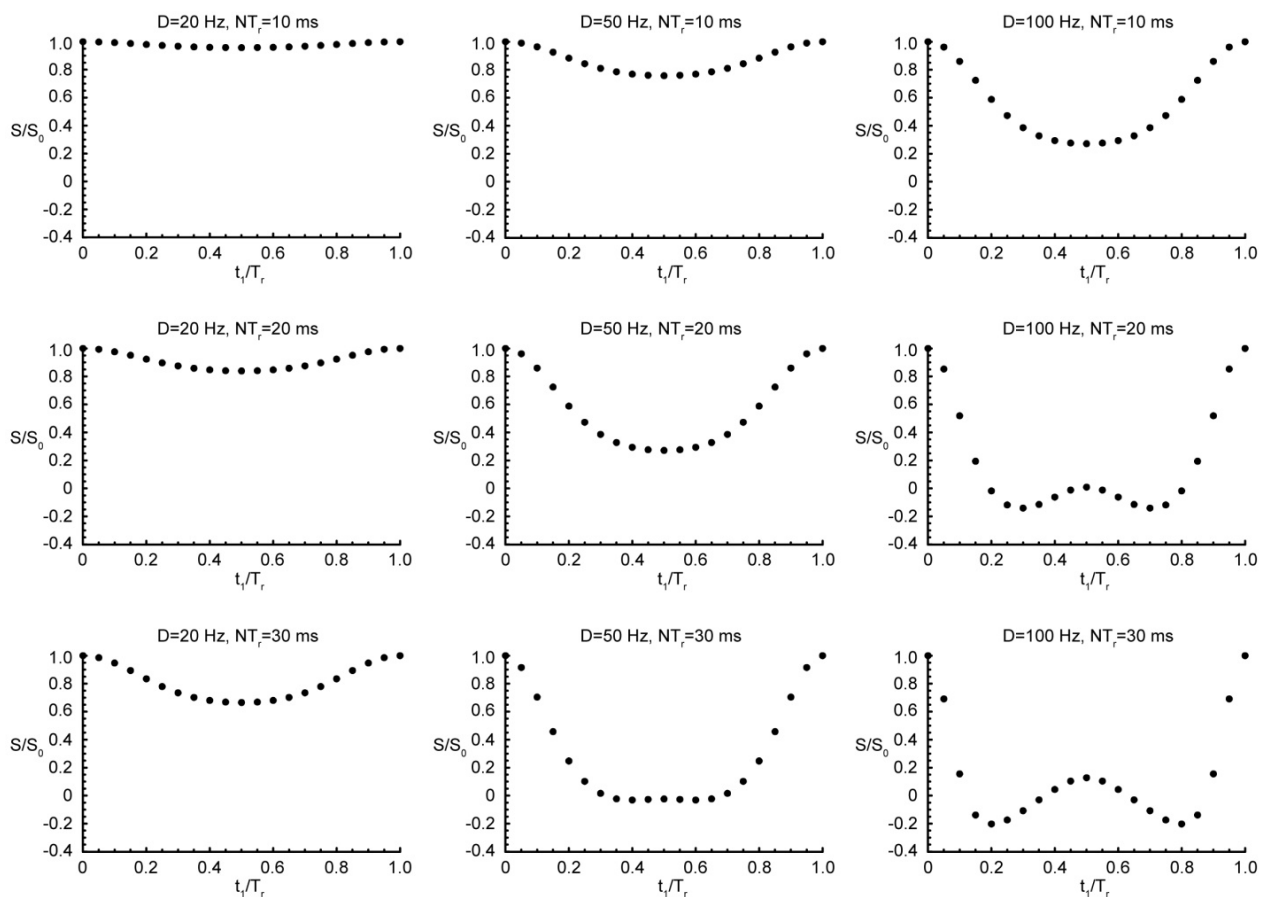


Figure 1.13 A simulation of REDOR dephasing as a function of  $t_1$ , dipolar coupling constant ( $D$ ), and dephasing time.

When  $\frac{t_1}{T_r} = \frac{1}{2}$ , a simplified expression for  $\bar{\omega}_D$  is obtained (Equation 1.45), and an analytical expression of  $\Delta S/S_0$  for the powder average is derived (Equation 1.46) [9], where J is the Bessel function of the first kind, and D is in unit of Hertz.

$$\bar{\omega}_D = -\frac{\sqrt{2}D}{\pi} \sin 2\beta \sin \alpha \quad (1.45)$$

$$\frac{S}{S_0} = \frac{1}{4\pi} \int_0^{2\pi} \left( \int_0^\pi \cos \Delta\Phi \sin \beta \, d\beta \right) d\alpha = \frac{\sqrt{2}\pi}{4} J_{1/4}(\sqrt{2}NT_r D) J_{-1/4}(\sqrt{2}NT_r D) \quad (1.46)$$

## 1.5 References

1. Hartmann, S.R. and Hahn, E.L., *Nuclear Double Resonance in Rotating Frame*. Physical Review, 1962. **128**(5): 2042-2053.
2. Pines, A., Gibby, M.G., and Waugh, J.S., *Proton-Enhanced NMR of Dilute Spins in Solids*. Journal of Chemical Physics, 1973. **59**(2): 569-590.
3. Andrew, E.R., Bradbury, A., and Eades, R.G., *Removal of Dipolar Broadening of Nuclear Magnetic Resonance Spectra of Solids by Specimen Rotation*. Nature, 1959. **183**(4678): 1802-1803.
4. Lowe, I.J., *Free Induction Decays of Rotating Solids*. Physical Review Letters, 1959. **2**(7): 285-287.
5. Schaefer, J. and Stejskal, E.O., *<sup>13</sup>C Nuclear Magnetic-Resonance of Polymers Spinning at Magic Angle*. Journal of the American Chemical Society, 1976. **98**(4): 1031-1032.
6. Stejskal, E.O., Schaefer, J., and Waugh, J.S., *Magic-Angle Spinning and Polarization Transfer in Proton-Enhanced NMR*. Journal of Magnetic Resonance, 1977. **28**(1): 105-112.
7. Gullion, T. and Schaefer, J., *Rotational-Echo Double-Resonance NMR*. Journal of Magnetic Resonance, 1989. **81**(1): 196-200.
8. Pan, Y., Gullion, T., and Schaefer, J., *Determination of C-N Internuclear Distances by Rotational-Echo Double-Resonance NMR of Solids*. Journal of Magnetic Resonance, 1990. **90**(2): 330-340.

9. Mueller, K.T., Jarvie, T.P., Aurentz, D.J., and Roberts, B.W., *The REDOR Transform - Direct Calculation of Internuclear Couplings from Dipolar-Dephasing NMR Data*. Chemical Physics Letters, 1995. **242**(6): 535-542.

## Chapter 2

# Solid-State NMR Study of the Structures of Phorbol Diacetate and Bryostatin Bound to Protein Kinase C $\delta$ C1b Domain

### 2.1 Introduction

Since their discovery in the 1970s [1, 2], protein kinase C (PKC) isoforms have attracted considerable interest due to their central role in cellular signal transduction [3]. The PKC family consists of ten related enzymes classified into three subfamilies: conventional PKCs (PKC $\alpha$ ,  $\beta$ I,  $\beta$ II, and  $\gamma$ ) (Figure 2.1), novel PKCs (PKC $\delta$ ,  $\epsilon$ ,  $\theta$ , and  $\eta$ ) (Figure 2.1), and atypical PKCs (PKC  $\zeta$  and  $\lambda$ /i) [4]. Each cell has multiple PKC isoforms [4]. Conventional PKCs require both a diacylglycerol (DAG) cofactor (Figure 2.2) and calcium to associate with the C1 domains (C1a and C1b) to activate the kinase, whereas novel PKCs only require a DAG cofactor [4-8]. Atypical PKCs share less sequence homology with the conventional and novel PKCs [4]. They also do not respond to the same activators as the conventional and novel PKCs [4]. The function of the activator DAG can be mimicked with a variety of small molecules such as phorbol esters, prostratin, bryostatins, daphnane diterpenoid orthoesters, aplysiatoxin, teleocidins, *etc.* (Figure 2.2), many of which are far more potent than the endogenous ligand DAG [9]. Importantly, non-

natural, designed ligands based on these natural products have been shown to retain or even exceed the potency of their parent scaffolds [10, 11]. In some cases, these designed ligands elicit previously unseen selectivities and activities [12]. The native and non-natural ligands serve as widely used research tools and inspire the discovery of new drugs, targeting diseases including cancer, cardiovascular disease, stroke, pain, cognitive dysfunction and HIV/AIDS eradication, among others, by modulating protein kinase C [4].

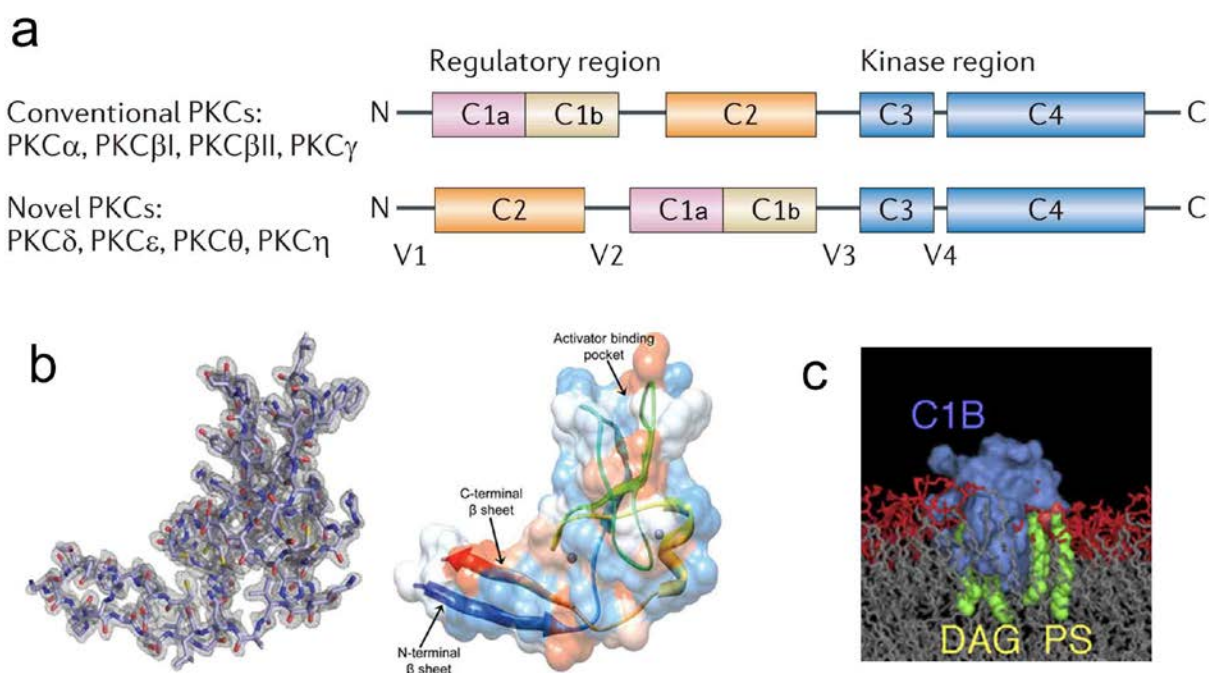


Figure 2.1 (a) The domain composition of PKC isoforms [4]. (b) The crystal structure of PKC $\theta$  C1b domain [13]. The electron density map is on the left, and the ribbon structure superimposed on the contour surface is on the right. (c) The model of PKC $\gamma$  C1b domain interacting with the activator DAG and phosphatidylserine (PS) in lipid bilayers [14]. The phosphatidylserine tightly bound to the C1b domain is depicted in CPK format, and the surrounding phosphatidylserine bilayers are in stick format.

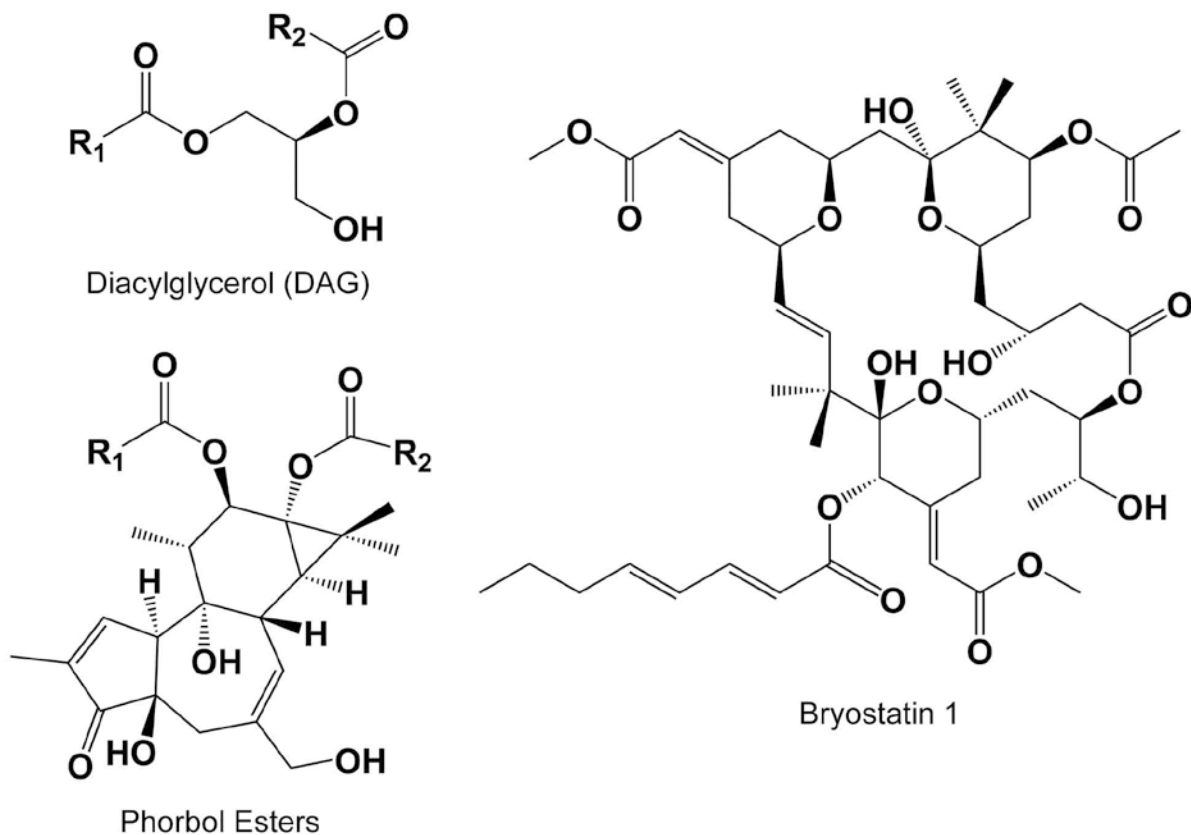


Figure 2.2 The structure of some PKC activators.

Unfortunately, structural detail regarding the binding interaction between PKC and phorbol esters, bryostatin, and other ligands is limited. Experimental approaches, including solution NMR and X-ray crystallography, have provided structures of PKC C1 domains in the presence and absence of certain ligands [13, 15-19] and a full-length crystal structure of PKC $\beta$ II was recently reported [20]. However, no structural detail has been elucidated for PKC in a biorelevant membrane microenvironment with an appropriate membrane surrogate. The membrane microenvironment could contribute significantly to: (i) the development of proper secondary and tertiary structure and (ii) potentially crucial structural dynamics that relate to function. Indeed, early studies aimed at determining the solution NMR structure of a PKC $\gamma$

fragment bound to phorbol 12,13-dibutyrate (PDBu) indicates that PKC does not fold properly in an aqueous environment but only when associated with phospholipid vesicles, and the vesicles must contain at least 15% phosphatidylserine for proper folding and binding [21, 22].

Differences have also been noted among X-ray, solution NMR, and solid-state NMR determined structures of *E. coli* diacylglycerol kinase (a transmembrane enzyme) when it was studied in different microenvironments (micelles for solution NMR, lipidic cubic phases for crystallography, and lipid bilayers/vesicles for solid-state NMR) [23]. Ideally, membrane-associated proteins should be studied in membrane microenvironments that maintain protein function.

Solid-state NMR spectroscopy is uniquely suited to examine and access site-specific atomic-level information in noncrystalline and heterogeneous molecular systems such as membrane-associated protein complexes. Rotational-Echo Double-Resonance (REDOR) NMR enables the determination of short and long-range heteronuclear dipolar couplings and hence distances, typically between isolated spin pairs [24, 25]. Since its introduction in 1989, REDOR has found wide applicability in diverse macromolecular and whole-cell systems including enzyme-cofactor-inhibitor ternary complexes, protein-protein complexes, lipid-embedded membrane proteins, bacteria-antibiotic complexes, and intact leaves [26-28]. REDOR approaches require the design and generation of strategically labeled samples to enable key distance determinations and require the optimization of pulse-sequence parameters. The gyromagnetic ratios of the nuclei being observed put constraints on the distance that can be measured, but distances as long as 16 Å have been successfully determined on a  $^{31}\text{P}\{^{19}\text{F}\}$  system [29, 30].

A systematic approach has been designed to examine PKC $\delta$  C1b domain peptide complexes with potent ligands including bryostatin by measuring intra-ligand, ligand-protein, intra-protein, ligand-membrane, and protein-membrane distances between selectively incorporated  $^{13}\text{C}$ ,  $^{15}\text{N}$ ,  $^{19}\text{F}$ ,  $^{31}\text{P}$ , and  $^2\text{H}$  (D) labels to provide atomic-level structural constraints required to establish the structural basis of ligand binding and to map the protein-ligand-membrane topology in biorelevant complexes. Such detail is critically needed for the design of new PKC isoform selective ligands and hence therapeutic leads, and more generally for understanding the functional role of PKC in a membrane microenvironment.

The efforts reported below are first-in-class with respect to this challenge, interrogating a three-component system comprised of a  $^{13}\text{C}/\text{CD}_3$ -labeled phorbol diacetate ( $[^{13}\text{C}, ^2\text{H}_3]\text{PDAc}$ ) (Figure 2.3) as a model ligand, phosphatidylserine (PS) multilamellar vesicles as the membrane surrogate, and the 51-residue mouse PKC $\delta$  C1b domain representing the membrane-associated protein of interest. While REDOR studies have been reported for several membrane-associated proteins of human and bacterial origin, few included a bound ligand [31-35], fewer were aimed at measuring long-range intra-ligand distances [36-38], and none involved protein kinase C. Here, solid-state NMR experiments were designed and implemented to determine a precise intra-ligand distance in phorbol diacetate at a site known to be highly tunable for PKC affinity. In addition, the experiments revealed the presence of mobile phorbol diacetate in lipid bilayers, a phenomenon that has not been previously observed for PKC-associated ligands.

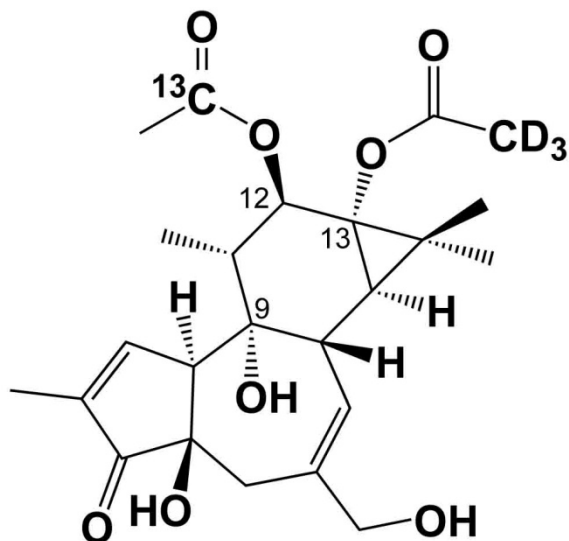


Figure 2.3 [ $^{13}\text{C}, ^2\text{H}_3$ ]PDAc structure.

## 2.2 Materials and Methods

### 2.2.1 NMR Sample Preparation

Solid-state NMR samples were prepared with the goal of obtaining 220 mg of final lyophilized sample to be loaded into a 5-mm thin-wall rotor. Components included in this sample were phosphatidylserine (PS, Avanti Polar Lipids), ligand ([ $^{13}\text{C}, ^2\text{H}_3$ ]PDAc or [ $^{19}\text{F}, ^{13}\text{C}, ^2\text{H}_3$ ]bryostatin), peptide (Anaspec, PKC $\delta$  C1b domain), and trehalose (vesicle cryoprotectant). The sample was prepared using a molar ratio of 1:1:50:50 for ligand:peptide:phosphatidylserine:trehalose.

### 2.2.2 Solid-State NMR Experiments

The NMR spectrometer has an 89-mm bore, 12-T static field ( $^1\text{H}$  at 500 MHz, Magnex, Agilent, Santa Clara, CA), a Tecmag (Houston, TX) Apollo console, and a homebuilt four-channel ( $^1\text{H}$ ,  $^{19}\text{F}$ ,  $^{13}\text{C}$ ,  $^2\text{H}$ ) transmission-line probe equipped with a 5 mm Chemagnetics/Varian stator and zirconium rotors. Radio frequency pulses for  $^1\text{H}$  were amplified first by a 50-W American Microwave Technology (AMT, Anaheim, CA) power amplifier and then by a 2-kW Creative Electronics tube amplifier. AMT amplifiers (2 kW) were used for  $^{13}\text{C}$  and  $^2\text{H}$  pulses. In all the NMR experiments, 71-kHz pulses (7  $\mu\text{s}$  for  $\pi$  pulses) were used for  $^1\text{H}$ ,  $^{13}\text{C}$  and  $^2\text{H}$ , and the proton decoupling strength was 80 kHz. Matched cross-polarization transfers were made at 71 kHz in 1.68 ms (12 rotor cycles) in the  $^{13}\text{C}\{^2\text{H}\}$  REDOR and  $^{13}\text{C}$  CPMAS experiments. Adamantane was used as an external  $^{13}\text{C}$  chemical shift reference [39]. Spinning rates were actively controlled to  $7143 \pm 2$  Hz. All RF pulse amplitudes were under active control ( $H_1$  control) to eliminate long-term drifts due to component aging or changes in temperature [40]. Additionally, alternating scans of  $S_0$  and  $S$  were acquired to compensate for short-term drift. XY-8 phase cycling [41] was used for all refocusing ( $^{13}\text{C}$ ) and dephasing ( $^2\text{H}$ ) pulses [42, 43].

### 2.2.3 REDOR Calculations

$^{13}\text{C}\{^2\text{H}\}$ REDOR dephasing for the  $^{13}\text{C}$ - $\text{CD}_3$  system was calculated using modifications (Table 2.1) of the analytical expression of Mueller *et al.* that were developed for spin-1/2 pairs [44].

Table 2.1 REDOR analytical expressions for spin pairs containing spin-1.

Spin Pair	$\frac{\Delta S}{S_0}$ (an isolated spin pair)	$\frac{\Delta S}{S_0}$ (powder average of an ensemble of spin pairs)
spin- $\frac{1}{2}$ and spin- $\frac{1}{2}$ (e.g. $^{13}\text{C}$ - $^{15}\text{N}$ )	$\cos[\bar{\omega}_D n T_r]$	$\frac{\sqrt{2}\pi}{4} J_{1/4}(\sqrt{2}DnT_r) J_{-1/4}(\sqrt{2}DnT_r)$
spin- $\frac{1}{2}$ and spin-1 (e.g. $^{13}\text{C}$ -D)	$\frac{1}{3} [1 + 2\cos(2\bar{\omega}_D n T_r)]$	$\frac{1}{3} \{1 + 2[\frac{\sqrt{2}\pi}{4} J_{1/4}(2\sqrt{2}DnT_r) J_{-1/4}(2\sqrt{2}DnT_r)]\}$
spin- $\frac{1}{2}$ and a super spin made up of three spin-1 (e.g. $^{13}\text{C}$ - $\text{CD}_3$ )	$\frac{1}{27} [7 + 12\cos(2\bar{\omega}_D n T_r)$ $+ 6\cos(4\bar{\omega}_D n T_r)$ $+ 2\cos(6\bar{\omega}_D n T_r)]$	$\frac{1}{27} \{7 + 12[\frac{\sqrt{2}\pi}{4} J_{1/4}(2\sqrt{2}DnT_r) J_{-1/4}(2\sqrt{2}DnT_r)]$ $+ 6[\frac{\sqrt{2}\pi}{4} J_{1/4}(4\sqrt{2}DnT_r) J_{-1/4}(4\sqrt{2}DnT_r)]$ $+ 2[\frac{\sqrt{2}\pi}{4} J_{1/4}(6\sqrt{2}DnT_r) J_{-1/4}(6\sqrt{2}DnT_r)]\}$

$^{13}\text{C}\{^2\text{H}\}$ REDOR of a single  $^{13}\text{C}$ -D pair would exhibit maximum dephasing of 67%, corresponding to two of the three eigen states ( $m = -1, 0, +1$ ) for D that are spin-active ( $m = \pm 1$ ) (Table 2.1). The rapidly rotating  $\text{CD}_3$  dephaser was approximated as a single super spin centered in the triangle defined by the three D nuclei [45, 46]. There are 27 states for a  $D_3$  group, where 7

states are not spin active ( $M = 0$ ) (Table 2.2). Thus the maximum  $^{13}\text{C-D}_3$  dephasing is 74%. The dephaser in the phorbol diacetate is predominantly present as a  $\text{CD}_3$  group, but some was present as  $\text{CD}_2\text{H}$  and  $\text{CDH}_2$ . Mass spectrometry determined the enrichment as 90.1%  $\text{CD}_3$ , 8.5%  $\text{CD}_2\text{H}$ , 0.6%  $\text{CDH}_2$  and 0.8%  $\text{CH}_3$ . These values were included in the calculation. Similarly, the  $\text{CD}_2\text{H}$  was treated as a super spin centered in the  $\text{D}_2\text{H}$  triangle, and the  $\text{CDH}_2$  was treated as a single spin centered in the  $\text{DH}_2$  triangle. For the calculation, a fit of  $\Delta S/S_0$  as a function of dephasing time yielded the dipolar coupling constant and hence the internuclear distance.

Table 2.2  $\text{D}_3$  spin states.

[M]	Degeneracy	M	Spin States ( $m_1, m_2, m_3$ )
0	7	0	(+1,0,-1), (+1,-1,0), (0,+1,-1), (0,0,0), (0,-1,+1), (-1,+1,0), (-1,0,+1)
1	12	+1	(+1,+1,-1), (+1,0,0), (+1,-1,+1), (0,+1,0), (0,0,+1), (-1,+1,+1)
		-1	(+1,-1,-1), (0,0,-1), (0,-1,0), (-1,+1,-1), (-1,0,0), (-1,-1,+1)
2	6	+2	(+1,+1,0), (+1,0,+1), (0,+1,+1)
		-2	(0,-1,-1), (-1,0,-1), (-1,-1,0)
3	2	+3	(+1,+1,+1)
		-3	(-1,-1,-1)

## 2.3 Results and Discussion for Phorbol Diacetate

### 2.3.1 Design of [<sup>13</sup>C, <sup>2</sup>H<sub>3</sub>]Phorbol-12,13-Diacetate for REDOR Analysis

The project was initiated with a study of PDAc because the phorbol esters are one of the most studied classes of biologically active molecules and potent PKC activators. Moreover, their activity is significantly influenced by the functionality at C12 and C13. The C12, C13 diol is inactive while the C12-tetradecanoyl, C13-acetate diester is one of the most potent known tumor promoters. In striking contrast, the C12 deoxy, C13-acetate monoester is not a tumor promoter and is a lead compound in preclinical studies for the eradication of HIV/AIDS [47, 48].

The design of the labeled PDAc included considerations of synthetic feasibility and ease of preparation together with the maximum internuclear distances that could be measured using REDOR. In addition, excluding <sup>19</sup>F and using <sup>13</sup>C and <sup>2</sup>H labels eliminated any possible perturbation of biological activity. *In silico* analysis of the phorbol ester scaffold revealed that the C12 and C13 acyloxy carbonyls are approximately  $5.0 \pm 0.5$  Å away from the  $\alpha$ -position of their counterpart, depending on the conformation of the C12 acetoxy group. Minor adjustments in this distance could arise ultimately from interactions with the peptide and lipids. This distance is within the 6-7 Å distance limit corresponding to the strength of <sup>13</sup>C-<sup>2</sup>H dipolar couplings that can be measured conveniently with REDOR. Thus, we designed a strategy to install the <sup>13</sup>C label at the C12-OAc carbonyl position, hoping that it would exhibit sufficient chemical-shift resolution to be distinguished from the natural abundance <sup>13</sup>C carbonyl contributions of the protein and lipids in the complex. Incorporation of <sup>2</sup>H was designed as a CD<sub>3</sub> group on the C13-OAc, where the REDOR-determined distance would extend from the C12 carbonyl to the average position of the three deuterons.

### **2.3.2 Preparation and NMR Characterization of Ligand-Bound PKC $\delta$ C1b in a Membrane Microenvironment**

A 51-residue peptide corresponding to the mouse PKC $\delta$  C1b domain was employed in the study given the large number of previous structural studies using this isoform [13, 15-19, 21, 22] and its ability to recapitulate the ligand binding capabilities of the full-length protein [9, 13, 15-19, 21, 22]. Previous efforts to examine C1a and C1b domain peptides of all conventional, novel, and atypical PKCs also revealed that all but one (PKC $\gamma$ ) of C1b domains, including PKC $\delta$  C1b, were comparable to the native enzymes in binding phorbol 12,13-dibutyrate (PDBu), while C1a peptides were not [22]. In addition, the C1b domain is more important for membrane binding than the C1a domain in PKC $\delta$  [49]. The C1 domain does not fold properly for binding in water but does fold in association with a phosphatidylserine vesicle [13, 21]. Thus, phosphatidylserine vesicles were used as the membrane surrogate.

To achieve maximum sensitivity for the NMR experiments, we sought to prepare a sample including as much labeled ligand bound to peptide in the NMR rotor as possible while maintaining lipid:peptide ratios that are functionally relevant. Thus, we determined the lowest lipid:peptide ratio that could be tolerated without compromising peptide function, specifically, its association with the high affinity ligand PDBu. The viability of the peptide in the various lipid:peptide ratios was assessed through radioligand binding assays traditionally used for these C1 domain peptides. However, these generally use lipid:peptide ratios of ~4300:1 [50], a ratio that would allow for only trace amounts of labeled material if it were used for the REDOR measurements. With a lipid:peptide ratio of ~4300:1, a 0.50 nM K<sub>d</sub> was obtained using standard conditions. Promisingly, a lipid:peptide ratio as low as 50:1 maintained a comparable K<sub>d</sub> value

of 1.5 nM. When the ratio was reduced to 20:1, the  $K_d$  rose to 26 nM, a considerable loss in affinity. Thus, biorelevant complexes of PKC in phosphatidylserine vesicles are achieved with high affinity at a lipid:peptide molar ratio of at least 50:1. We confirmed that binding affinity was not affected by other compositional factors, *e.g.* Tris and trehalose buffer components. The final NMR samples were prepared with ligand:peptide:phosphatidylserine:trehalose molar ratios of 1:1:50:50.

The full  $^{13}\text{C}$  spectrum of the peptide-ligand-lipid complex includes natural abundance  $^{13}\text{C}$  contributions from PKC and phosphatidylserine in addition to the labeled  $^{13}\text{C}$  carbonyl contribution from the  $[^{13}\text{C}, ^2\text{H}_3]\text{PDAC}$ , shifted upfield of the carbonyls associated with the peptide and lipids (Figure 2.4).

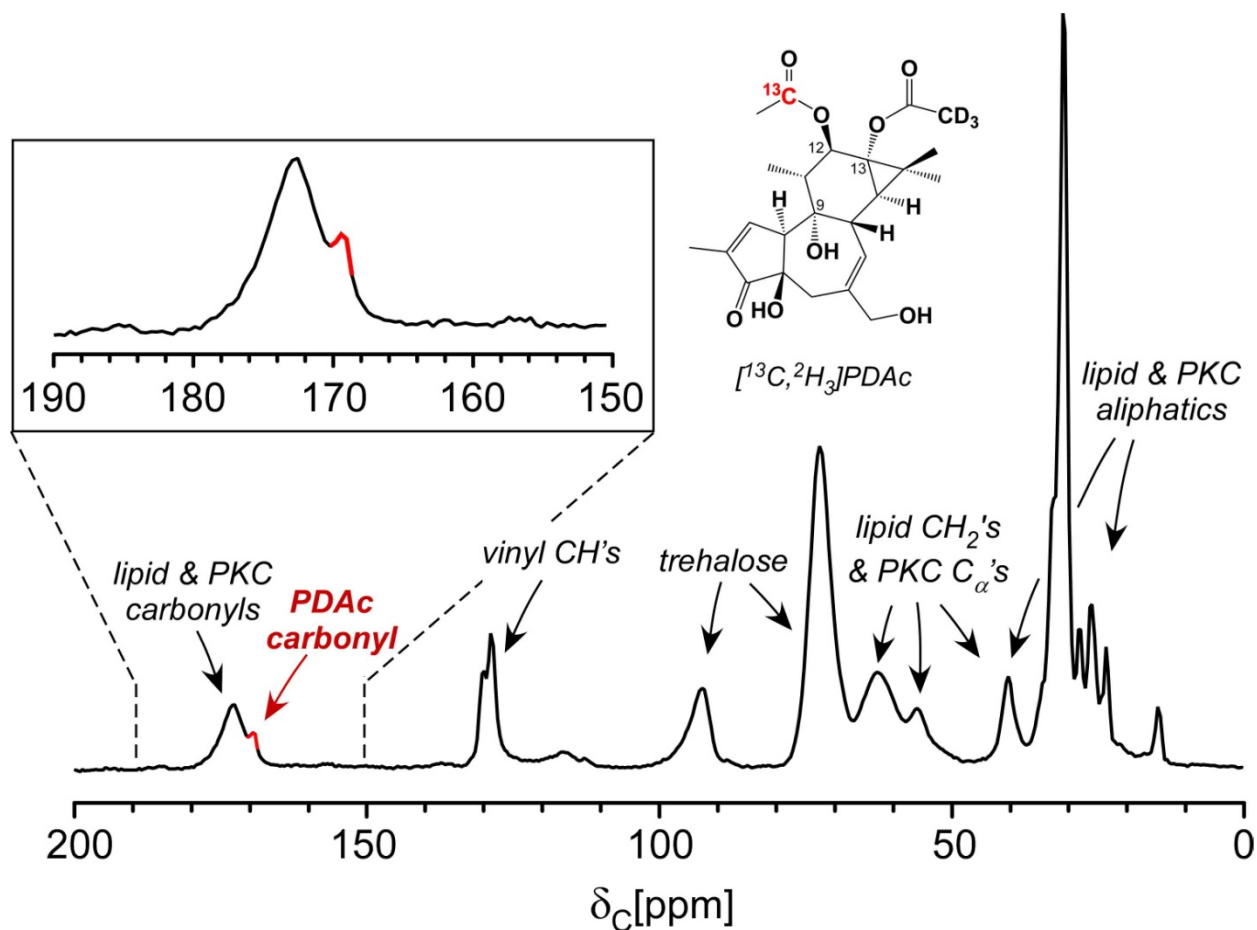


Figure 2.4  $^{13}\text{C}$  CPMAS echo spectrum of the  $[^{13}\text{C}, ^2\text{H}_3]\text{PDAc}$ -PKC-lipid complex.

The spectrum of a comparative sample of protein complexed with  $[^2\text{H}_3]\text{PDAc}$ , without the  $^{13}\text{C}$  label, confirmed the PDAc  $^{13}\text{C}$  chemical shift assignment (Figure 2.5). Thus, the ligand  $^{13}\text{C}$ -label peak was sufficiently resolved from the natural abundance background to permit  $^{13}\text{C}\{^2\text{H}\}$  REDOR measurements to determine the intramolecular  $^{13}\text{C}$ - $\text{CD}_3$  distance in the labeled PDAc.

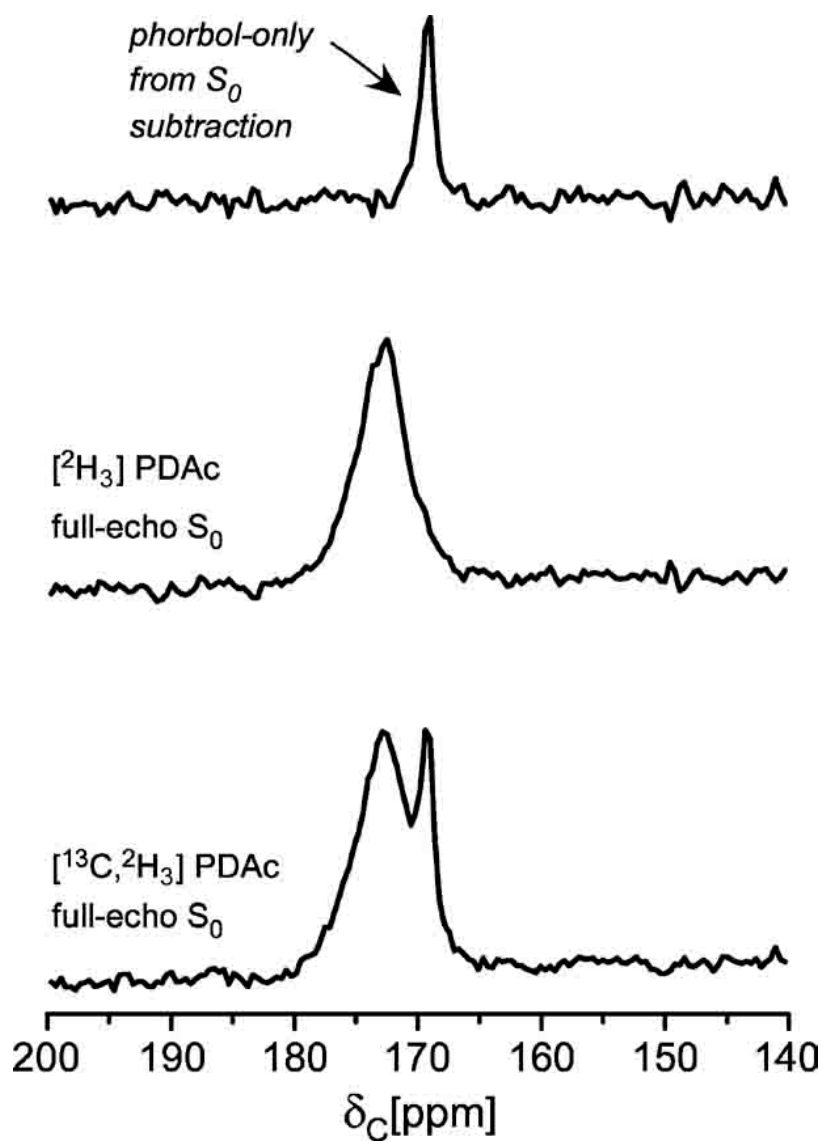


Figure 2.5  $160 T_r$  (22.4 ms)  $^{13}\text{C}\{^2\text{H}\}$ REDOR  $S_0$  spectra of  $[^{13}\text{C}, ^2\text{H}_3]$ PDAc-PKC-lipid complex and  $[^2\text{H}_3]$ PDAc-PKC-lipid complex. Their subtraction yields the phorbol-only  $S_0$ .

### 2.3.3 The $^{13}\text{C}$ - $\text{CD}_3$ Distance Determination for PKC-Bound $[^{13}\text{C}, ^2\text{H}_3]$ Phorbol-12,13-Diacetate

REDOR was used to determine the distance between the  $^{13}\text{C}$  and the average position of the  $^2\text{H}$  atoms in the  $\text{CD}_3$  group. The full-echo and REDOR difference spectra after 160 rotor periods of

evolution, corresponding to 22.4 ms, are provided in Figure 2.6. Only dephasing of the ligand  $^{13}\text{C}$  label is observed, with 42% dephasing observed after 22.4 ms of evolution. The same measurement was performed on a separate sample in which the ligand was labeled only with the  $\text{CD}_3$  group. No dephasing was observed for this sample (Figure 2.6) and demonstrates that the dephasing observed in the  $^{13}\text{C}, ^2\text{H}_3$ -labeled PDAc corresponds to the  $^{13}\text{C}$  label on the PDAc.

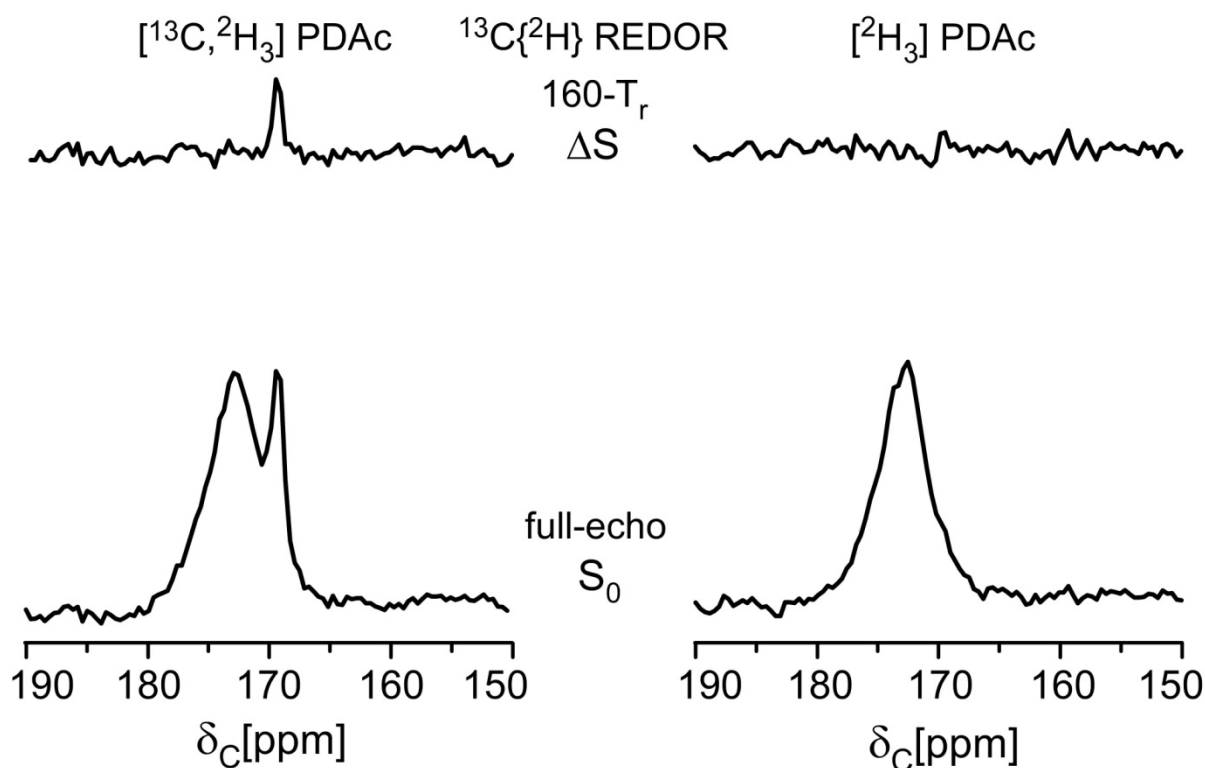


Figure 2.6  $160 T_r$  (22.4 ms)  $^{13}\text{C}\{^2\text{H}\}$  REDOR spectra of  $[^{13}\text{C}, ^2\text{H}_3]\text{PDAc}$ -PKC-lipid complex and  $[^2\text{H}_3]\text{PDAc}$ -PKC-lipid complex.

The percent dephasing ( $\Delta S/S_0$ ) for multiple evolution times were plotted and scaled uniformly to reach the maximum theoretical  $^{13}\text{C}$  dephasing of 73% caused by a combination of  $\text{CD}_3$ ,  $\text{CD}_2\text{H}$ , and  $\text{CDH}_2$  dephasers in  $[^{13}\text{C}, ^2\text{H}_3]\text{PDAc}$  (Figure 2.7). These data fit a distance of  $5.1 \pm 0.2 \text{ \AA}$

(Figure 2.7). Thus, REDOR enabled the determination of the biorelevant conformation of PDAc bound to a PKC C1b domain in a membrane microenvironment.

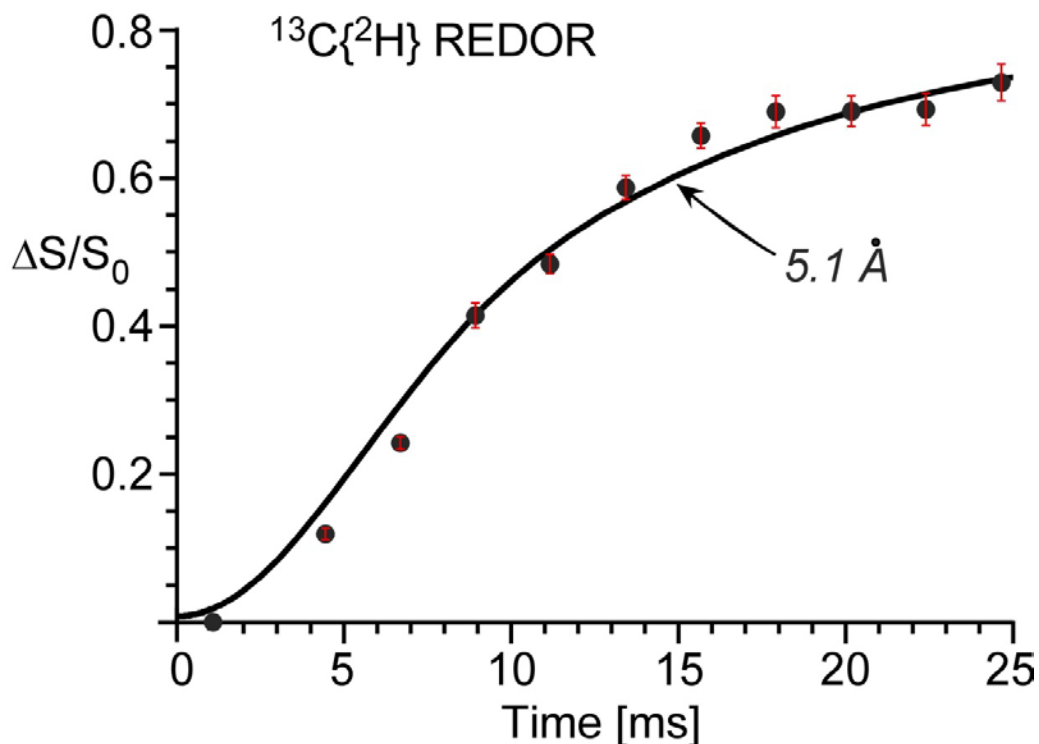


Figure 2.7  $^{13}\text{C}\{^2\text{H}\}$ REDOR data points and fitting curve of  $[^{13}\text{C}, ^2\text{H}_3]\text{PDAc-PKC-lipid}$  complex.

Approximately 140,000 scans of  $S_0$  and  $S$  were obtained at the early evolution times of 4.48 and 6.72 ms. 60,000-80,000 scans were collected for later evolution times. The acquisition of the entire REDOR curve took about two months of spectrometer time. In addition, a further amount of time was required to obtain the spectrum for the natural abundance sample.

We sought to understand why data scaling was necessary to reach the expected plateau, noting that the actual plateau is a valuable parameter provided by the REDOR experiment when the NMR sensitivity permits the collection of a full dephasing curve. Scaling REDOR data can be

necessary in certain circumstances, *e.g.* studies in which the nucleus serving as the dephaser is not 100% isotopically labeled or if each observed nucleus does not have a dephaser nearby (common in intermolecular distance measurements). In addition, molecular motion can average out the dipolar couplings to be measured and thus the observed spins would contribute to the REDOR  $S_0$  spectrum but would not exhibit dephasing. Without scaling, our data reached a plateau of only 42%, corresponding to the  $\Delta S/S_0$  of the longer evolution times of 22.4 and 24.6 ms. This reduced plateau was not anticipated, as this was an intramolecular distance measurement and nearly every PDAc contained both  $^{13}\text{C}$  and  $^2\text{H}$  labels (90%  $\text{CD}_3$  and 8.5%  $\text{CD}_2\text{H}$ , confirmed by mass spectrometry) which should yield 73% dephasing at long evolution times. REDOR experiments on [ $^{13}\text{C}$ ,  $^2\text{H}_3$ ]zinc acetate yielded the theoretically expected dephasing of 74% [46].

The incomplete dephasing is hypothesized to be attributed to mobile PDAc that was lipid associated but not peptide bound. Motion faster than the strength of the  $\sim 35$  Hz  $^{13}\text{C}$ - $^2\text{H}$  dipolar coupling would interfere with REDOR dephasing, but would allow  $^{13}\text{C}$  to still be observed in the REDOR  $S_0$  spectrum if the motion were not faster than the  $^1\text{H}$ - $^{13}\text{C}$  dipolar couplings of  $\sim 2$  kHz or were sufficiently anisotropic.

### **2.3.4 Partitioning of [ $^{13}\text{C}$ , $^2\text{H}_3$ ]Phorbol-12,13-Diacetate into a Mobile Phase**

The difference in the REDOR dephasing plateau (42% versus the theoretical maximum of 73%), suggests that approximately 42%  $[(73-42)/73]$  of the ligand is not peptide bound. To test this possibility,  $^2\text{H}$  was observed and a significant fraction of the PDAc was discovered to be mobile. As shown in Figure 2.8, a prominent centerband is observed in the  $^2\text{H}$  Hahn-echo spectrum (red),

corresponding to motional averaging of the  $^2\text{H}$  quadrupolar anisotropy. To further demonstrate the ability to use the  $^2\text{H}$  spectrum as a reporter of PDAc motion, the experiment was repeated with a shorter recycle delay of 0.5 seconds instead of 8 seconds. The immobilized peptide-bound PDAc would have a longer  $T_1$  than the mobile population and would not contribute to the Hahn echo with the shorter recycle delay. Indeed, the spectrum exhibits the anticipated major diminution of the broad sideband pattern corresponding to the rigid component relative to the mobile  $^2\text{H}$  centerband.

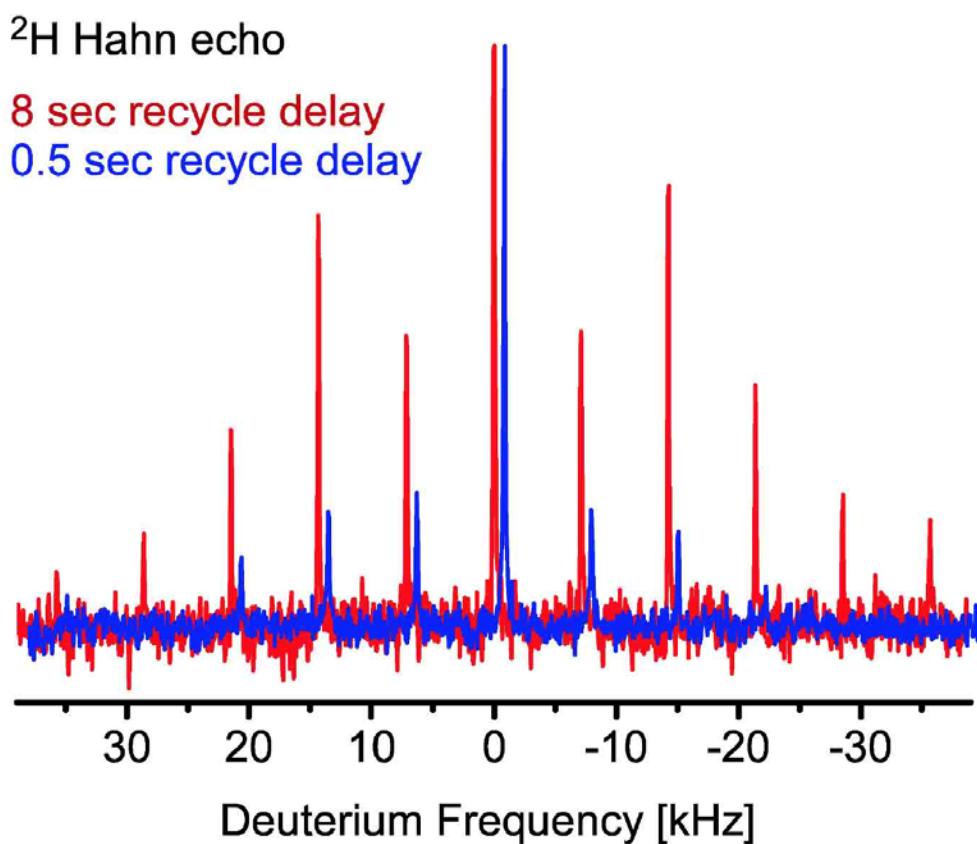


Figure 2.8  $^2\text{H}$  Hahn echo spectra of [ $^{13}\text{C}$ ,  $^2\text{H}_3$ ]PDAc-PKC-lipid complex. The blue spectrum is right shifted slightly for visual clarity.

The percentage of PDAc that is rigid and mobile can be estimated through the integrated peak intensities of the two  $^2\text{H}$  Hahn echo spectra, where the spectrum collected with an 8-second recycle delay (in red) has all PDAc contributions and the spectrum resulting from the shorter recycle delay (blue) represents only the mobile PDAc (Figure 2.8). The mobile spectrum in blue has 45% of the integrated intensity of the full 8-second Hahn echo spectrum. Thus, the rigid peptide-bound fraction is 55%. Based on this independent calculation, we would expect the REDOR data to exhibit a plateau of 40% (55% of the maximum theoretical dephasing of 73%). This is in close agreement with our experimentally determined plateau of 42%. Thus, based on our REDOR data, supported by the  $^2\text{H}$ -observe spectra reporting on PDAc motion, approximately 42% of the PDAc is mobile  $[(73-42)/73]$ . By virtue of this motion, the dipolar couplings in the mobile PDAc are averaged and cannot be measured. Thus mobile PDAc  $^{13}\text{C}$  labels contribute to  $S_0$  but are not dephased by  $^2\text{H}$ .

Control binding assays with only lipids and PDAc revealed that after the centrifugation of material, PDAc did not pellet with the lipids as it does in the presence of PKC and lipids. Thus, our results suggest that phorbol diacetate binds to PKC but, in the presence of lipids in the lyophilized formulation, exhibits a tendency to associate with lipids and dissociate from the protein. Such a phenomenon would pose a challenge for detection by other methods, including radioactivity-based binding assays which report on the differential concentrations of ligand in supernatants versus pellets (in centrifugal based assays), or above or below a filter (in filter based assays).

### 2.3.5 Conclusion for Phorbol Diacetate

The atomic-level examination of membrane-associated proteins poses a challenge to analysis by conventional methods due to the large size of protein-lipid assemblies involving bilayer and liposome preparations. Previously determined structures of PKC-ligand complexes include a PKC-phorbol-13-acetate complex with both the PKC C1b domain and ligand in the crystal structure [17] and a PKC C1 domain-PDBu complex without detection of the ligand [18]. These structures are of great value and have been employed in computational studies and drug design efforts. However, these complexes were not associated in a membrane microenvironment and, to our knowledge, a PKC-phorbol diester complex has not been reported. REDOR NMR can provide crucial atomic-level structural detail in membrane-associated systems to reveal the bioactive-bound conformations of PKC ligands such as phorbol diacetate and bryostatin.

In this work, the first structural study of the C1 binding domain of a PKC isoform in an environment other than a crystal lattice or solution was described. An intramolecular distance of peptide-bound [ $^{13}\text{C}, ^2\text{H}_3$ ]phorbol-12,13-diacetate between  $^{13}\text{C}$  and  $^2\text{H}_3$  labels complexed in lipid vesicles with a lipid:peptide molar ratio of 50:1 was determined. The distance between the PDAc C12-OAc  $^{13}\text{C}$  and the C13-OAc  $\text{CD}_3$  was measured to be  $5.1 \pm 0.2 \text{ \AA}$ . The REDOR distance is consistent with a hydrogen bond association of C9 and C13 in PDAc. Although not anticipated, a significant fraction of the PDAc in the ligand-peptide-lipid system was discovered to be not peptide-bound. Two independent measurements were employed to determine the extent of partitioning of PDAc between peptide-bound and mobile species that were in excellent agreement: (i) the experimental determination of the REDOR  $\Delta S/S_0$  plateau establishing a total accounting of the rigid ligand and (ii) the determination of the percent of the mobile ligand

through  $^2\text{H}$  Hahn echo measurements. These determinations highlight the power of REDOR and solid-state NMR to define key parameters in dynamic membrane-associated complexes. The first information toward mapping the membrane-associated structure of the PKC $\delta$  C1b domain bound to a biologically active ligand has been established by this study. This work opens new opportunities to study how structure is influenced by membrane composition, type of bound modulator, and the depth and orientation of PKC in a membrane.

## **2.4 Results and Discussion for Bryostatin**

### **2.4.1 Introduction to Bryostatin**

The study of bryostatin traces back to a Gulf of Mexico collection in 1968, aimed at providing marine organisms for the anticancer drug screen at the National Cancer Institute [51]. The initial anticancer activity displayed by marine organisms led to the isolation of the active component, bryostatin 1 (Figure 2.2, henceforth bryostatin), from the marine animal Bryozoa in 1982 [52]. The remarkable anticancer efficacy of bryostatin has led to its testing in multiple cancer clinical trials [53-55]. Recently, bryostatin has shown potential to treat neurodegenerative diseases and entered into a clinical trial on Alzheimer's disease [56]. In addition, the latest research revealed that bryostatin and its analogues can activate latent HIV-infected cells [57, 58]. This offers a promising strategy to eliminate HIV/AIDS in conjunction with the antiretroviral therapy that targets the active virus.

Bryostatin exhibits all its therapeutic effects by modulating PKC. Understanding this modulation on the molecular level is crucial for developing more potent analogues. Here we use

solid-state NMR to probe the structure and dynamics of the PKC bound bryostatin in the biorelevant membrane microenvironment. The isotopically labeled bryostatin was synthesized by the Paul Wender lab, and is carefully designed to contain a  $^{19}\text{F}$  atom, a  $^{13}\text{C}$  atom, and a  $\text{CD}_3$  group (Figure 2.9) [59].

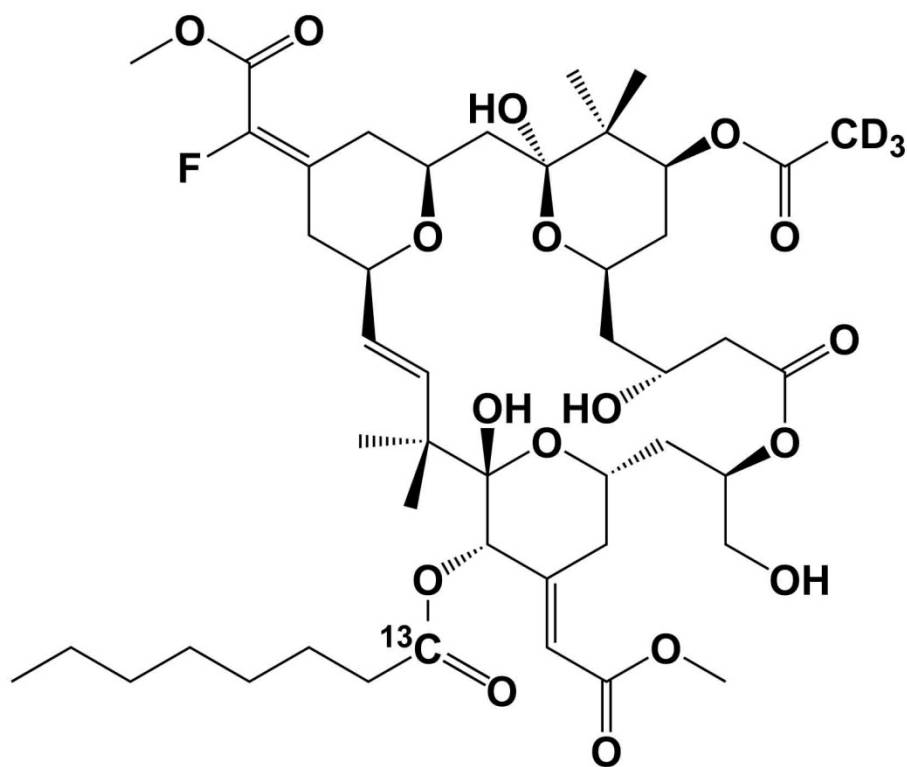


Figure 2.9 The isotopically labeled bryostatin analogue synthesized for REDOR NMR studies.

## 2.4.2 Bryostatin is Predominantly Immobile

The deuterium Hahn echo spectrum of the PKC bound bryostatin with 8 s recycle delay (Figure 2.10) indicates the bryostatin is predominantly PKC bound and immobile. Only a minor fraction of bryostatin is associated with lipids and mobile. This is evidenced by the deuterium Hahn echo spectrum which predominantly displays a Pake pattern, corresponding to the immobile bryostatin. The centerband is slightly higher than that of a Pake pattern (dotted line), indicating minor mobile bryostatin component (Figure 2.10). In contrast to phorbol diacetate (Figure 2.8), significantly more bryostatin is PKC bound than lipid associated. This observation is consistent with the fact that bryostatin has a much higher binding affinity to PKC than phorbol diacetate.

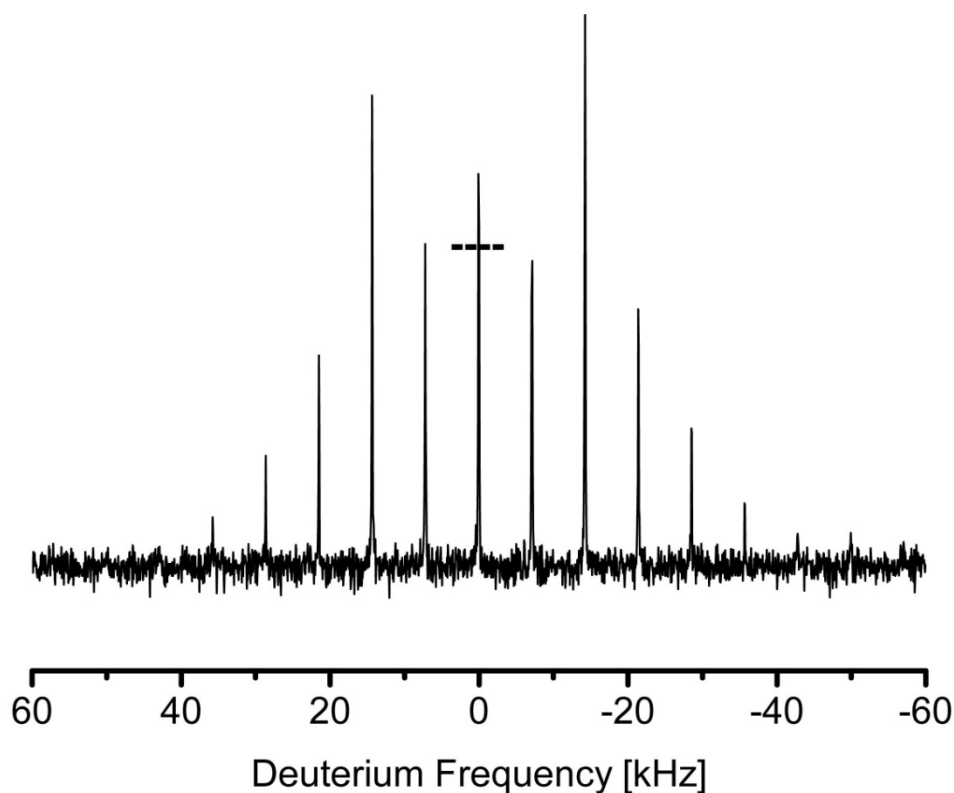


Figure 2.10 The deuterium Hahn echo spectrum of [ $^{19}\text{F}$ ,  $^{13}\text{C}$ ,  $^2\text{H}_3$ ]bryostatin-PKC-lipid complex with 8 s recycle delay.

### 2.4.3 The $^{19}\text{F}$ - $\text{CD}_3$ Distance Determination for PKC-Bound

#### $[^{19}\text{F}, ^{13}\text{C}, ^2\text{H}_3]\text{Bryostatin}$

Dephasing is observed in  $^2\text{H}\{^{19}\text{F}\}$  REDOR (Figure 2.11) which indicates the proximity of the  $^{19}\text{F}$  and  $\text{CD}_3$  group.

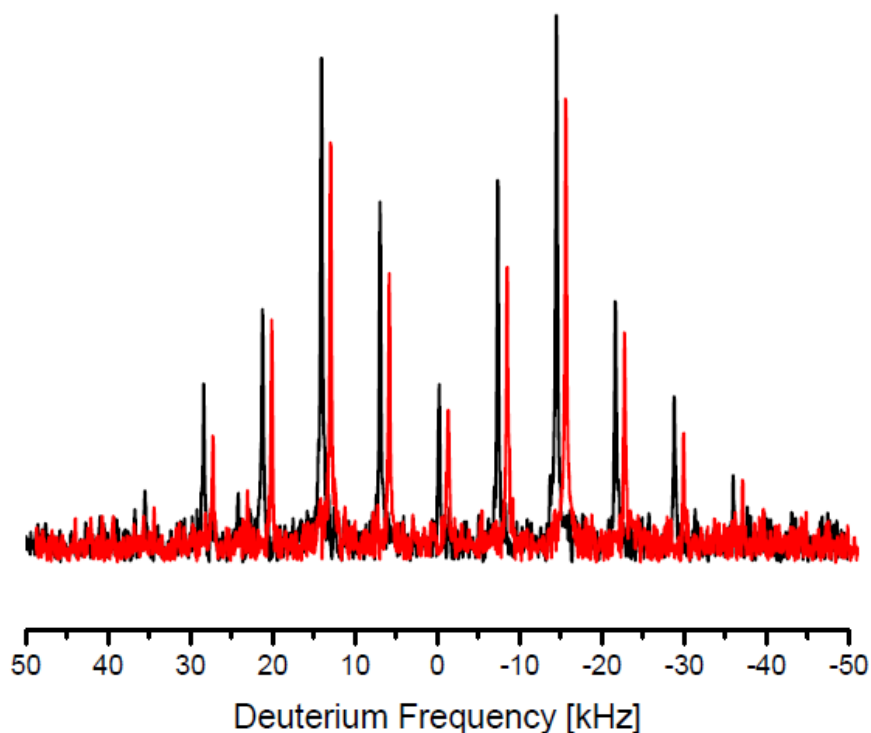


Figure 2.11  $^2\text{H}\{^{19}\text{F}\}$  REDOR spectra of  $[^{19}\text{F}, ^{13}\text{C}, ^2\text{H}_3]\text{bryostatin-PKC-lipid}$  complex at  $128 T_r$  (17.92 ms). The black spectrum is  $S_0$ , and the red one is  $S$ . The red spectrum is right shifted slightly for visual clarity. The centerband corresponding to the mobile bryostatin is not observed because cross polarization is only effective for immobile structures. Both  $S_0$  and  $S$  are magnitude spectra. The real spectra are not used because they exhibit a slight phase modulation as a result of the residual quadrupolar evolution over  $128 T_r$ . This residual quadrupolar evolution is due to the fact that the magic angle can not be set perfectly.

The  $^2\text{H}\{^{19}\text{F}\}$  REDOR data points were fit to determine the distance between the  $^{19}\text{F}$  and  $\text{CD}_3$  group. A single distance REDOR curve does not fit the data points (Figure 2.12, left). By assuming a Gaussian distribution of distances, the data points can be well fit (Figure 2.12, right).

Here the Gaussian distribution is in the form  $\frac{1}{\sigma\sqrt{2\pi}} e^{-\frac{(r-r_0)^2}{2\sigma^2}}$  with  $r_0 = 12.0 \text{ \AA}$  and  $\sigma = 4.3 \text{ \AA}$

(Figure 2.12, right inset).

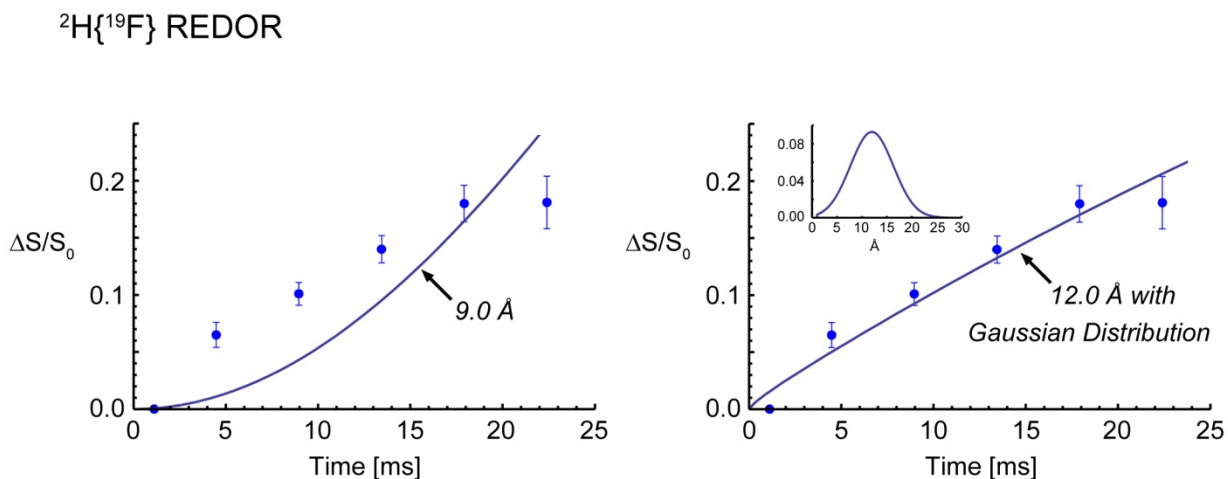


Figure 2.12  $^2\text{H}\{^{19}\text{F}\}$  REDOR data and fitting curves. REDOR curve with a single distance of  $9.0 \text{ \AA}$  (left). REDOR curve with a Gaussian distribution of distances (right). The

Gaussian distribution is in the form  $\frac{1}{\sigma\sqrt{2\pi}} e^{-\frac{(r-r_0)^2}{2\sigma^2}}$  with  $r_0 = 12.0 \text{ \AA}$  and  $\sigma = 4.3 \text{ \AA}$

(right inset). Typically, each data point in the REDOR curve was the result of the accumulation of 150,000 to 300,000 scans. The acquisition of the entire REDOR curve took two to three months of spectrometer time.

## 2.4.4 The $^{19}\text{F}$ - $^{13}\text{C}$ Distance Determination for PKC-Bound

### $[^{19}\text{F}, ^{13}\text{C}, ^2\text{H}_3]\text{Bryostatin}$

Dephasing is observed in  $^{13}\text{C}\{^{19}\text{F}\}$  REDOR (Figure 2.13) indicating the proximity of the  $^{19}\text{F}$  and  $^{13}\text{C}$  atoms.

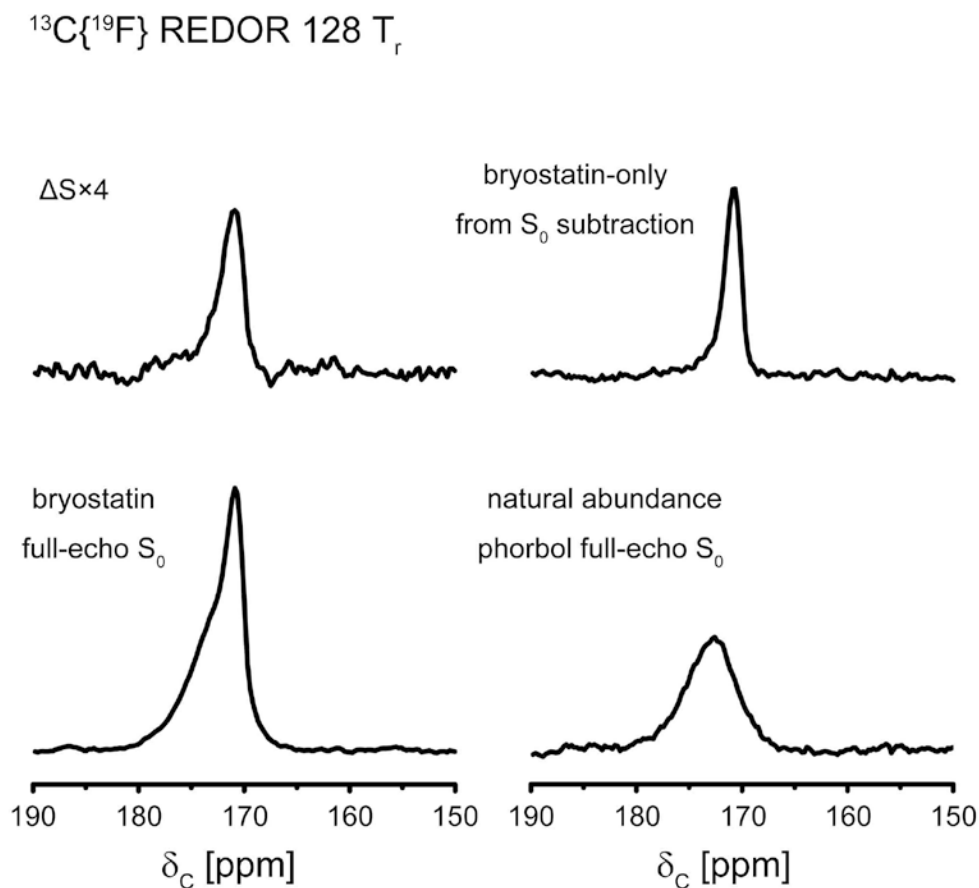


Figure 2.13  $^{13}\text{C}\{^{19}\text{F}\}$  REDOR spectra of  $[^{19}\text{F}, ^{13}\text{C}, ^2\text{H}_3]\text{bryostatin-PKC-lipid}$  complex and  $[^2\text{H}_3]\text{PDAc-PKC-lipid}$  complex at 128  $T_r$  (17.92 ms). The bryostatin full-echo  $S_0$  (bottom left spectrum) contains contributions from the  $^{13}\text{C}$  label in bryostatin and the natural abundance  $^{13}\text{C}$  from PKC and lipids. The bryostatin-only  $S_0$  (top right spectrum) is obtained by subtracting the PKC and lipids natural abundance  $^{13}\text{C}$  (using the natural abundance phorbol full-echo  $S_0$ ) from the bryostatin full-echo  $S_0$ .

The  $^{13}\text{C}\{^{19}\text{F}\}$  REDOR data points were fit to determine the distance between the  $^{13}\text{C}$  and  $^{19}\text{F}$  atoms. The REDOR data points are not well fit by a single distance REDOR curve (Figure 2.14, left). A Gaussian distribution of distances gives a much better fit (Figure 2.14, right). Here the Gaussian distribution is in the form  $\frac{1}{\sigma\sqrt{2\pi}} e^{-\left(\frac{r-r_0}{\sqrt{2}\sigma}\right)^2}$  with  $r_0 = 11.5 \text{ \AA}$  and  $\sigma = 3.0 \text{ \AA}$  (Figure 2.14, right inset).

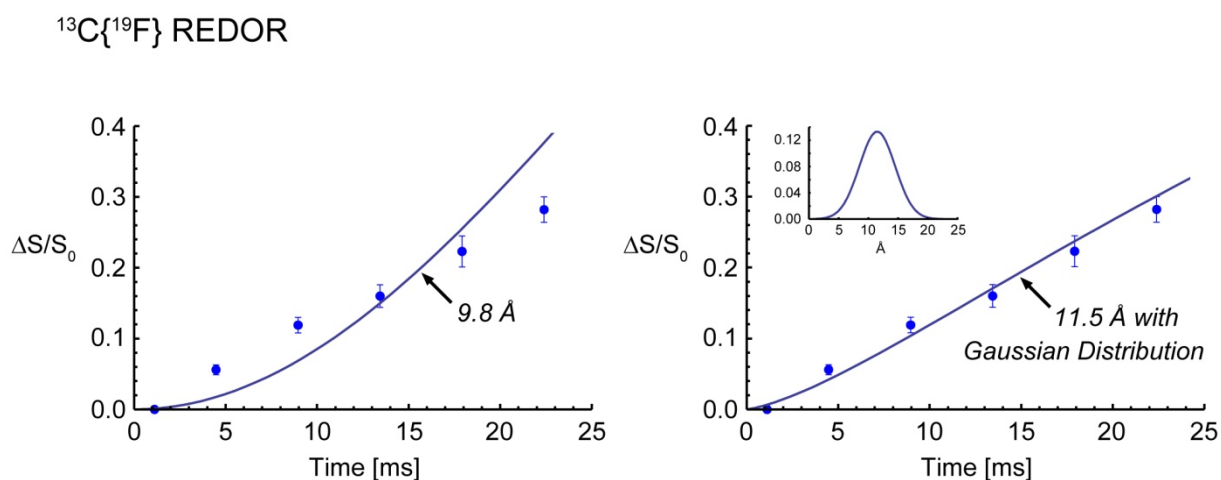


Figure 2.14  $^{13}\text{C}\{^{19}\text{F}\}$  REDOR data and fitting curves. REDOR curve with a single distance of  $9.8 \text{ \AA}$  (left). REDOR curve with a Gaussian distribution of distances (right). The Gaussian distribution is in the form  $\frac{1}{\sigma\sqrt{2\pi}} e^{-\left(\frac{r-r_0}{\sqrt{2}\sigma}\right)^2}$  with  $r_0 = 11.5 \text{ \AA}$  and  $\sigma = 3.0 \text{ \AA}$  (right inset). Typically, each data point in the REDOR curve was the result of the accumulation of 150,000 to 200,000 scans. The acquisition of the entire REDOR curve took about two months of spectrometer time. In addition, a further amount of time was required to obtain the spectrum for the natural abundance sample.

## 2.4.5 The $^{13}\text{C}$ - $\text{CD}_3$ Distance Determination for PKC-Bound

### $^{19}\text{F}$ , $^{13}\text{C}$ , $^2\text{H}_3$ Bryostatin

Dephasing is observed in  $^{13}\text{C}\{^2\text{H}\}$  REDOR (Figure 2.15) indicating the proximity of the  $^{13}\text{C}$  and  $\text{CD}_3$  group.

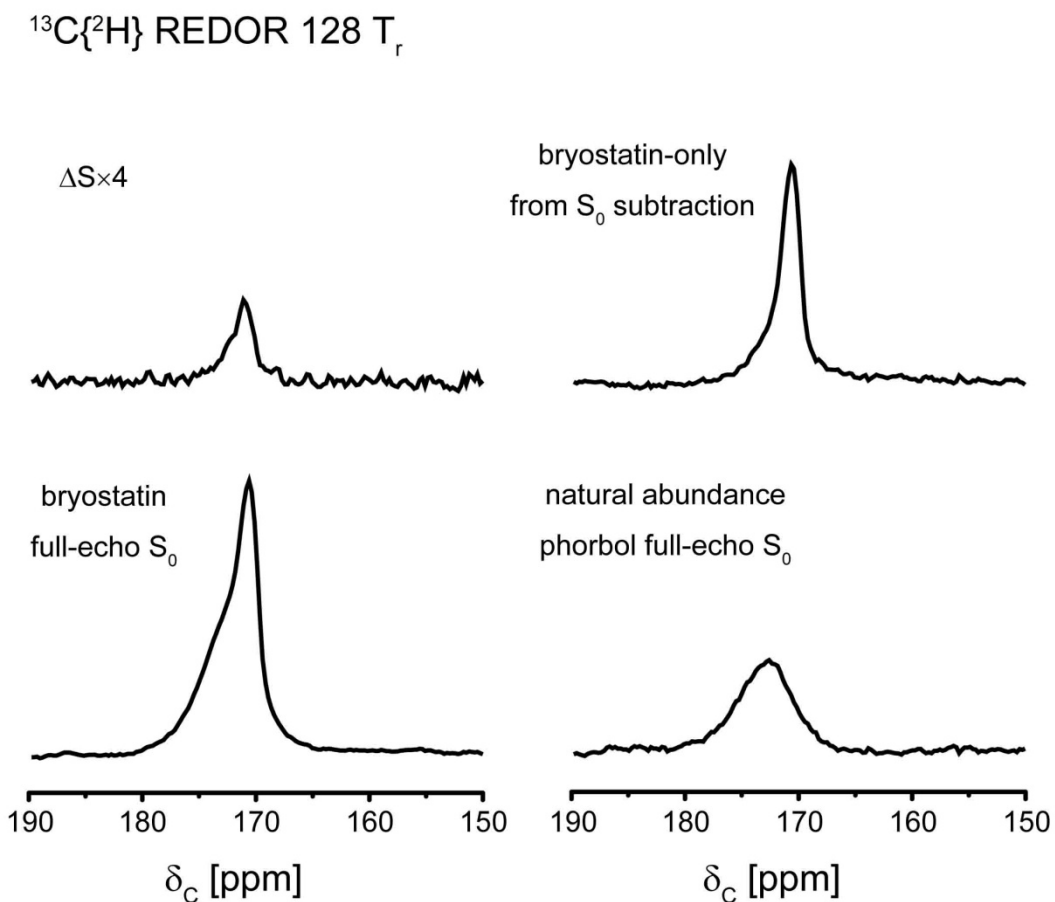


Figure 2.15  $^{13}\text{C}\{^2\text{H}\}$  REDOR spectra of  $^{19}\text{F}$ ,  $^{13}\text{C}$ ,  $^2\text{H}_3$  bryostatin-PKC-lipid complex and  $^2\text{H}_3$  PDAC-PKC-lipid complex at 128  $T_r$  (17.92 ms). The bryostatin full-echo  $S_0$  (bottom left spectrum) contains contributions from the  $^{13}\text{C}$  label in bryostatin and the natural abundance  $^{13}\text{C}$  from PKC and lipids. The bryostatin-only  $S_0$  (top right spectrum) is obtained by subtracting the PKC and lipids natural abundance  $^{13}\text{C}$  (using the natural abundance phorbol full-echo  $S_0$ ) from the bryostatin full-echo  $S_0$ .

The  $^{13}\text{C}\{^2\text{H}\}$  REDOR data points were fit to determine the distance between the  $^{13}\text{C}$  and  $\text{CD}_3$  group. By assuming a single  $^{13}\text{C}\text{-CD}_3$  distance, the  $^{13}\text{C}\{^2\text{H}\}$  REDOR data points are not well fit (Figure 2.16, left). However, using a Gaussian distribution of distances, the data points can be well fit (Figure 2.16, right). Here the Gaussian distribution is in the form  $\frac{1}{\sigma\sqrt{2\pi}} e^{-\left(\frac{r-r_0}{\sqrt{2}\sigma}\right)^2}$  with  $r_0 = 12.4 \text{ \AA}$  and  $\sigma = 4.2 \text{ \AA}$  (Figure 2.16, right inset).

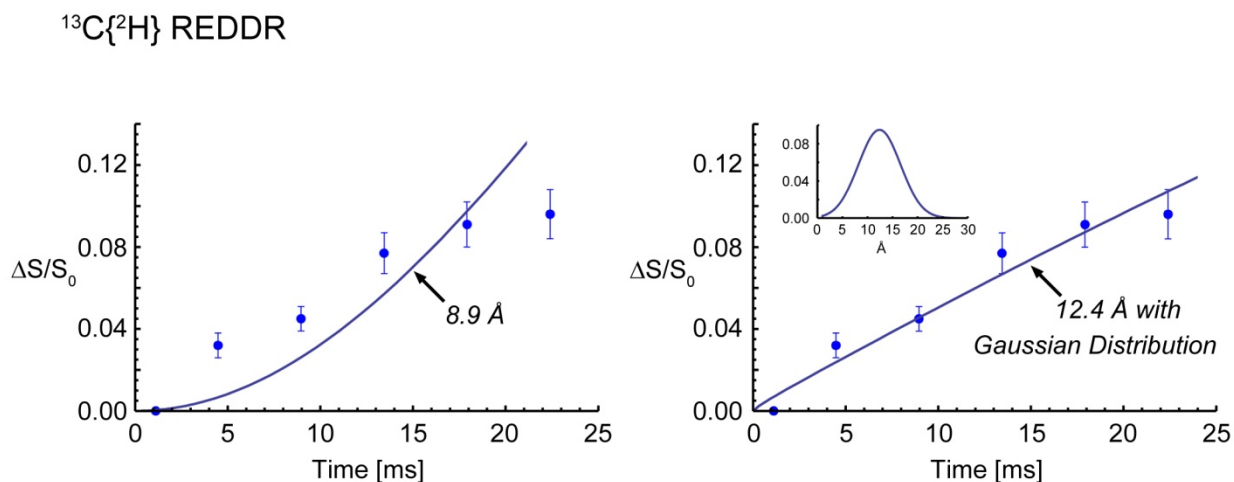


Figure 2.16  $^{13}\text{C}\{^2\text{H}\}$  REDOR data and fitting curves. REDOR curve with a single distance of  $8.9 \text{ \AA}$  (left). REDOR curve with a Gaussian distribution of distances (right). The Gaussian distribution is in the form  $\frac{1}{\sigma\sqrt{2\pi}} e^{-\left(\frac{r-r_0}{\sqrt{2}\sigma}\right)^2}$  with  $r_0 = 12.4 \text{ \AA}$  and  $\sigma = 4.2 \text{ \AA}$  (right inset). Typically, each data point in the REDOR curve was the result of the accumulation of 200,000 to 300,000 scans. The acquisition of the entire REDOR curve took about three months of spectrometer time. In addition, a further amount of time was required to obtain the spectrum for the natural abundance sample.

## 2.4.6 Conclusion for Byrostatin

In conclusion, solid-state NMR measurements have provided crucial structural information of the PKC bound bryostatin in a biorelevant membrane microenvironment. Bryostatin is found to be predominantly PKC bound, as opposed to lipid associated. The PKC bound bryostatin does not assume a single conformation as evidenced by the poor fits to the REDOR data in all cases assuming a single  $^{19}\text{F-CD}_3$ ,  $^{13}\text{C-}^{19}\text{F}$ , or  $^{13}\text{C-CD}_3$  distance. Instead, the REDOR data points in all cases are well fit by using Gaussian distributions of distances, reflecting a distribution of conformations. The REDOR results suggest that the binding site of the PKC C1b domain complexed with bryostatin but not with phorbol diacetate is probably dynamic in solution [60], and the lyophilized sample therefore contains a distribution of trapped conformations and shows a distribution of distances. This information will be used by the Wender group as constraints on molecular modeling of the PKC-bryostatin complex (Figure 2.17).

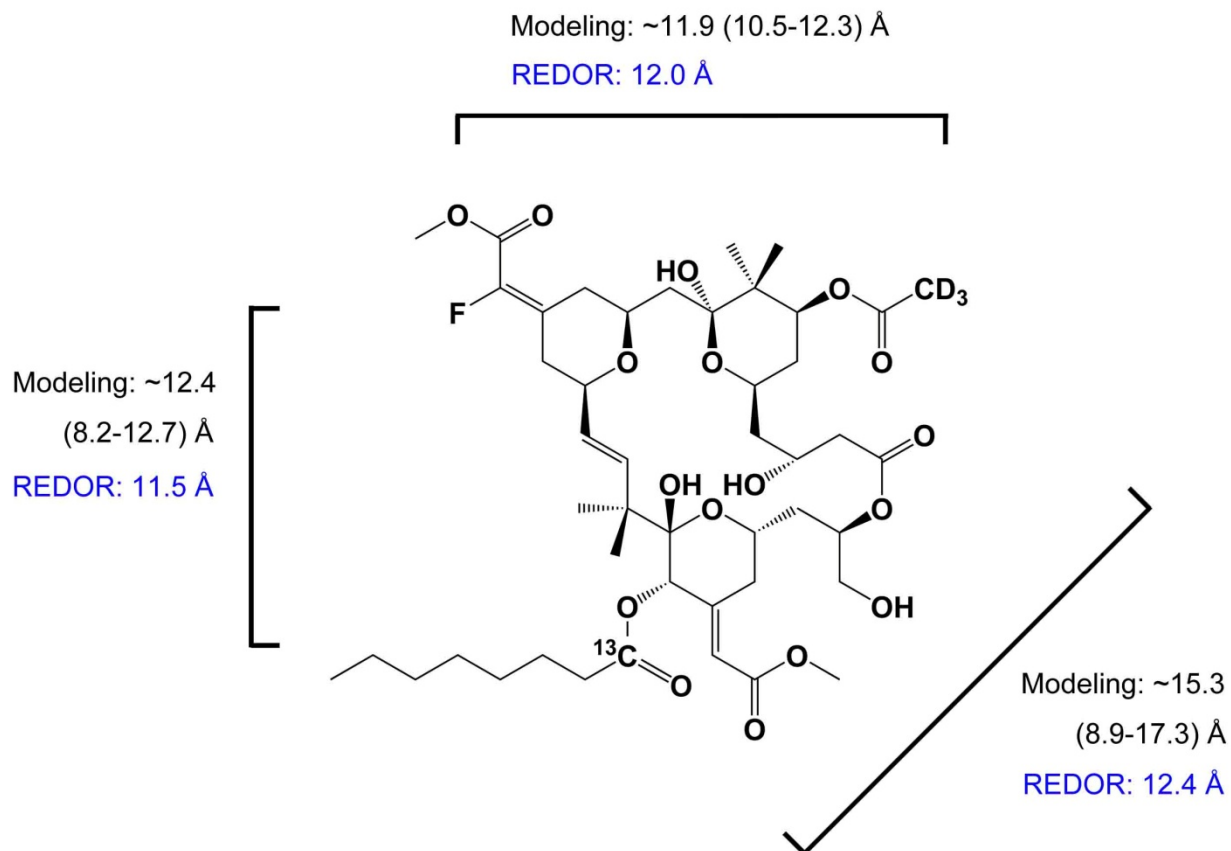


Figure 2.17 Distances between the spin pairs in [<sup>19</sup>F, <sup>13</sup>C, <sup>2</sup>H<sub>3</sub>]bryostatin from modeling and REDOR measurements, respectively. The modeling distances are from the lowest energy conformer, with a range in parenthesis representing other possible low energy conformations. The REDOR distances are the center distances of the Gaussian distributions (Figure 2.12, right; Figure 2.14, right; Figure 2.16, right). The REDOR distances will be used as constraints on molecular modeling of the PKC-bryostatin complex.

## 2.5 References

1. Inoue, M., Kishimoto, A., Takai, Y., and Nishizuka, Y., *Studies on a Cyclic Nucleotide-Independent Protein-Kinase and Its Proenzyme in Mammalian-Tissues .2. Proenzyme and Its Activation by Calcium-Dependent Protease from Rat-Brain*. Journal of Biological Chemistry, 1977. **252**(21): 7610-7616.
2. Nakamura, S. and Yamamura, H., *Yasutomi Nishizuka: Father of Protein Kinase C*. Journal of Biochemistry, 2010. **148**(2): 125-130.
3. Newton, A.C., *Protein Kinase C: Poised to Signal*. American Journal of Physiology-Endocrinology and Metabolism, 2010. **298**(3): E395-E402.
4. Mochly-Rosen, D., Das, K., and Grimes, K.V., *Protein Kinase C, an Elusive Therapeutic Target?* Nature Reviews Drug Discovery, 2012. **11**(12): 937-957.
5. Newton, A.C., *Protein Kinase C: Structural and Spatial Regulation by Phosphorylation, Cofactors, and Macromolecular Interactions*. Chemical Reviews, 2001. **101**(8): 2353-2364.
6. Gallegos, L.L. and Newton, A.C., *Spatiotemporal Dynamics of Lipid Signaling: Protein Kinase C as a Paradigm*. Iubmb Life, 2008. **60**(12): 782-789.
7. Rosse, C., Linch, M., Kermorgant, S., Cameron, A.J.M., Boeckeler, K., and Parker, P.J., *PKC and the Control of Localized Signal Dynamics*. Nature Reviews Molecular Cell Biology, 2010. **11**(2): 103-112.
8. Das, J. and Rahman, G.M., *CI Domains: Structure and Ligand-Binding Properties*. Chemical Reviews, 2014. **114**(24): 12108-12131.

9. Irie, K. and Yanagita, R.C., *Synthesis and Biological Activities of Simplified Analogs of the Natural PKC Ligands, Bryostatin-1 and Aplysiatoxin*. *Chemical Record*, 2014. **14**(2): 251-267.
10. Wender, P.A., Donnelly, A.C., Loy, B.A., Near, K.E., and Staveness, D., *Rethinking the Role of Natural Products: Function-Oriented Synthesis, Bryostatin, and Bryologs*, in *Natural Products in Medicinal Chemistry*. 2014, Wiley-VCH Verlag GmbH & Co. KGaA. p. 473-544.
11. Wender, P.A., Loy, B.A., and Schrier, A.J., *Translating Nature's Library: The Bryostatins and Function-Oriented Synthesis*. *Israel Journal of Chemistry*, 2011. **51**(3-4): 453-472.
12. Wender, P.A., Baryza, J.L., Brenner, S.E., DeChristopher, B.A., Loy, B.A., Schrier, A.J., and Verma, V.A., *Design, Synthesis, and Evaluation of Potent Bryostatin Analogs That Modulate PKC Translocation Selectivity*. *Proceedings of the National Academy of Sciences of the United States of America*, 2011. **108**(17): 6721-6726.
13. Rahman, G.M., Shanker, S., Lewin, N.E., Kedei, N., Hill, C.S., Prasad, B.V.V., Blumberg, P.M., and Das, J., *Identification of the Activator-Binding Residues in the Second Cysteine-Rich Regulatory Domain of Protein Kinase C Theta (PKC Theta)*. *Biochemical Journal*, 2013. **451**: 33-44.
14. Ziemba, B.P. and Falke, J.J., *Lateral Diffusion of Peripheral Membrane Proteins on Supported Lipid Bilayers Is Controlled by the Additive Frictional Drags of (1) Bound Lipids and (2) Protein Domains Penetrating into the Bilayer Hydrocarbon Core*. *Chemistry and Physics of Lipids*, 2013. **172**: 67-77.

15. Hommel, U., Zurini, M., and Luyten, M., *Solution Structure of a Cysteine-Rich Domain of Rat Protein-Kinase-C*. *Nature Structural Biology*, 1994. **1**(6): 383-387.
16. Ichikawa, S., Hatanaka, H., Takeuchi, Y., Ohno, S., and Inagaki, F., *Solution Structure of Cysteine-Rich Domain of Protein-Kinase C-Alpha*. *Journal of Biochemistry*, 1995. **117**(3): 566-574.
17. Zhang, G.G., Kazanietz, M.G., Blumberg, P.M., and Hurley, J.H., *Crystal-Structure of the Cys2 Activator-Binding Domain of Protein-Kinase C-Delta in Complex with Phorbol Ester*. *Cell*, 1995. **81**(6): 917-924.
18. Xu, R.X., Pawelczyk, T., Xia, T.H., and Brown, S.C., *NMR Structure of a Protein Kinase C-Gamma Phorbol-Binding Domain and Study of Protein-Lipid Micelle Interactions*. *Biochemistry*, 1997. **36**(35): 10709-10717.
19. Shanmugasundararaj, S., Das, J., Sandberg, W.S., Zhou, X.J., Wang, D., Messing, R.O., Bruzik, K.S., Stehle, T., and Miller, K.W., *Structural and Functional Characterization of an Anesthetic Binding Site in the Second Cysteine-Rich Domain of Protein Kinase C Delta*. *Biophysical Journal*, 2012. **103**(11): 2331-2340.
20. Leonard, T.A., Rozycki, B., Saidi, L.F., Hummer, G., and Hurley, J.H., *Crystal Structure and Allosteric Activation of Protein Kinase C Beta II*. *Cell*, 2011. **144**(1): 55-66.
21. Wender, P.A., Irie, K., and Miller, B.L., *Identification, Activity, and Structural Studies of Peptides Incorporating the Phorbol Ester-Binding Domain of Protein-Kinase-C*. *Proceedings of the National Academy of Sciences of the United States of America*, 1995. **92**(1): 239-243.
22. Irie, K., Oie, K., Nakahara, A., Yanai, Y., Ohigashi, H., Wender, P.A., Fukuda, H., Konishi, H., and Kikkawa, U., *Molecular Basis for Protein Kinase C Isozyme-Selective*

- Binding: The Synthesis, Folding, and Phorbol Ester Binding of the Cysteine-Rich Domains of All Protein Kinase C Isozymes*. Journal of the American Chemical Society, 1998. **120**(36): 9159-9167.
23. Chen, Y.K., Zhang, Z.F., Tang, X.Q., Li, J.P., Glaubitz, C., and Yang, J., *Conformation and Topology of Diacylglycerol Kinase in E. Coli Membranes Revealed by Solid-State NMR Spectroscopy*. Angewandte Chemie-International Edition, 2014. **53**(22): 5624-5628.
24. Gullion, T. and Schaefer, J., *Rotational-Echo Double-Resonance NMR*. Journal of Magnetic Resonance, 1989. **81**(1): 196-200.
25. Pan, Y., Gullion, T., and Schaefer, J., *Determination of C-N Internuclear Distances by Rotational-Echo Double-Resonance NMR of Solids*. Journal of Magnetic Resonance, 1990. **90**(2): 330-340.
26. Matsuoka, S. and Inoue, M., *Application of REDOR NMR in Natural Product Chemistry*. Chemical Communications, 2009(38): 5664-5675.
27. Toke, O. and Cegelski, L., *REDOR Applications in Biology: An Overview*. Solid State NMR Studies of Biopolymers, 2010. **2**: 473-490.
28. Cegelski, L., *REDOR NMR for Drug Discovery*. Bioorganic & Medicinal Chemistry Letters, 2013. **23**(21): 5767-5775.
29. Louie, E.A., Chirakul, P., Raghunathan, V., Sigurdsson, S.T., and Drobny, G.P., *Using Solid-State  $^{31}\text{P}\{^{19}\text{F}\}$  REDOR NMR to Measure Distances between a Trifluoromethyl Group and a Phosphodiester in Nucleic Acids*. Journal of Magnetic Resonance, 2006. **178**(1): 11-24.

30. Studelska, D.R., Klug, C.A., Beusen, D.D., McDowell, L.M., and Schaefer, J., *Long-Range Distance Measurements of Protein Binding Sites by Rotational-Echo Double-Resonance NMR*. Journal of the American Chemical Society, 1996. **118**(23): 5476-5477.
31. Wang, J.X., Balazs, Y.S., and Thompson, L.K., *Solid-State REDOR NMR Distance Measurements at the Ligand Site of a Bacterial Chemotaxis Membrane Receptor*. Biochemistry, 1997. **36**(7): 1699-1703.
32. Watts, J.A., Watts, A., and Middleton, D.A., *A Model of Reversible Inhibitors in the Gastric H<sup>+</sup>/K<sup>+</sup>-ATPase Binding Site Determined by Rotational Echo Double Resonance NMR*. Journal of Biological Chemistry, 2001. **276**(46): 43197-43204.
33. Getmanova, E., Patel, A.B., Klein-Seetharaman, J., Loewen, M.C., Reeves, P.J., Friedman, N., Sheves, M., Smith, S.O., and Khorana, H.G., *NMR Spectroscopy of Phosphorylated Wild-Type Rhodopsin: Mobility of the Phosphorylated C-Terminus of Rhodopsin in the Dark and Upon Light Activation*. Biochemistry, 2004. **43**(4): 1126-1133.
34. Werner, K., Lehner, I., Dhiman, H.K., Richter, C., Glaubitz, C., Schwalbe, H., Klein-Seetharaman, J., and Khorana, H.G., *Combined Solid State and Solution NMR Studies of Alpha,Epsilon-<sup>15</sup>N Labeled Bovine Rhodopsin*. Journal of Biomolecular NMR, 2007. **37**(4): 303-312.
35. Cady, S.D., Schmidt-Rohr, K., Wang, J., Soto, C.S., DeGrado, W.F., and Hong, M., *Structure of the Amantadine Binding Site of Influenza M2 Proton Channels in Lipid Bilayers*. Nature, 2010. **463**(7281): 689-U127.
36. Li, Y.K., Poliks, B., Cegelski, L., Poliks, M., Gryczynski, Z., Piszczek, G., Jagtap, P.G., Studelska, D.R., Kingston, D.G.I., Schaefer, J., and Bane, S., *Conformation of*

- Microtubule-Bound Paclitaxel Determined by Fluorescence Spectroscopy and REDOR NMR.* Biochemistry, 2000. **39**(2): 281-291.
37. Middleton, D.A., Rankin, S., Esmann, M., and Watts, A., *Structural Insights into the Binding of Cardiac Glycosides to the Digitalis Receptor Revealed by Solid-State NMR.* Proceedings of the National Academy of Sciences of the United States of America, 2000. **97**(25): 13602-13607.
38. Paik, Y., Yang, C., Metaferia, B., Tang, S.B., Bane, S., Ravindra, R., Shanker, N., Alcaraz, A.A., Johnson, S.A., Schaefer, J., O'Connor, R.D., Cegelski, L., Snyder, J.P., and Kingston, D.G.I., *Rotational-Echo Double-Resonance NMR Distance Measurements for the Tubulin-Bound Paclitaxel Conformation.* Journal of the American Chemical Society, 2007. **129**(2): 361-370.
39. Morcombe, C.R. and Zilm, K.W., *Chemical Shift Referencing in MAS Solid State NMR.* Journal of Magnetic Resonance, 2003. **162**(2): 479-486.
40. Stueber, D., Mehta, A.K., Chen, Z.Y., Wooley, K.L., and Schaefer, J., *Local Order in Polycarbonate Glasses by  $^{13}\text{C}\{^{19}\text{F}\}$  Rotational-Echo Double-Resonance NMR.* Journal of Polymer Science Part B-Polymer Physics, 2006. **44**(19): 2760-2775.
41. Gullion, T., Baker, D.B., and Conradi, M.S., *New, Compensated Carr-Purcell Sequences.* Journal of Magnetic Resonance, 1990. **89**(3): 479-484.
42. Gullion, T. and Schaefer, J., *Elimination of Resonance Offset Effects in Rotational-Echo, Double-Resonance NMR.* Journal of Magnetic Resonance, 1991. **92**(2): 439-442.
43. Weldeghiorghis, T.K. and Schaefer, J., *Compensating for Pulse Imperfections in REDOR.* Journal of Magnetic Resonance, 2003. **165**(2): 230-236.

44. Mueller, K.T., Jarvie, T.P., Aurentz, D.J., and Roberts, B.W., *The REDOR Transform - Direct Calculation of Internuclear Couplings from Dipolar-Dephasing NMR Data*. Chemical Physics Letters, 1995. **242**(6): 535-542.
45. Schmidt, A., McKay, R.A., and Schaefer, J., *Internuclear Distance Measurement between Deuterium ( $I = 1$ ) and a Spin-1/2 Nucleus in Rotating Solids*. Journal of Magnetic Resonance, 1992. **96**(3): 644-650.
46. Schmidt, A., Kowalewski, T., and Schaefer, J., *Local Packing in Glassy Polycarbonate by Carbon Deuterium REDOR NMR*. Macromolecules, 1993. **26**(7): 1729-1733.
47. Wender, P.A., Kee, J.M., and Warrington, J.M., *Practical Synthesis of Prostratin, DPP, and Their Analogs, Adjuvant Leads against Latent HIV*. Science, 2008. **320**(5876): 649-652.
48. Beans, E.J., Fournogerakis, D., Gauntlett, C., Heumann, L.V., Kramer, R., Marsden, M.D., Murray, D., Chun, T.W., Zack, J.A., and Wender, P.A., *Highly Potent, Synthetically Accessible Prostratin Analogs Induce Latent HIV Expression in Vitro and Ex Vivo*. Proceedings of the National Academy of Sciences of the United States of America, 2013. **110**(29): 11698-11703.
49. Antal, C.E., Violin, J.D., Kunkel, M.T., Skovso, S., and Newton, A.C., *Intramolecular Conformational Changes Optimize Protein Kinase C Signaling*. Chemistry & Biology, 2014. **21**(4): 459-469.
50. Irie, K., Nakahara, A., Nakagawa, Y., Ohigashi, H., Shindo, M., Fukuda, H., Konishi, H., Kikkawa, U., Kashiwagi, K., and Saito, N., *Establishment of a Binding Assay for Protein Kinase C Isozymes Using Synthetic C1 Peptides and Development of New Medicinal*

- Leads with Protein Kinase C Isozyme and C1 Domain Selectivity*. Pharmacology & Therapeutics, 2002. **93**(2-3): 271-281.
51. Halford, B., *The Bryostatin's Tale*. Chemical & Engineering News, 2011. **89**(43): 10-17.
52. Pettit, G.R., Herald, C.L., Doubek, D.L., Herald, D.L., Arnold, E., and Clardy, J., *Anti-Neoplastic Agents .86. Isolation and Structure of Bryostatin-1*. Journal of the American Chemical Society, 1982. **104**(24): 6846-6848.
53. Kortmansky, J. and Schwartz, G.K., *Bryostatin-1: A Novel PKC Inhibitor in Clinical Development*. Cancer Investigation, 2003. **21**(6): 924-936.
54. Barr, P.M., Lazarus, H.M., Cooper, B.W., Schluchter, M.D., Panneerselvam, A., Jacobberger, J.W., Hsu, J.W., Janakiraman, N., Simic, A., Dowlati, A., and Remick, S.C., *Phase II Study of Bryostatin 1 and Vincristine for Aggressive Non-Hodgkin Lymphoma Relapsing after an Autologous Stem Cell Transplant*. American Journal of Hematology, 2009. **84**(8): 484-487.
55. Gennas, G.B., Talman, V., Yli-Kauhaluoma, J., Tuominen, R.K., and Ekokoski, E., *Current Status and Future Prospects of C1 Domain Ligands as Drug Candidates*. Current Topics in Medicinal Chemistry, 2011. **11**(11): 1370-1392.
56. *A Study Assessing Bryostatin in the Treatment of Moderately Severe to Severe Alzheimer's Disease* (NCT02431468). 2015-2017, <https://clinicaltrials.gov>.
57. Mehla, R., Bivalkar-Mehla, S., Zhang, R.N., Handy, I., Albrecht, H., Giri, S., Nagarkatti, P., Nagarkatti, M., and Chauhan, A., *Bryostatin Modulates Latent HIV-1 Infection Via PKC and AMPK Signaling but Inhibits Acute Infection in a Receptor Independent Manner*. Plos One, 2010. **5**(6).

58. DeChristopher, B.A., Loy, B.A., Marsden, M.D., Schrier, A.J., Zack, J.A., and Wender, P.A., *Designed, Synthetically Accessible Bryostatin Analogues Potently Induce Activation of Latent HIV Reservoirs in Vitro*. *Nature Chemistry*, 2012. **4**(9): 705-710.
59. Loy, B.A., Lesser, A.B., Staveness, D., Billingsley, K.L., Cegelski, L., and Wender, P.A., *Toward a Biorelevant Structure of Protein Kinase C Bound Modulators: Design, Synthesis, and Evaluation of Labeled Bryostatin Analogues for Analysis with Rotational Echo Double Resonance NMR Spectroscopy*. *Journal of the American Chemical Society*, 2015. **137**(10): 3678-3685.
60. Forman-Kay, J.D. and Mittag, T., *From Sequence and Forces to Structure, Function, and Evolution of Intrinsically Disordered Proteins*. *Structure*, 2013. **21**(9): 1492-1499.

# Chapter 3

## Characterization of the Peptidoglycan Tertiary Structure of *Enterococcus faecalis*

### 3.1 Introduction

Enterococci have emerged as the leading hospital acquired pathogens in recent years. However, from their first description in 1899 [1] until the 1970s, enterococci had been considered as generally harmless commensals of the gastrointestinal (GI) tract of humans and other mammals, birds, insects, *etc.* [2, 3], only causing opportunistic infections sporadically [1, 2]. In the middle to late 1970s, enterococci began to be isolated as common causes of hospital acquired infections [4]. In 1988, the first vancomycin resistant enterococci (VRE) were reported in the United Kingdom and France [5, 6]. Since then, enterococci have developed to be the leading causes of nosocomial infections, ranking as the second most cause of urinary tract and wound infections, and the third most cause of bacteremia in the United States [3, 4]. Among all the *Enterococcus* species, only two are responsible for almost all clinical infections: *E. faecalis* (Figure 3.1) and *E. faecium* [3, 4]. From 01/01/2010 to 06/30/2012, a total 84,050 enterococcal infections were reported in the United States, including 9,309 bloodstream isolates, 54,709 urinary-tract isolates, and 20,032 wound isolates [3]. *E. faecalis* accounted for 76% of these enterococcal infections,

while *E. faecium* accounted for 24%. Out of the total 84,050 infections, 20.6% (17,360) are vancomycin resistant. Among all the VRE isolates, 75% (14,998) are *E. faecium*, and the rest are *E. faecalis*.

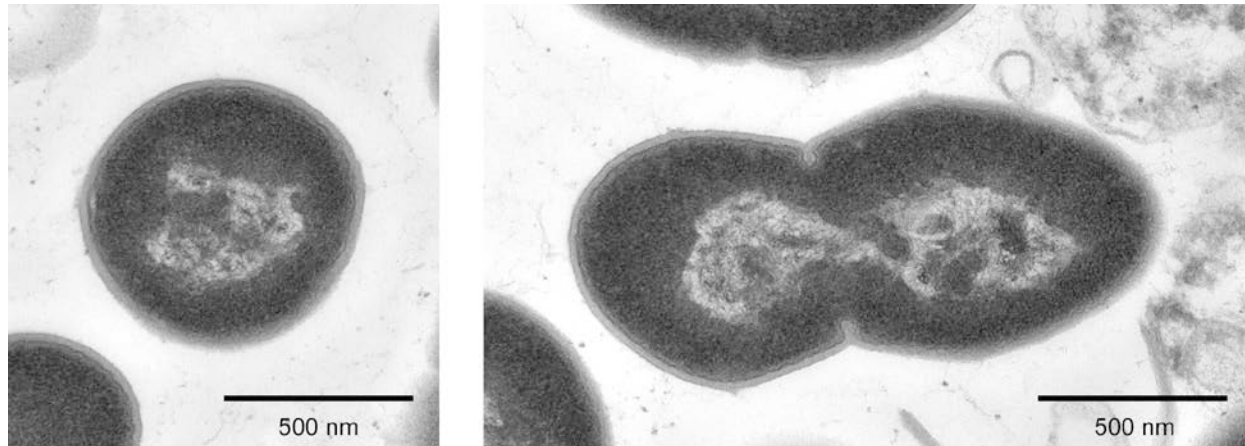


Figure 3.1 Transmission electron microscopy (TEM) of *E. faecalis* (ATCC 29212).

Enterococci can survive under adverse conditions, including high salt environments and at a broad range of temperatures (from 10 °C to > 45 °C) [7, 8]. Historically, Sherman recommended use of the name "enterococcus" to represent streptococci that grow at pH 9.6, in 6.5% NaCl, at both 10 and 45 °C, and survive at 60 °C for 30 min [4, 9]. In addition to their sturdy nature, enterococci are intrinsically resistant to several commonly used antibiotics, and are able to acquire resistance to almost all currently available antibiotics [4], including the drug of last resort, vancomycin.

The enterococcus cell wall is an important target for many antibiotics including vancomycin. The main components of the cell wall are peptidoglycan (PG) and wall teichoic acids (WTA). Figure 3.2 illustrates the chemical structure of the peptidoglycan and wall teichoic acids of *E. faecalis*.

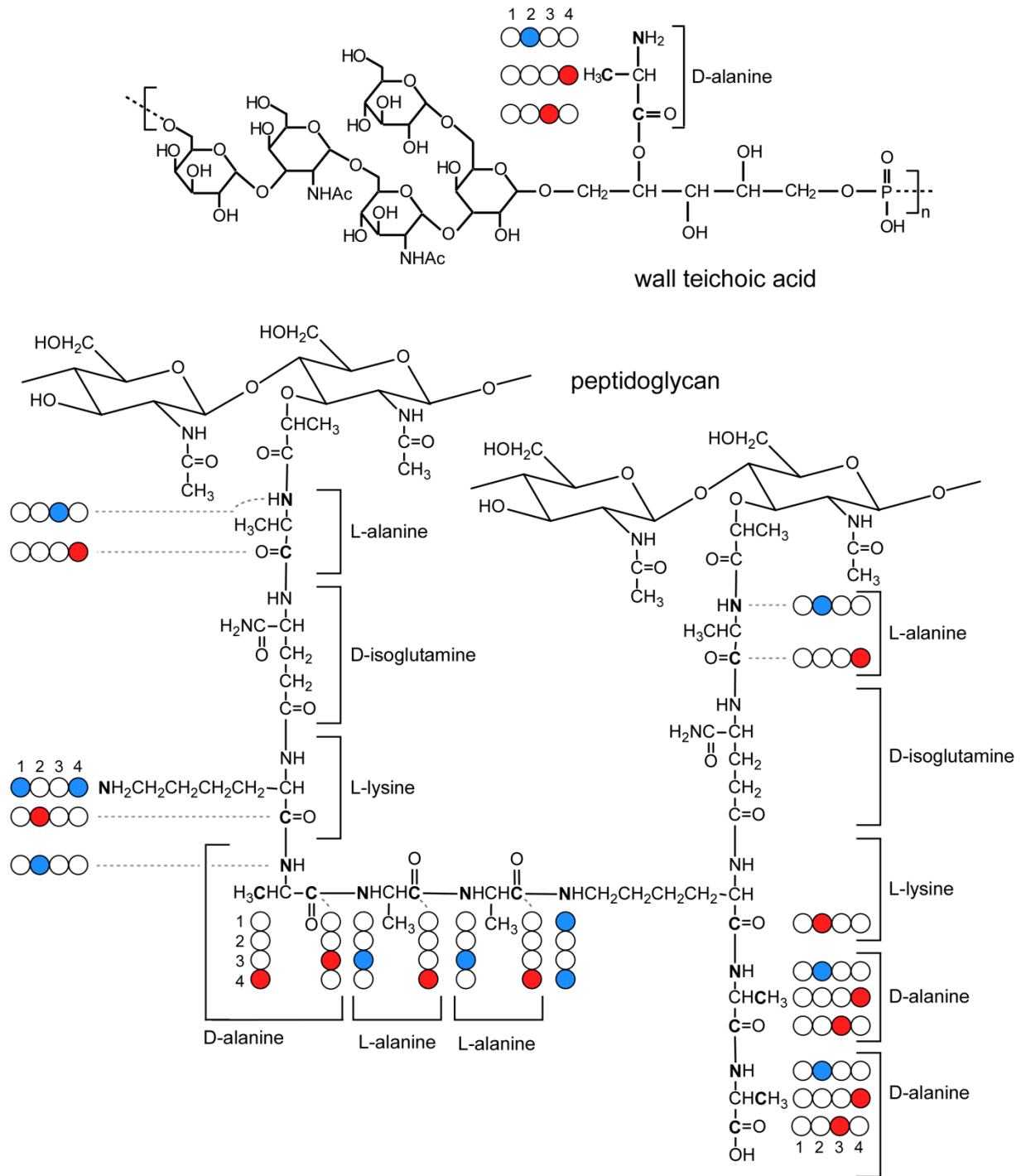


Figure 3.2 Chemical structures of wall teichoic acid (top) and peptidoglycan (bottom) of *E. faecalis*. The stable-isotope labeling of the four whole-cell and cell-wall samples of Table 3.2 is indicated by circles: open, natural abundance; red,  $^{13}\text{C}$ ; and blue,  $^{15}\text{N}$ .

Peptidoglycan is a lattice structure assembled from PG-repeat units, each consisting of a disaccharide, a stem, and a bridge (Figure 3.2). The disaccharide *N*-acetylglucosamine (GlcNAc) and *N*-acetylmuramic acid (MurNAc) are connected by a  $\beta(1-4)$  glycosidic bond. The *E. faecalis* PG stem is L-Ala-D-iso-Gln-L-Lys-D-Ala-D-Ala, and the bridge is L-Ala-L-Ala (Figure 3.2). The bridge is attached to the  $\epsilon$ -nitrogen side chain of L-lysine of the stem. The peptidoglycan lattice is assembled from the PG-repeat units by transglycosylase and transpeptidase. Transglycosylase polymerizes the PG-repeat units along the disaccharides to form a glycan chain. Transpeptidase interconnects the glycan chains by forming a peptide bond (cross-linking) between the N-terminus of L-alanine of a bridge in one PG unit to the C-terminus of the penultimate D-alanine of a stem in another PG unit from neighboring glycan chain. During the cross-linking, the terminal D-alanine (the 5th amino acid) from the acceptor stem is cleaved. The vancomycin resistant enterococci modify the vancomycin binding site, D-alanine-D-alanine (terminal residues of stem), to D-alanine-D-lactate, resulting in a 1000-fold decrease in binding affinity [10].

The bacterial cell wall is crucial to maintaining the integrity of the cell structure, and is also an important target of antibiotics. However, the tertiary structure of bacterial cell walls is poorly understood due to its heterogeneous and insoluble nature, making it unsuitable for X-ray crystallography and solution NMR studies. Here we use solid-state NMR to investigate the tertiary structure of the *E. faecalis* cell wall. The results not only expand our basic knowledge about bacterial cells, but also provide crucial structural information for understanding how antibiotics inhibit cell-wall biosynthesis.

## 3.2 Materials and Methods

### 3.2.1 Preparation of *E. faecalis* Whole-Cell Samples

*E. faecalis* (ATCC 29212) starter cultures were prepared by inoculating brain-heart infusion (BHI) media with colonies from a brain-heart infusion agar plate. Starter cultures were incubated statically overnight at 37 °C. *E. faecalis* whole-cell samples for NMR were prepared by inoculating sterile enterococcal defined media (EDM) with the overnight starter cultures (0.5% final volume). The components of EDM are listed in Table 3.1. The pH of EDM was adjusted to 7.0 before sterile filtration. Natural-abundance amino acids in EDM were replaced by <sup>13</sup>C and <sup>15</sup>N selectively enriched amino acids (500 mg/L for L-alanine, 200 mg/L for D-alanine, 100 mg/L for L-lysine) to incorporate specific labels into the *E. faecalis* cells. When samples were enriched with isotopically labeled L-alanine or D-alanine, 15 µg/ml of alaphosphin was added to the media every 5 h of growth to inhibit alanine racemase [11] and prevent the interconversion between L-alanine and D-alanine.

Typically the whole cell samples for NMR were grown in 350 ml of EDM at 37 °C with gentle shaking. Cells were harvested at the end of the log phase, which is approximately after 10 h growth with the 660 nm OD around 0.8, by centrifugation at 10,000 g for 10 min at 4 °C. Then the whole-cell pellets were washed two times with 40 mM triethanolamine hydrochloride solution (pH 7.0), centrifuging at 10,000 g for 10 min at 4 °C after each wash. The final whole-cell pellets were resuspended in about 10 ml of 40 mM triethanolamine hydrochloride solution (pH 7.0), instantly frozen in liquid nitrogen, and lyophilized. Typically 150 to 200 mg lyophilized powder was obtained. Then the lyophilized powder of the whole cells were pressed into cylindrical pellets and packed into a zirconium rotor for NMR measurements.

Table 3.1 The components of enterococcal defined media (EDM) on a per liter basis.

$K_2HPO_4 \cdot 3H_2O$	4.3 g	Riboflavin	2 mg	L-Proline	100 mg
$KH_2PO_4$	4.0 g	Inositol	1mg	L-Isoleucine	100 mg
$(NH_4)_2SO_4$	1 g	P-Aminobenzoic Acid	0.05 mg	L-Leucine	100 mg
Boric Acid	0.1 mg	Cyanocobalamin	0.01 mg	L-Valine	100 mg
EDTA	1 mg	$MgSO_4 \cdot 7H_2O$	30 mg	L-Phenylalanine	100 mg
D-Glucose	10 g	$MnSO_4 \cdot H_2O$	10 mg	L-Arginine	100 mg
Adenine	5 mg	$CuSO_4 \cdot 5H_2O$	1 mg	L-Threonine	100 mg
Uracil	5 mg	$ZnSO_4 \cdot 7H_2O$	1 mg	L-Histidine	100 mg
Cytosine	5 mg	NaCl	10 mg	L-Serine	100 mg
Guanine	5 mg	$CaCl_2$	1 mg	L-Methionine	100 mg
Xanthine	5 mg	$NiAc_2 \cdot 4H_2O$	0.1 mg	L-Asparagine	100 mg
Biotin	0.1 mg	$(NH_4)_6Mo_7O_{24} \cdot 4H_2O$	0.2 mg	L-Alanine	100 mg
Thiamine HCl	2 mg	$FeSO_4 \cdot 7H_2O$	10 mg	Glycine	100 mg
Calcium Pantothenate	2 mg	L-Aspartic Acid	100 mg	L-Lysine	100 mg
Pyridoxine HCl	20 mg	L-Cysteine	100 mg	L-Glutamic Acid	100 mg
Folic Acid	0.2 mg	L-Tryptophan	100 mg	L-Glutamine	100 mg
Niacin	2 mg	L-Tyrosine	100 mg		

### 3.2.2 Cell-Wall Isolation

The cell wall was isolated from lyophilized whole cells in a manner similar to that described before [12-14], with some modifications to remove unbroken whole cells and glass-bead debris. The lyophilized whole cells were resuspended in 40 ml cold water with subsequent centrifugation at 3200 g for 30 min at 4 °C. This resuspension and centrifugation cycle was repeated 2 times to remove the triethanolamine hydrochloride in the whole cells. The whole-cell pellet was then resuspended in about 10 ml of water and boiled for 20 min to inactivate the cells prior to centrifugation at 3200 g for 30 min at 4 °C. The whole-cell pellet was resuspended in 25 ml of 25 mM cold potassium phosphate buffer (pH 7.0) with 5 mg of DNase I and transferred to a 60 ml bead beater (Biospec Products, Bartlesville, OK) chamber which was two thirds filled with 0.1 mm diameter glass beads. Cells were beat through 10 cycles of 1 min disruption and 1 min rest. Through the beating process, the bead beater chamber was kept in a bigger chamber containing an ice-water mixture to keep the bead beater chamber cold. After disruption, the homogenate and beads were filtered with a coarse sintered glass funnel to separate the homogenate (filtrate) from the beads by vacuum filtration. The beads were washed further with 100 ml of 10 mM cold EDTA solution (pH 7.0). The filtrate was centrifuged at 25,000 g for 30 min at 4 °C. The crude cell-wall pellet was resuspended in 20 ml of cold water, added dropwise to 100 ml of boiling 4% sodium dodecyl sulfate (SDS), and boiled for 30 min with constant stirring. The mixture was allowed to cool for 2 h with stirring and then maintained unstirred overnight at room temperature. SDS was removed by centrifugation of the mixture at 38,000 g for 1 h at room temperature, followed by three washes using water with centrifugation after each wash. The resulting pellet was resuspended in 60 ml of 10 mM Tris buffer (pH8.2) containing 5 mg of DNase I, 16 mg trypsin, and 16 mg  $\alpha$ -chymotrypsin and incubated at 37 °C with shaking

(150 rpm) for 16 h. This mixture was centrifuged at 38,000 g for 1 h at room temperature and washed two times using water with centrifugation after each wash. The pellet was resuspended in 35 ml of water and centrifuged at 500 g for 5 min to remove any unbroken cells and glass-bead debris. The isolated cell wall was collected by centrifugation at 38,000 g at room temperature for 1 h, resuspended in about 10 ml of 40 mM triethanolamine hydrochloride solution (pH 7.0), instantly frozen in liquid nitrogen, and lyophilized. Typically 40 to 50 mg lyophilized powder was obtained. The lyophilized powder of the cell walls was pressed into cylindrical pellets and packed into a zirconium rotor for NMR measurements.

### 3.2.3 Solid-State NMR Spectrometer and Dante-Select Spin-Diffusion Pulse Sequence

Experiments were performed at 12 Tesla with a six-frequency transmission-line probe having a 12-mm long, 6-mm inner-diameter analytical coil, and a Chemagnetics/Varian ceramic spinning module. Samples were spun using a thin-wall Chemagnetics/Varian (Fort Collins, CO/Palo Alto, CA) 5-mm outer diameter-zirconia rotor at 7143 Hz, with the speed under active control and maintained to within  $\pm 2$  Hz. A Tecmag Libra pulse programmer (Houston, TX) controlled the spectrometer. Two-kW American Microwave Technology (AMT) power amplifiers were used to produce radio-frequency pulses for  $^{13}\text{C}$  (125 MHz) and  $^{15}\text{N}$  (50.7 MHz). The  $^1\text{H}$  (500 MHz) radio-frequency pulses were generated by a 2-kW Creative Electronics tube amplifier driven by 50-W AMT amplifier. All final-stage amplifiers were under active control [15]. The  $\pi$ -pulse lengths were 8  $\mu\text{s}$  for  $^{13}\text{C}$  and  $^1\text{H}$ , and 9  $\mu\text{s}$  for  $^{15}\text{N}$ . Proton-carbon-matched cross-polarization transfers were made in 2 ms at 56 kHz. Proton dipolar decoupling was 100 kHz during data acquisition. The S and S<sub>0</sub> alternate-scan strategy compensated for short-term drifts in Dante-select spin-diffusion and REDOR experiments. Standard XY-8 phase cycling [16] was used to compensate for pulse imperfections [17, 18] for all refocusing observe-channel  $\pi$  pulses (inserted at the end of each rotor period during dipolar evolution) and dephasing  $\pi$  pulses (inserted in the middle of each rotor period). Frequency-specific  $^{13}\text{C}$  chemical shifts were selected (Figure 3.3) prior to  $^{13}\text{C}\{^{15}\text{N}\}$  REDOR dipolar evolution using rotor-asynchronous Dante irradiation, z-axis storage, and mixing times of 200 ms with no  $^1\text{H}$  decoupling [19, 20]. Typically, CPMAS spectra from 100-mg whole-cell and 50-mg cell-wall samples were the result of the accumulation of 20,000 to 40,000 scans at room temperature. The combined Dante-select-REDOR experiments involved the accumulation of 160,000 scans for each spectrum.

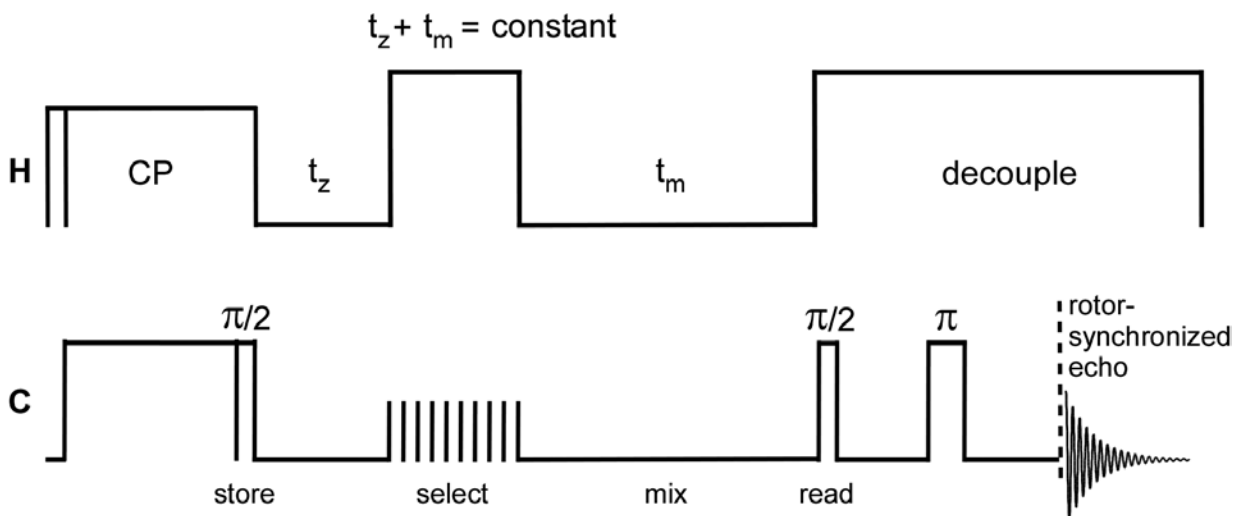


Figure 3.3 Pulse sequence for determination of  $^{13}\text{C}$ - $^{13}\text{C}$  proximities by spin diffusion. Carbon magnetization from a matched Hartmann-Hahn cross-polarization transfer is stored along the static magnetic field. The time  $t_z$  allows transients to disperse. A Dante frequency selection is made by 64 1- $\mu\text{s}$  pulses (40- $\mu\text{s}$  separation) with proton decoupling so that carbon frequencies are well defined. Spin diffusion occurs during  $t_m$  (with no proton irradiation) and cross peaks are read out by a Hahn echo. This is a constant-time experiment ( $t_z + t_m$  is fixed) so that signal intensities for different mixing times can be compared directly with no correction for  $^{13}\text{C}$  spin-lattice relaxation. Proximity of  $^{15}\text{N}$  to either or both of the carbons of a  $^{13}\text{C}$ - $^{13}\text{C}$  pair connected by spin diffusion is determined by adding a C{N} REDOR dipolar evolution period after  $t_m$  and before the read pulse.

## 3.3 Results and Discussion

### 3.3.1 *E. faecalis* Growth with Alaphosphin

In Gram-positive bacteria, alanine racemase interconverts L-alanine and D-alanine [21]. L-alanine is effectively produced through the biosynthesis pathway of the bacteria, and D-alanine is produced by converting L-alanine to D-alanine through alanine racemase [21]. D-alanine is an essential building block for bacterial peptidoglycan and teichoic acids. The NMR samples required incorporation of  $^{13}\text{C}$  or  $^{15}\text{N}$  selectively-labeled L-alanine and D-alanine. Thus, the inhibition of alanine racemase is crucial to prevent scrambling of isotopic labels. To accomplish this goal, alaphosphin was used to inhibit alanine racemase [11]. Under the presence of alaphosphin, *E. faecalis* cells have little growth since D-alanine can not be produced (Figure 3.4, top and bottom, purple curves). To resume the growth, 100 mg/L and 200 mg/L of D-alanine were externally added to the media with alaphosphin. The cell growth was partially resumed with 100 mg/L D-alanine, and almost completely resumed with 200 mg/L D-alanine (Figure 3.4, top, red and blue curves). Further increasing the D-alanine concentration from 200 mg/L to 300 mg/L did not significantly affect the growth (Figure 3.4, bottom, red and blue curves). Thus, for the NMR sample preparation, 200 mg/L D-alanine was added to EDM with alaphosphin present to prevent the scrambling of isotopic labels while maintaining regular cell growth. Two *E. faecalis* whole-cell and two cell-wall samples for NMR were prepared. The isotopic labeling strategy is detailed in Table 3.2.

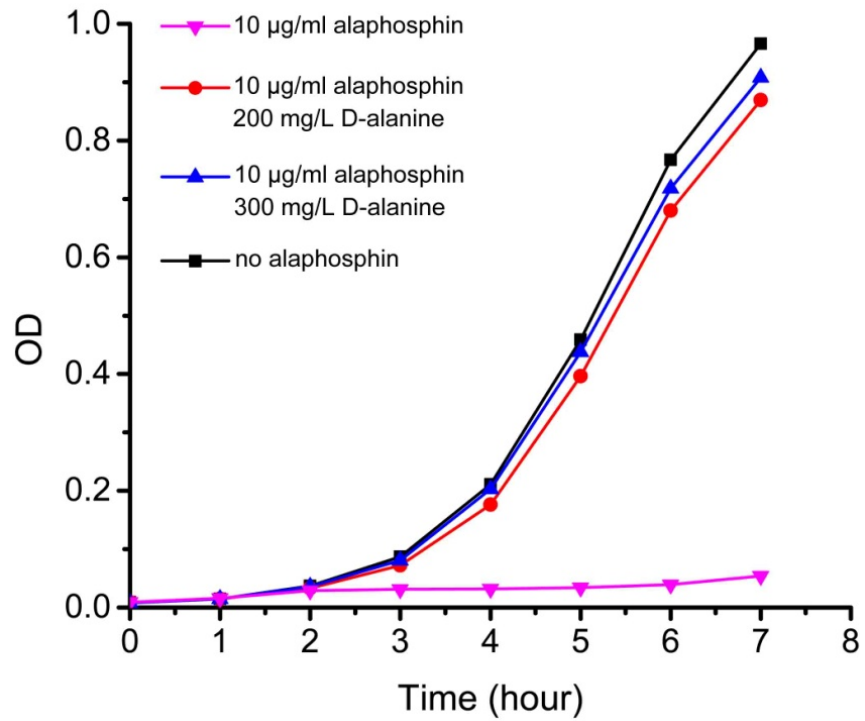
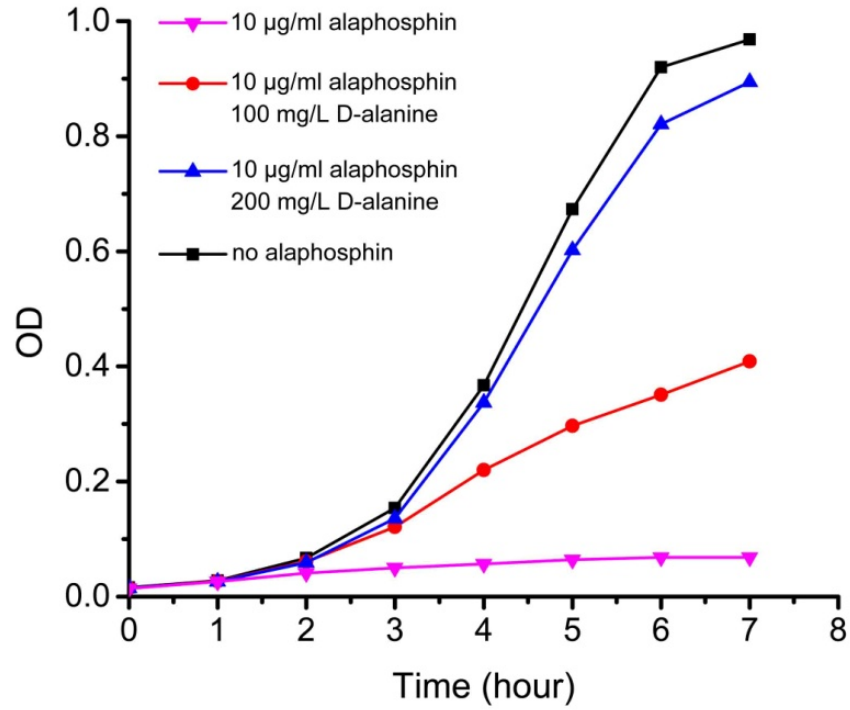


Figure 3.4 *E. faecalis* growth curves in 100 ml of EDM with 10 µg/ml alaphosphin at different concentrations of D-alanine.

Table 3.2 *E. faecalis* labeling strategy. (Left to right: sample number, sample labeling, state of NMR sample, and characterization target.)

1	L-[ $\epsilon$ - $^{15}\text{N}$ ]lysine	cell walls	stems without bridges
2	L-[1- $^{13}\text{C}$ ]lysine and D-[ $^{15}\text{N}$ ]alanine	whole cells	D-alanylation of wall teichoic acid, tripeptide-stem concentration, and D-[ $^{15}\text{N}$ ]alanine isotopic enrichment
3	D-[1- $^{13}\text{C}$ ]alanine and L-[ $^{15}\text{N}$ ]alanine	cell walls	cross-linking and L-[ $^{15}\text{N}$ ]alanine isotopic enrichment
4	L-[1- $^{13}\text{C}$ ]alanine, D-[3- $^{13}\text{C}$ ]alanine and L-[ $\epsilon$ - $^{15}\text{N}$ ]lysine	whole cells	cross-links, bridge links, L-[1- $^{13}\text{C}$ ]alanine isotopic enrichment, and peptidoglycan architecture

When the NMR samples were prepared, two shots of 15  $\mu\text{g/ml}$  (final concentration in EDM) alaphosphin were added at the beginning and at the 5th hour of growth, respectively, to inhibit completely alanine racemase (Figure 3.5). When alaphosphin is added to the media, it does not function instantaneously. Instead, there are three steps: (1) active transport of alaphosphin into bacterial cells by peptide permeases; (2) cleavage of alaphosphin by intracellular aminopeptidases to yield L-1-aminoethylphosphonic acid; (3) inhibition of L-1-aminoethylphosphonic acid on alanine racemase [11]. A small amount of growth after adding alaphosphin was observed in the first two hours before the curve flattens (Figure 3.5, blue curve), attributed to the fact that alaphosphin takes time to function. Thus the isotopically-labeled D-alanine and L-alanine were added at the second hour of growth instead of the beginning (Figure 3.5, red curve) to completely prevent scrambling of isotopic labels. Accordingly, the growth resumption was delayed for two hours (Figure 3.5, red curve). The *E. faecalis* L-alanine biosynthesis is very active; thus 500 mg/L of isotopically labeled L-alanine was used to increase the isotopic enrichment in cells. Cells were harvested at the end of the log phase, which is approximately after 10 h growth with 660 nm OD around 0.8 (Figure 3.5, red curve).

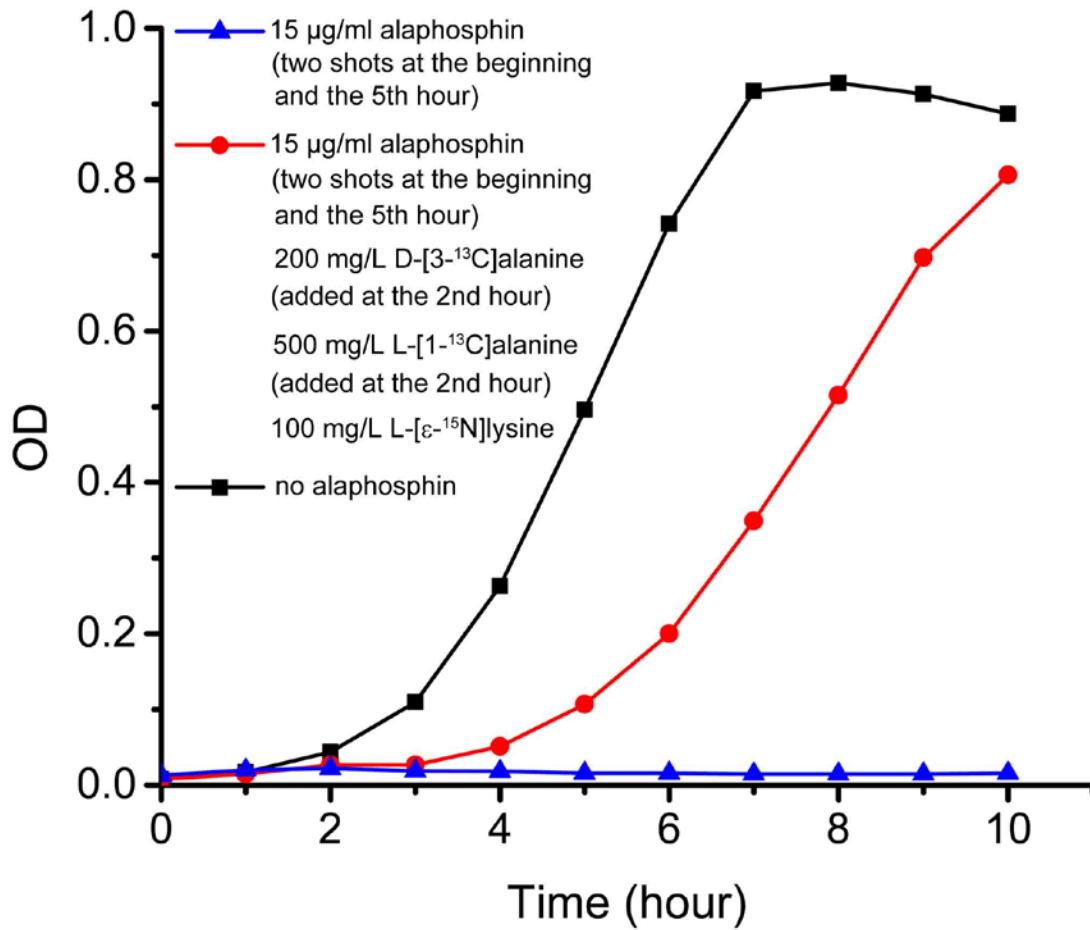


Figure 3.5 Growth curves for *E. faecalis* with alaphosphin (blue curve), sample #4 (red curve) with alaphosphin and selectively isotopical labeled D-alanine, L-alanine, and L-lysine as shown in the figure, and *E. faecalis* without alaphosphin (black curve),. The black and blue curves are growth in 100 ml of EDM. The red curve is growth in 350 ml of EDM.

### 3.3.2 Solid-State NMR Characterization of *E. faecalis* PG Tertiary Structure

*Open and Closed Peptidoglycan Lysyl Sidechains.* With increasing contact time, the matched Hartmann-Hahn cross-polarization  $^{15}\text{N}$  NMR amide-nitrogen intensities (95 ppm) decrease while the amine-nitrogen intensities (10 ppm) increase (Figure 3.6) for isolated cell walls of *E. faecalis* labeled by L- $[\epsilon\text{-}^{15}\text{N}]$ lysine (sample #1). This indicates a proton rotating-frame lifetime,  $T_{1\rho}(\text{H})$ , longer than the proton-amide nitrogen transfer time and shorter than the proton-amine nitrogen transfer time [22]. Because both types of nitrogens have directly attached protons, the difference in transfer rates is due to local dynamics [22]. This is consistent with a relatively rigid lysyl sidechain that is part of a bridge-link and a flexible lysyl sidechain for an open sidechain (see Figure 3.2). If the terminal amine is protonated,  $\text{C}_3$  rotation for a  $\text{-NH}_3^+$  is also possible [23]. The cross-polarization dynamics can be described by coupled ordinary differential equations [22] which leads to an estimate of 10% open bridges for *E. faecalis* grown as described in the Methods section. Open-bridge concentrations between 0 and 15% have been observed for the peptidoglycan of *Staphylococcus aureus* [14], with the lower concentrations observed for cells harvested during the early stages of exponential growth, and the higher concentrations for cells harvested during stationary-phase growth.

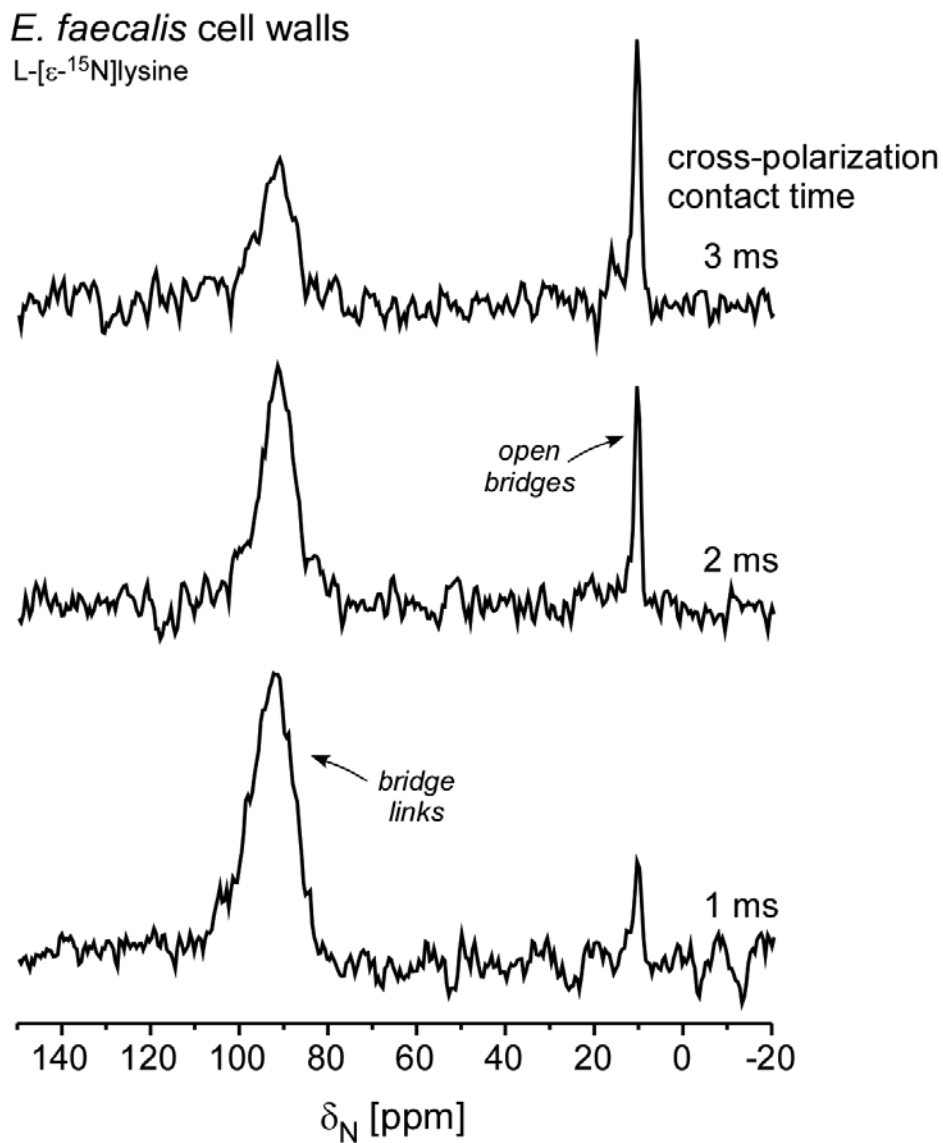


Figure 3.6 CPMAS  $^{15}\text{N}$  NMR spectra of isolated cell walls of *E. faecalis* labeled by L-[ $\epsilon$ - $^{15}\text{N}$ ]lysine (sample #1) as a function of the proton-nitrogen contact time. The chemical-shift scale is referenced to solid ammonium sulfate (whose nitrogen resonance appears at 20 ppm relative to external liquid ammonia).

*Wall Teichoic Acid.* The main repeating unit for *E. faecalis* of wall teichoic acid (Figure 3.2 top) is heavy in sugars and relatively light in sites for D-alanylation to modulate cell-surface charge [24]. Whole cells of *E. faecalis* labeled by L-[1-<sup>13</sup>C]lysine and D-[<sup>15</sup>N]alanine (sample #2) have a CPMAS <sup>15</sup>N NMR spectrum with an amide-peak intensity (after ethanol extraction) that is ten times that of the amine-peak intensity (Figure 3.7). The former is due to D-alanine in cell walls and the latter in wall teichoic acid (Figure 3.2). The minor change in relative intensities induced by the extraction is attributed to a reduction in flexibility of the wall teichoic acid resulting in a decrease in the proton-amine nitrogen transfer time.

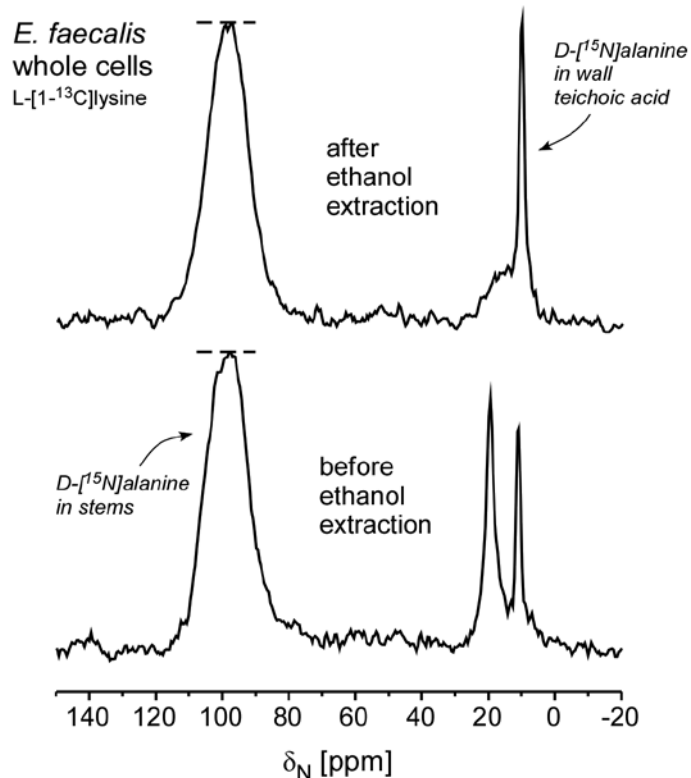


Figure 3.7 CPMAS <sup>15</sup>N NMR spectra of whole cells of *E. faecalis* labeled by L-[1-<sup>13</sup>C]lysine and D-[<sup>15</sup>N]alanine (sample #2) before (bottom) and after (top) extraction by ethanol to remove low molecular-weight metabolites. The spectra have been scaled for equal-intensity amide-nitrogen peaks near 100 ppm (dotted lines).

*Tripeptide Stems. Isotopic Enrichments of L-[1-<sup>13</sup>C]Alanine and D-[<sup>15</sup>N]Alanine.* The N{C} REDOR <sup>15</sup>N NMR spectrum after 16 rotor periods of dipolar evolution of whole cells labeled by L-[1-<sup>13</sup>C]alanine, D-[3-<sup>13</sup>C]alanine, and L-[ε-<sup>15</sup>N]lysine (sample #4) has a ΔS/S<sub>0</sub> of 0.6 (Figure 3.8). This is a direct measure of the 60% isotopic enrichment of L-[1-<sup>13</sup>C]alanine and the extent of *de novo* synthesis of alanine even in the presence of high concentrations of exogenous L-alanine in the media (see Methods and Section 3.3.1). The REDOR full-echo spectrum has an amine-nitrogen peak height that is four times that of the amide-nitrogen peak and a linewidth which is half that of the amide peak (Figure 3.8, bottom). This translates into an integrated intensity ratio of 2:1 for lysines in cytoplasmic protein relative to lysines in cell-wall stems.

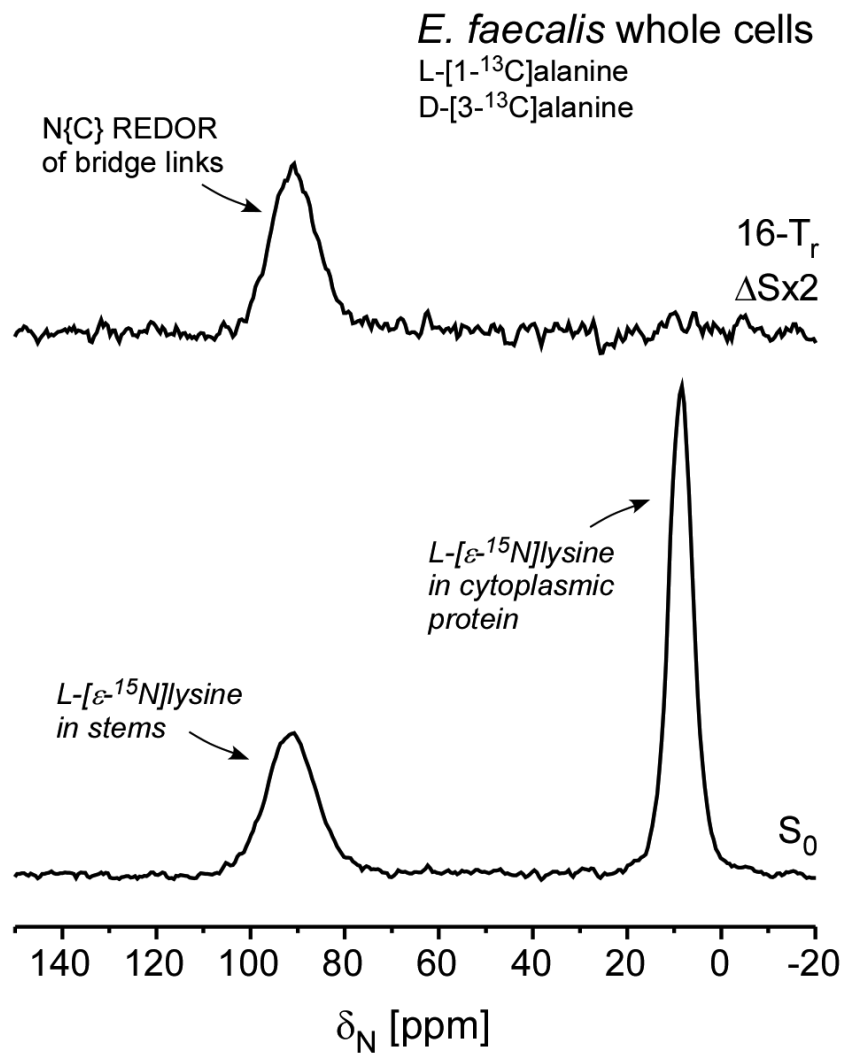


Figure 3.8  $N\{C\}$  REDOR  $^{15}N$  NMR spectra of whole cells of *E. faecalis* labeled by L-[1- $^{13}C$ ]alanine, D-[3- $^{13}C$ ]alanine, and L-[ $\epsilon$ - $^{15}N$ ]lysine (sample #4). The full-echo spectrum ( $S_0$ ) is at the bottom of the figure and the REDOR difference ( $\Delta S$ ) after 16 rotor periods of dipolar evolution is at the top. The ratio of labeled lysine incorporated in cytoplasmic proteins to that incorporated in cell walls is 2:1.

The C{N} REDOR  $^{13}\text{C}$  NMR spectra of sample #2 shows a  $\Delta\text{S}$  with a chemical shift of 174 ppm while that of  $\text{S}_0$  is 175 ppm (Figure 3.9). This occurs because the direct-bond REDOR difference arises from peptide stems that are four or five units long, whereas  $\text{S}_0$  has contributions from these peptide bonds but also from the carboxyl carbons of terminal lysyl units in tripeptide stems. These short stems result from the D,D-carboxypeptidase that is active in enterococci [25]. The carboxyl-carbon chemical shift is typically near 178 ppm [25]. An estimate can be made of the concentration of tripeptide stems by assuming that the  $\Delta\text{S}$  lineshape is representative of all peptide residues in cell walls and cytoplasmic proteins, and then scaling  $\Delta\text{S}$  so that subtraction from  $\text{S}_0$  has zero intensity at 174 ppm (Figure 3.9 top). The surviving difference signal is attributed to lysyl label in tripeptide stems. The total peptide intensity is then deconvoluted into cytoplasmic and cell-wall contributions (2:1) to be consistent with the experimentally determined ratio in Figure 3.8 (bottom). These contributions are shown in blue in Figure 3.9. The ratio of the C{N}  $\Delta\text{S}$  to the cell-wall contribution determines the isotopic enrichment of D- $^{15}\text{N}$ alanine (which appears only in cell walls) as 50%. The ratio of the tripeptide integrated intensity to that of the cell-wall contribution is also 50% which establishes the activity of the D,D-carboxypeptidase.

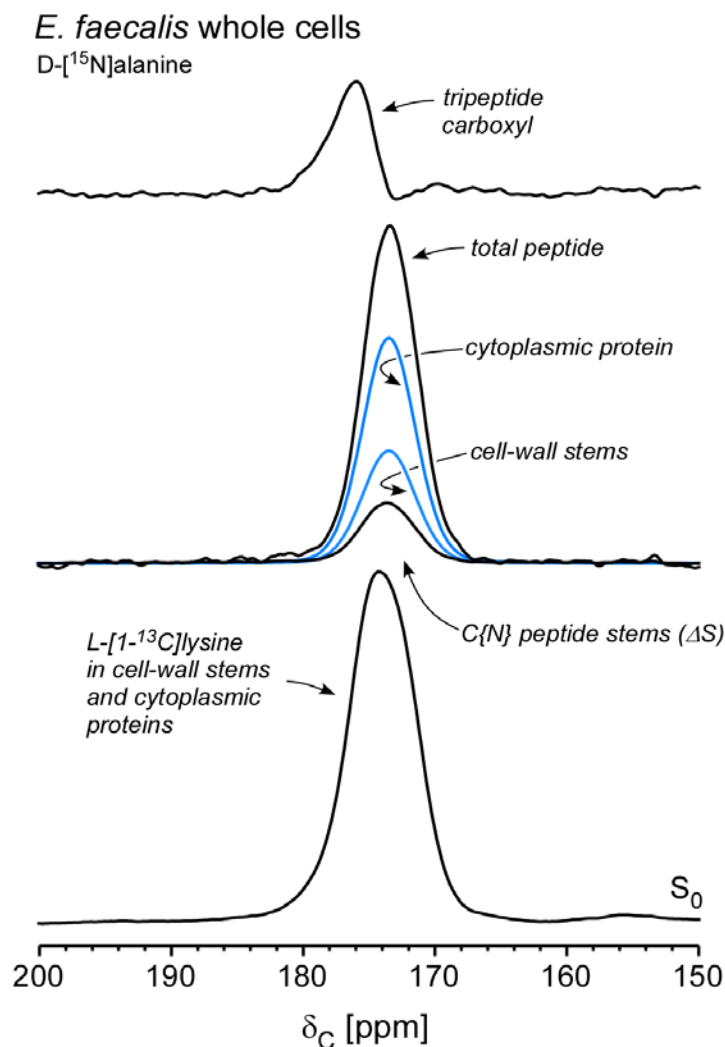


Figure 3.9 C{N} REDOR  $^{13}\text{C}$  NMR spectra of whole cells of *E. faecalis* labeled by L-[1- $^{13}\text{C}$ ]lysine and D-[ $^{15}\text{N}$ ]alanine (sample #2). The full-echo spectrum ( $S_0$ ) is at the bottom of the figure and the REDOR difference ( $\Delta S$ ) after 16 rotor periods of dipolar evolution is second from the bottom. The chemical-shift scale has been referenced to external tetramethylsilane. Total peptide (second from the top) was estimated by 5.85 times  $\Delta S$ , a factor which left zero intensity at 174 ppm after the subtraction,  $S_0 - 5.85\Delta S$ . The difference peak at 178 ppm is assigned to terminal lysine carboxyl carbons in uncross-linked tri-peptide stems. The total peptide is separated into cytoplasmic and cell-wall contributions (blue peaks) having the 2:1 ratio of Figure 3.8. The ratio of  $\Delta S$  to the blue cell-wall stem peak determines the isotopic enrichment of D-[ $^{15}\text{N}$ ]alanine as approximately 50%.

*Cross-Linking.* The N{C} REDOR  $^{15}\text{N}$  NMR spectra of isolated cell walls of *E. faecalis* labeled by D-[1- $^{13}\text{C}$ ] and L-[ $^{15}\text{N}$ ]alanine (sample #3) after 16 rotor periods of dipolar evolution has a  $\Delta\text{S}/\text{S}_0$  ratio of 0.15 (Figure 3.10). Because there are three L-alanines (two in the bridge and one in the stem) contributing to  $\text{S}_0$  for every L-alanine in a L-alanine-D-alanine cross-link, a  $\Delta\text{S}/\text{S}_0$  ratio of 0.15 means cross-linking of 45%. The *E. faecalis* peptidoglycan therefore has 45% cross-linked tetrapeptide stems, 50% uncross-linked tripeptide stems (see above), and 5% uncross-linked tetra- and/or pentapeptide stems. The latter would be sufficient to make this strain vancomycin susceptible [25].

*Isotopic Enrichment of L-[ $^{15}\text{N}$ ]Alanine.* The C{N}  $\text{S}_0$  is composed of three components (Figure 3.11, left black): carbonyl carbons in a peptide bond (175 ppm) predominantly in cross-linked D-alanine, ester carbonyl carbons (172 ppm) in wall teichoic acids, and carboxyl carbons (178 ppm) in uncross-linked D-alanine. The C{N}  $\Delta\text{S}$  after 16 rotor periods of dipolar evolution represents the carbonyl carbon directly bond to an  $^{14}\text{N}$  in a peptide bond (Figure 3.11, left red). If the observed C{N}  $\Delta\text{S}$  is scaled by a factor of 1.9 (Figure 3.11, right red) to account for all the carbonyl carbons in a peptide bond, the residual ester carbonyl carbons (Figure 3.11, right blue, 172 ppm) are consistent with the determination of D-alanine in wall teichoic acid shown in Figure 3.7, and with the 5% concentration of D-alanyl termini in uncross-linked stems (Figure 3.11, right blue, 178 ppm) described in the previous paragraph. The scale factor establishes the isotopic enrichment of L-[ $^{15}\text{N}$ ]alanine as 53% ( $1/1.9 \approx 0.53$ ).

*E. faecalis* cell walls  
D-[1-<sup>13</sup>C]alanine

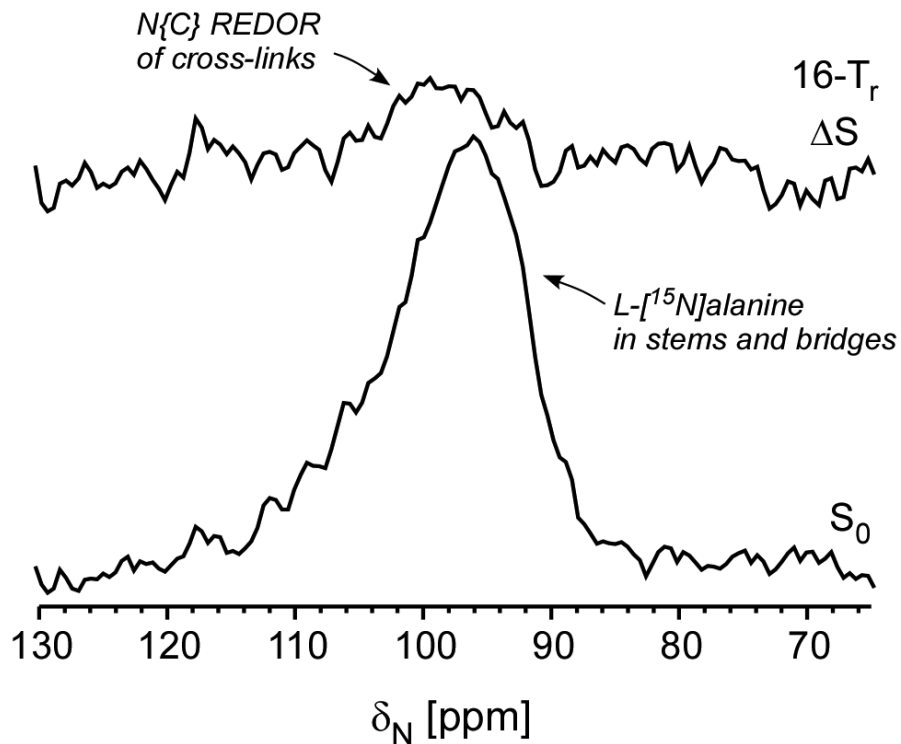


Figure 3.10 N{C} REDOR <sup>15</sup>N NMR spectra of cell walls of *E. faecalis* labeled by D-[1-<sup>13</sup>C]alanine and L-[<sup>15</sup>N] alanine (sample #3). The full-echo spectrum ( $S_0$ ) is at the bottom of the figure and the REDOR difference ( $\Delta S$ ) after 16 rotor periods of dipolar evolution is at the top. The <sup>13</sup>C alanine isotopic enrichment is 99% (full) because of alanine racemase inhibition during cell growth (see Methods and Section 3.3.1). The  $\Delta S/S_0$  ratio of 15-20% translates into approximately 50% cell-wall cross-linking, after taking into account the three L-alanyl contributions to  $S_0$  (stem and bridge, Figure 3.2) for each D-alanyl-L-alanyl cross-link  $\Delta S$ .

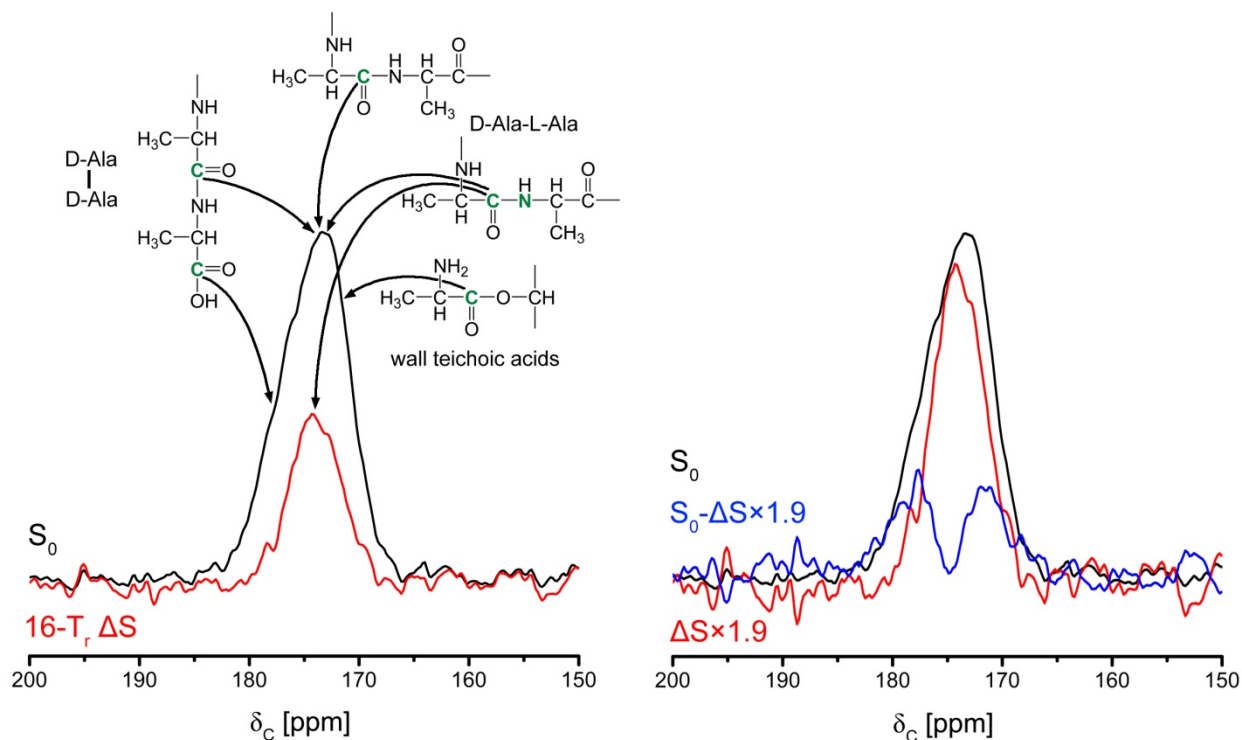


Figure 3.11  $C\{N\}$  REDOR  $^{13}\text{C}$  NMR spectra of cell walls of *E. faecalis* labeled by D-[1- $^{13}\text{C}$ ]alanine and L-[ $^{15}\text{N}$ ]alanine (sample #3). The isotopically-labeled carbon and nitrogen are in green (left). The full-echo spectrum ( $S_0$ ) are in black and the REDOR difference ( $\Delta S$ ) after 16 rotor periods of dipolar evolution is in red (left). The REDOR difference spectrum is scaled ( $\Delta S \times 1.9$ , right red) and subtracted from the  $S_0$  spectrum (right blue). The scale factor for the  $\Delta S$  spectrum was chosen to account for all the carbonyl carbons in a peptide bond (right red) and leaves no intensity at 175 ppm after subtraction from  $S_0$  (right blue). The residual ester carbonyl carbons at 172 ppm (right blue) match the ratio of D-alanyl label in wall teichoic acid and peptidoglycan stems of Figure 3.7. The concentration of uncross-linked stems (right blue, 178 ppm) is about 10% of that of cross-linked stems (right red). The isotopic enrichment of L-[ $^{15}\text{N}$ ]alanine is therefore 53% (1/1.9).

*Peptidoglycan Architecture.* The strategy to determine the peptidoglycan architecture of *E. faecalis* is detection of connectivities between stems and bridges removed from the cross-link sites. Carbon-carbon spin diffusion has a range of only 3-4 Å for mixing times of 200 ms if there is no proton irradiation [26]. Dante carbon-frequency selection at 18 ppm of whole cells labeled by L-[1-<sup>13</sup>C]alanine, D-[3-<sup>13</sup>C]alanine, and L-[ε-<sup>15</sup>N]lysine (sample #4), with and without C{N} REDOR dephasing for 8 rotor periods (see caption to Figure 3.3), results in minor cross-peaks for the buffer and cell-wall sugars (Figure 3.12). These can be attributed to natural-abundance <sup>13</sup>C and will be ignored. A more substantial ΔS/S<sub>0</sub> at 155 ppm is due to single-carbon label insertions in purines resulting from the activity of D-alanylmethyltransferase [27]. This is important for metabolism but incidental to the architecture determination and will also be ignored.

The peak at 176 ppm with a weaker shoulder at 172 ppm (top insets) are together about 15% of half the D-[3-<sup>13</sup>C]alanyl inversion (only half is due to an excess over the Boltzmann population), and therefore arise from the L-[1-<sup>13</sup>C]alanine label. Neither the peak nor its shoulder has a significant coupling to the bridge <sup>15</sup>N label (Figure 3.12, insets, dotted lines). The 176-ppm peak shows a coupling, however, when the C{N} dipolar evolution is increased to 128 rotor periods (Figure 3.13, insets, dotted lines). In addition, the Dante-selected methyl-carbon peak also shows significant C{N} REDOR dephasing (Figure 3.13, top, dotted lines; Figure 3.14).

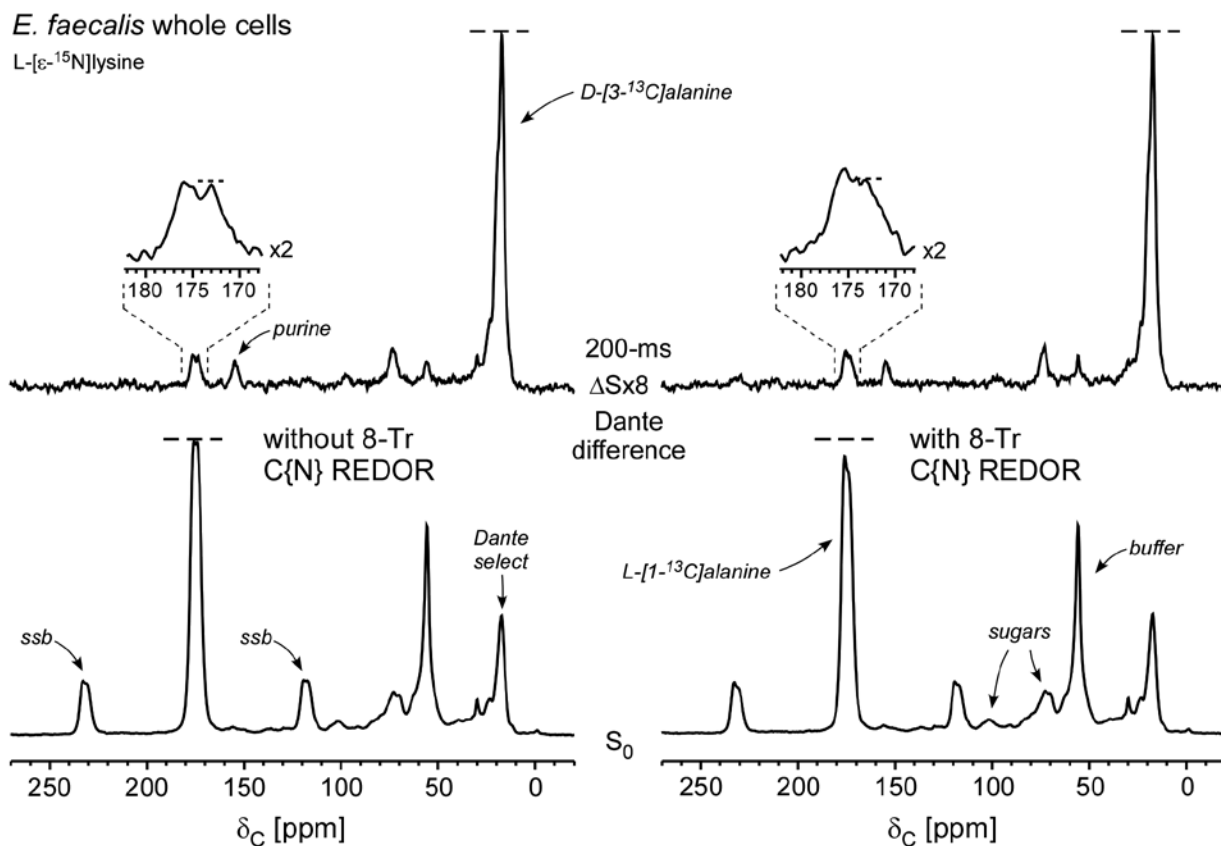


Figure 3.12 Dante difference  $^{13}\text{C}$  NMR spectra of whole cells of *E. faecalis* labeled by L-[1- $^{13}\text{C}$ ]alanine, D-[3- $^{13}\text{C}$ ]alanine, and L-[ $\epsilon$ - $^{15}\text{N}$ ]lysine (sample #4) with (right) and without (left) 8 rotor periods of C{N} dipolar evolution following  $^{13}\text{C}$ - $^{13}\text{C}$  spin diffusion. The full-echo spectrum ( $S_0$ ) is at the bottom of the figure and the Dante difference, after selection at the center of the D-[3- $^{13}\text{C}$ ]alanyl methyl-carbon peak (Figure 3.3), is at the top of the figure. The methyl-carbon label is connected by spin diffusion to the buffer, sugars, a purine carbon at 155 ppm (see text), and various L-[1- $^{13}\text{C}$ ]alanyl carbons (172-176 ppm). Right-to-left comparisons (dotted lines) reveal the extent of REDOR dephasing of selected peaks, which is significant only for the  $^{13}\text{C}$ - $^{15}\text{N}$  bridge-link direct bond (see Figure 3.2).

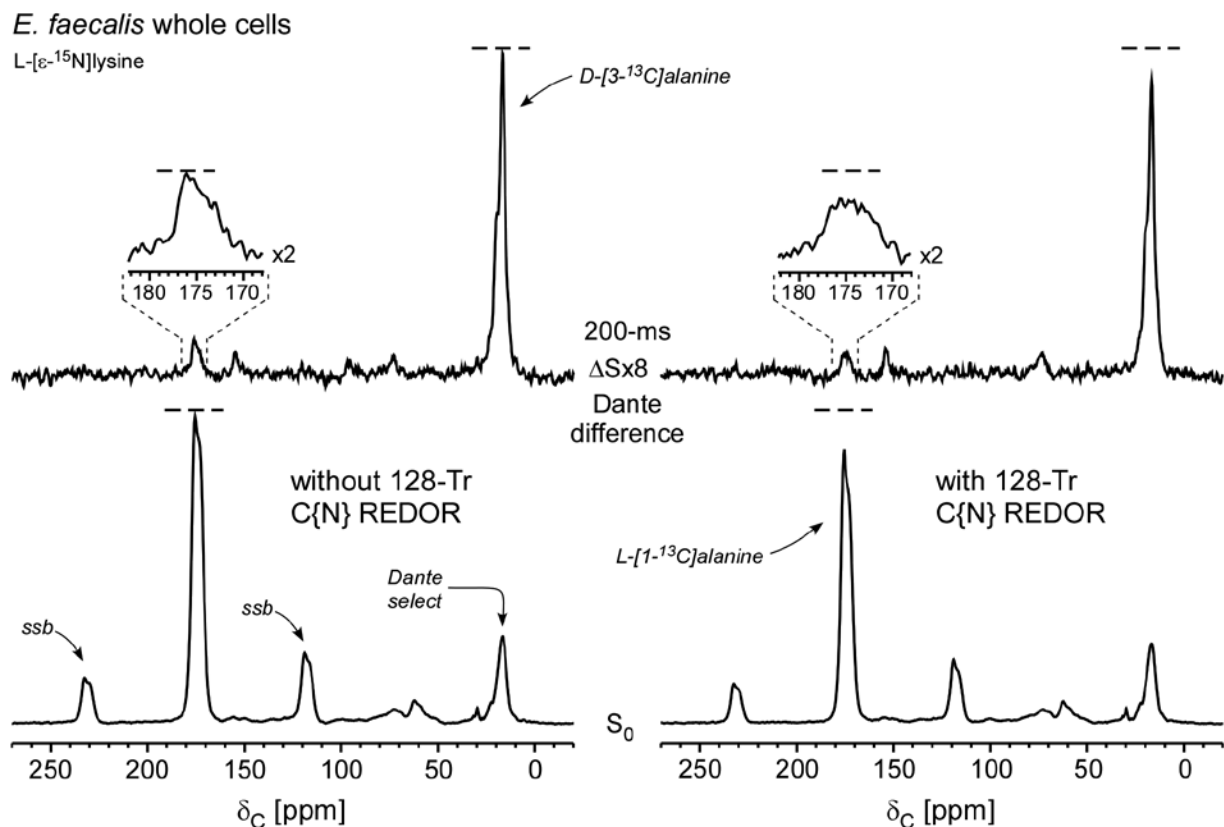


Figure 3.13 Dante difference  $^{13}\text{C}$  NMR spectra of whole cells of *E. faecalis* labeled by L-[ $1$ - $^{13}\text{C}$ ]alanine, D-[ $3$ - $^{13}\text{C}$ ]alanine, and L-[ $\epsilon$ - $^{15}\text{N}$ ]lysine (sample #4) with (right) and without (left) 128 rotor periods of  $\text{C}\{\text{N}\}$  dipolar evolution following  $^{13}\text{C}$ - $^{13}\text{C}$  spin diffusion. The full-echo spectrum ( $S_0$ ) is at the bottom of the figure and the Dante difference, after selection at the center of the D-[ $3$ - $^{13}\text{C}$ ]alanyl methyl-carbon peak, is at the top. Carbon-carbon connectivities are similar to those of Figure 3.12 but attenuated by the echo decay of the longer dipolar evolution. Right-to-left comparisons (dotted lines) show significant REDOR dephasing at 176 ppm (insets) and 18 ppm, in addition to that for the bridge-link direct bond.

*E. faecalis* whole cells

L-[ $\epsilon$ - $^{15}\text{N}$ ]lysine

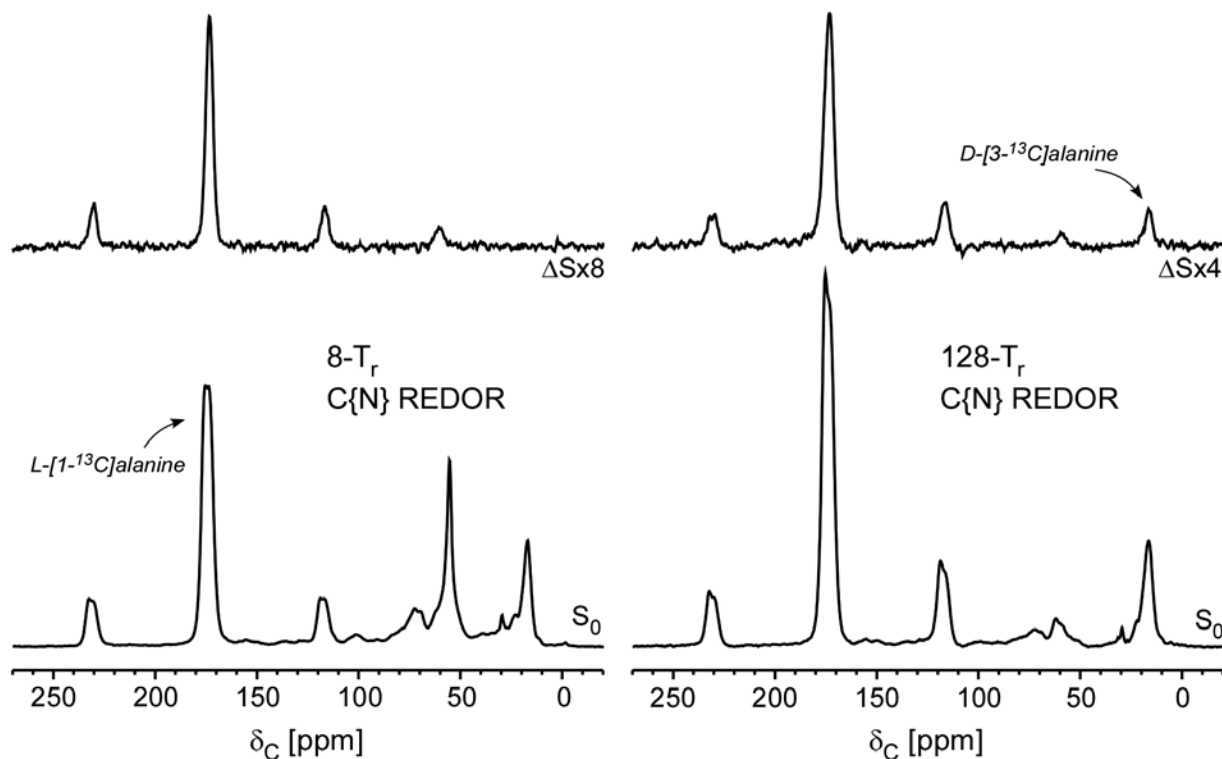


Figure 3.14 C{N} REDOR  $^{13}\text{C}$  NMR spectra of whole cells of *E. faecalis* labeled by L-[1- $^{13}\text{C}$ ]alanine, D-[3- $^{13}\text{C}$ ]alanine, and L-[ $\epsilon$ - $^{15}\text{N}$ ]lysine (sample #4) after (left) 8 and (right) 128 rotor periods of  $^{13}\text{C}$ - $^{15}\text{N}$  dipolar evolution. The full-echo spectra ( $S_0$ ) are at the bottom of the figure and the REDOR differences ( $\Delta S$ ) at the top (8  $T_r$ , left,  $\times 8$ ; 128  $T_r$ , right,  $\times 4$ ). The REDOR differences were obtained from the differences of the  $S_0$  spectra of Figures 9 (8  $T_r$ ) and 10 (128  $T_r$ ).

The L-[1-<sup>13</sup>C]alanyl coupling to the lysyl  $\epsilon$ -<sup>15</sup>N can be examined in more detail by using double differences. If the the 8-T<sub>r</sub>  $\Delta$ S is subtracted from the 128-T<sub>r</sub>  $\Delta$ S, then contributions to the latter from the carbonyl carbon proximal to the  $\epsilon$ -<sup>15</sup>N are largely removed (Figure 3.15, second from bottom). They are completely removed if the 32-T<sub>r</sub>  $\Delta$ S is subtracted (Figure 3.15, second from the top). Two equal-intensity peaks are now resolved, one at 176 ppm, and the other at 172 ppm. Both arise from the L-alanyl carbonyl carbon distal to the  $\epsilon$ -<sup>15</sup>N label. Based on chemical shifts [28], the 172-ppm is assigned to uncross-linked L-alanines with a terminal -NH<sub>2</sub> or -NH<sub>3</sub><sup>+</sup> moiety, while the 176-ppm peak is assigned to cross-linked L-alanines. The cross-linked peptide carbonyl carbon is about the same distance to the lysyl  $\epsilon$ -<sup>15</sup>N as is the uncross-linked L-alanine carbonyl carbon, evidenced by the equal intensity peaks in Figure 3.15 (second from top), but is closer to the D-[3-<sup>13</sup>C] alanyl label (comparison of top two spectra of Figure 3.15).

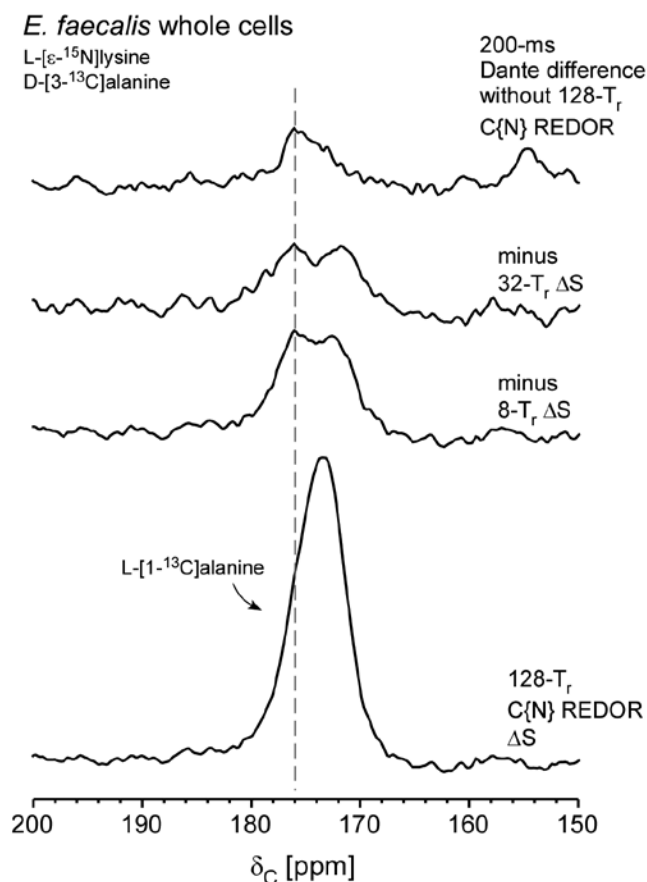


Figure 3.15 Double-difference C{N} REDOR  $^{13}\text{C}$  NMR spectra of whole cells of *E. faecalis* labeled by L-[1- $^{13}\text{C}$ ]alanine, D-[3- $^{13}\text{C}$ ]alanine, and L-[ $\epsilon$ - $^{15}\text{N}$ ]lysine (sample #4). The REDOR difference after 128 rotor periods of  $^{13}\text{C}$ - $^{15}\text{N}$  dipolar evolution (Figure 3.14, top right) is shown at the bottom of the figure (150-200 ppm only). This difference, after subtracting the REDOR  $\Delta\text{S}$ 's after 8 and 32 rotor periods of dipolar evolution, respectively, generates double differences, shown second and third from the bottom. The double differences are compared to the Dante difference of Figure 10 (top left, inset), shown at the top of the figure. The double-difference spectra have the contributions from the L-alanyl bridge label proximal to the bridge-link  $^{15}\text{N}$  removed (see Figure 3.2). The two double-difference L-alanyl peaks distal to the bridge-link  $^{15}\text{N}$  are assigned to cross-linked (176 ppm) and uncross-linked (172 ppm) bridges (see text). These two peaks are approximately equal in intensity indicating 50% cross-linking. The cross-linked distal L-alanyl moiety is closer in space to a D-[3- $^{13}\text{C}$ ]alanyl label (dotted line).

### 3.4 Conclusion

The connectivities of the two L-alanyl carbonyl carbons to D-[3-<sup>13</sup>C] and ε-<sup>15</sup>N labels are sufficient to establish peptidoglycan architecture. Inspection of the structural formula of Figure 3.2 would make it appear that neither L-alanyl bridge carbonyl carbon is close to the methyl label. However, the drawing of Figure 3.2 has cross-linked stems parallel whereas a short-bridge peptidoglycan probably has cross-linked stems perpendicular to one another as illustrated in Figure 3.16. This architecture was established for the short-bridge peptidoglycan of the FemA mutant of *Staphylococcus aureus* [29]. Cross-linked parallel stems were ruled out for FemA by the many severe steric clashes [29].

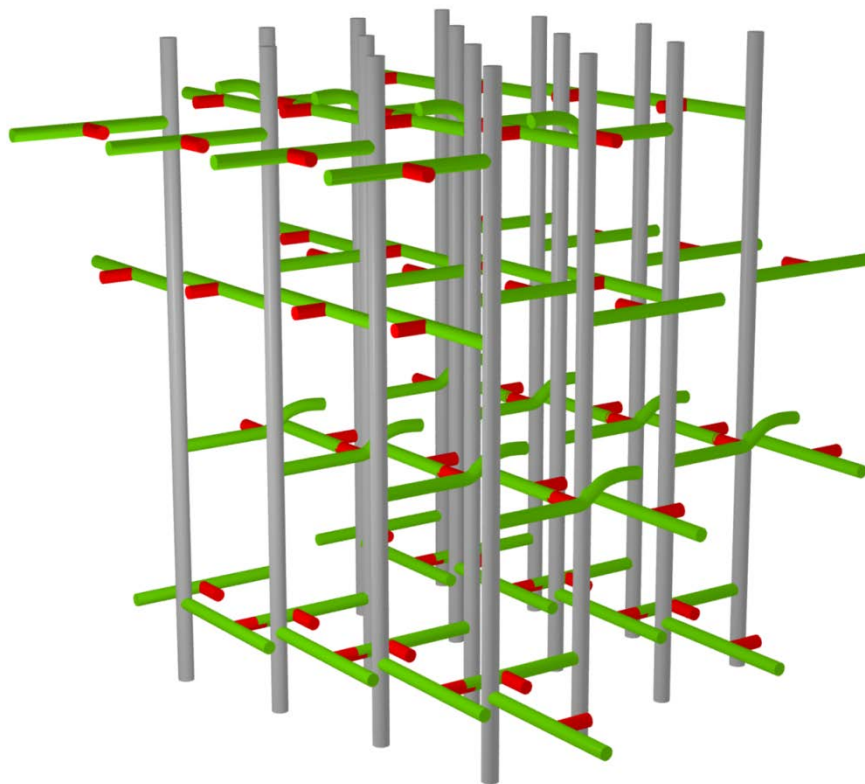


Figure 3.16 Three-dimensional representation of the hybrid model for a short-bridge peptidoglycan lattice [29]. Glycan chains are in gray, peptide stems in green, and the bridges in red.

The cross-link bond of *E. faecalis* is therefore not necessarily co-linear to the bridge-link bond (Figure 3.17, top), as shown in Figure 3.2. A geometry is possible that swings the methyl- $^{13}\text{C}$  label of the D-alanyl cross-link toward the bridge and shortens the distance to the cross-linked L-alanyl carbonyl carbon (distal to the lysyl  $\epsilon$ - $^{15}\text{N}$ ) to much less than the distance of five extended covalent bonds (Figure 3.17 bottom inset). The observed 15% dephasing (Figure 3.13 top insets) after  $128 T_r$  of dipolar evolution indicates a C-N distance of  $5.5 \text{ \AA}$  [30-32]. The D-[ $3\text{-}^{13}\text{C}$ ]alanyl label is also brought within dephasing range of the lysyl  $^{15}\text{N}$  (Figure 3.14, top right) with a  $\Delta S/S_0$  of 7% for a C-N distance of  $5.8 \text{ \AA}$  [30-32].

The uncross-linked distal L-alanyl carbonyl carbon is about the same distance to the  $\epsilon$ - $^{15}\text{N}$  label, but is farther away from the D-[ $3\text{-}^{13}\text{C}$ ]alanyl label (Figure 3.15, top two spectra). The first result is consistent with the geometry of a single stem and its attached bridge. The second result is consistent with the removal of most D-alanyl units from uncross-linked stems (Figure 3.16, blue highlight on the left) and the correspondingly high concentration of tripeptide stems (Figure 3.9). From the observed proximities of the cross-linked D-alanyl methyl-carbon label to the bridge  $^{13}\text{C}$  and  $^{15}\text{N}$  labels, and from the 50% cross-linking limit, we conclude that the peptidoglycan of *E. faecalis* has the same short-bridge architecture as the FemA mutant of *S. aureus* [29].

With the composition and architecture of the peptidoglycan of *E. faecalis* established by implementation of solid-state NMR the labeling strategy of Table 1, we are now in a position to explore the mode(s) of action of the drug oritavancin which is potent against both vancomycin-susceptible and vancomycin-resistant strains *E. faecalis* [33, 34].

### *E. faecalis* cell-wall architecture

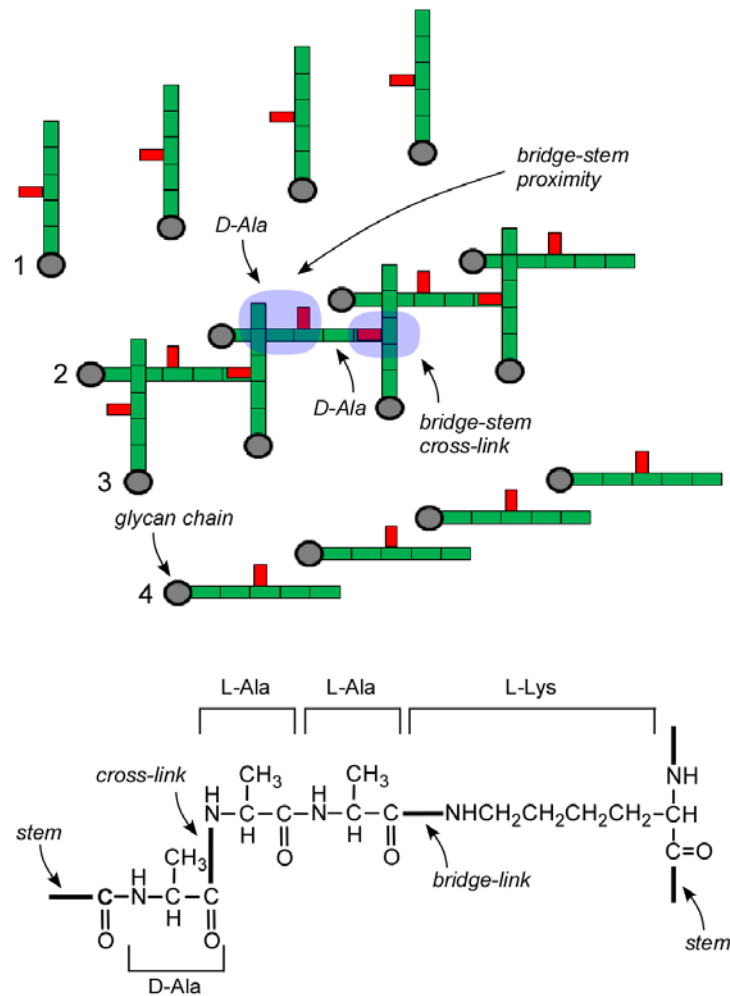


Figure 3.17 Lattice model for the peptidoglycan of short-bridged *E. faecalis*. A 4x4 array of glycan chains perpendicular to the plane of the paper is in gray, with the peptide stems in green and the bridges in red. The view is a slice transverse to the glycan chain direction of Figure 3.16 which shows that the D-Ala of one stem is proximate to the bridge of an adjacent stem (blue highlight on the right). The activity of D,D-carboxypeptidase (see Figure 3.9, top) means that uncross-linked terminal D-alanyl units (blue highlight on the left) are mostly removed. Alternate rows have stems that are perpendicular to one another. Thus, the stems of rows 1 and 3 are parallel, and those of rows 2 and 4 are parallel. Counts for the central four strands of the unit cell indicate that ideal (maximum) cross-linking is 50% [29]. The inset at the bottom of the figure shows a pair of cross-linked stems perpendicular to one another.

## 3.5 References

1. Maccallum, W.G. and Hastings, T.W., *A Case of Acute Endocarditis Caused by Micrococcus Zymogenes (Nov. Spec.), with a Description of the Microorganism*. The Journal of Experimental Medicine, 1899. **4**(5-6): 521-34.
2. Hendrickx, A.P.A., van Schaik, W., and Willems, R.J.L., *The Cell Wall Architecture of Enterococcus faecium: From Resistance to Pathogenesis*. Future Microbiology, 2013. **8**(8): 993-1010.
3. Gilmore, M.S., Lebreton, F., and van Schaik, W., *Genomic Transition of Enterococci from Gut Commensals to Leading Causes of Multidrug-Resistant Hospital Infection in the Antibiotic Era*. Current Opinion in Microbiology, 2013. **16**(1): 10-16.
4. Cetinkaya, Y., Falk, P., and Mayhall, C.G., *Vancomycin-Resistant Enterococci*. Clinical Microbiology Reviews, 2000. **13**(4): 686-707.
5. Leclercq, R., Derlot, E., Duval, J., and Courvalin, P., *Plasmid-Mediated Resistance to Vancomycin and Teicoplanin in Enterococcus-faecium*. New England Journal of Medicine, 1988. **319**(3): 157-161.
6. Uttley, A.H.C., Collins, C.H., Naidoo, J., and George, R.C., *Vancomycin-Resistant Enterococci*. Lancet, 1988. **1**(8575-6): 57-58.
7. Arias, C.A. and Murray, B.E., *The Rise of the Enterococcus: Beyond Vancomycin Resistance*. Nature Reviews Microbiology, 2012. **10**(4): 266-278.
8. Giraffa, G., *Enterococci from Foods*. Fems Microbiology Reviews, 2002. **26**(2): 163-171.
9. Sherman, J.M., *The Streptococci*. Bacteriological Reviews, 1937. **1**(1): 3-97.
10. Bugg, T.D.H., Wright, G.D., Dutkamalen, S., Arthur, M., Courvalin, P., and Walsh, C.T., *Molecular-Basis for Vancomycin Resistance in Enterococcus-faecium BM4147 -*

- Biosynthesis of a Depsipeptide Peptidoglycan Precursor by Vancomycin Resistance Proteins Vanh and Vana*. *Biochemistry*, 1991. **30**(43): 10408-10415.
11. Atherton, F.R., Hall, M.J., Hassall, C.H., Lambert, R.W., Lloyd, W.J., and Ringrose, P.S., *Phosphonopeptides as Antibacterial Agents - Mechanism of Action of Alaphosphin*. *Antimicrobial Agents and Chemotherapy*, 1979. **15**(5): 696-705.
  12. Tong, G., Pan, Y., Dong, H., Pryor, R., Wilson, G.E., and Schaefer, J., *Structure and Dynamics of Pentaglycyl Bridges in the Cell Walls of Staphylococcus aureus by  $^{13}\text{C}\{^{15}\text{N}\}$  REDOR NMR*. *Biochemistry*, 1997. **36**(32): 9859-9866.
  13. Kim, S.J., Cegelski, L., Studelska, D.R., O'Connor, R.D., Mehta, A.K., and Schaefer, J., *Rotational-Echo Double Resonance Characterization of Vancomycin Binding Sites in Staphylococcus aureus*. *Biochemistry*, 2002. **41**(22): 6967-6977.
  14. Zhou, X.X. and Cegelski, L., *Nutrient-Dependent Structural Changes in S. aureus Peptidoglycan Revealed by Solid-State NMR Spectroscopy*. *Biochemistry*, 2012. **51**(41): 8143-8153.
  15. Stueber, D., Mehta, A.K., Chen, Z.Y., Wooley, K.L., and Schaefer, J., *Local Order in Polycarbonate Glasses by  $^{13}\text{C}\{^{19}\text{F}\}$  Rotational-Echo Double-Resonance NMR*. *Journal of Polymer Science Part B-Polymer Physics*, 2006. **44**(19): 2760-2775.
  16. Gullion, T., Baker, D.B., and Conradi, M.S., *New, Compensated Carr-Purcell Sequences*. *Journal of Magnetic Resonance*, 1990. **89**(3): 479-484.
  17. Gullion, T. and Schaefer, J., *Elimination of Resonance Offset Effects in Rotational-Echo, Double-Resonance NMR*. *Journal of Magnetic Resonance*, 1991. **92**(2): 439-442.
  18. Weldeghiorghis, T.K. and Schaefer, J., *Compensating for Pulse Imperfections in REDOR*. *Journal of Magnetic Resonance*, 2003. **165**(2): 230-236.

19. Bork, V. and Schaefer, J., *Measuring  $^{13}\text{C}$ - $^{13}\text{C}$  Connectivity in Spinning Solids by Selective Excitation*. Journal of Magnetic Resonance, 1988. **78**(2): 348-354.
20. Cegelski, L. and Schaefer, J., *Glycine Metabolism in Intact Leaves by in Vivo  $^{13}\text{C}$  and  $^{15}\text{N}$  Labeling*. Journal of Biological Chemistry, 2005. **280**(47): 39238-39245.
21. Walsh, C.T., *Enzymes in the D-Alanine Branch of Bacterial-Cell Wall Peptidoglycan Assembly*. Journal of Biological Chemistry, 1989. **264**(5): 2393-2396.
22. McDowell, L.M., Schmidt, A., Cohen, E.R., Studelska, D.R., and Schaefer, J., *Structural Constraints on the Ternary Complex of 5-Enolpyruvylshikimate-3-Phosphate Synthase from Rotational-Echo Double-Resonance NMR*. Journal of Molecular Biology, 1996. **256**(1): 160-171.
23. Garbow, J.R., Jacob, G.S., Stejskal, E.O., and Schaefer, J., *Protein Dynamics from Chemical-Shift and Dipolar Rotational Spin-Echo  $^{15}\text{N}$  NMR*. Biochemistry, 1989. **28**(3): 1362-1367.
24. Theilacker, C., Holst, O., Lindner, B., Huebner, J., and Kaczynski, Z., *The Structure of the Wall Teichoic Acid Isolated from Enterococcus faecalis Strain 12030*. Carbohydrate Research, 2012. **354**: 106-109.
25. Patti, G.J., Kim, S.J., and Schaefer, J., *Characterization of the Peptidoglycan of Vancomycin-Susceptible Enterococcus faecium*. Biochemistry, 2008. **47**(32): 8378-8385.
26. Singh, M. and Schaefer, J., *Chain Packing in Glassy Polymers by Natural-Abundance  $^{13}\text{C}$ - $^{13}\text{C}$  Spin Diffusion Using 2D Centerband-Only Detection of Exchange*. Journal of the American Chemical Society, 2011. **133**(8): 2626-2631.
27. Wilson, E.M. and Snell, E.E., *Metabolism of Alpha-Methylserine .1. Alpha-Methylserine Hydroxymethyltransferase*. Journal of Biological Chemistry, 1962. **237**(10): 3171-3179.

28. Bour, P., Budesinsky, M., Spirko, V., Kapitan, J., Sebestik, J., and Sychrovsky, V., *A Complete Set of NMR Chemical Shifts and Spin-Spin Coupling Constants for L-Alanyl-L-Alanine Zwitterion and Analysis of Its Conformational Behavior*. Journal of the American Chemical Society, 2005. **127**(48): 17079-17089.
29. Kim, S.J., Singh, M., Sharif, S., and Schaefer, J., *Cross-Link Formation and Peptidoglycan Lattice Assembly in the FemA Mutant of Staphylococcus aureus*. Biochemistry, 2014. **53**(9): 1420-1427.
30. Gullion, T. and Schaefer, J., *Rotational-Echo Double-Resonance NMR*. Journal of Magnetic Resonance, 1989. **81**(1): 196-200.
31. Pan, Y., Gullion, T., and Schaefer, J., *Determination of C-N Internuclear Distances by Rotational-Echo Double-Resonance NMR of Solids*. Journal of Magnetic Resonance, 1990. **90**(2): 330-340.
32. Mueller, K.T., Jarvie, T.P., Aurentz, D.J., and Roberts, B.W., *The REDOR Transform - Direct Calculation of Internuclear Couplings from Dipolar-Dephasing NMR Data*. Chemical Physics Letters, 1995. **242**(6): 535-542.
33. Allen, N.E. and Nicas, T.I., *Mechanism of Action of Oritavancin and Related Glycopeptide Antibiotics*. Fems Microbiology Reviews, 2003. **26**(5): 511-532.
34. Patti, G.J., Kim, S.J., Yu, T.Y., Dietrich, E., Tanaka, K.S.E., Parr, T.R., Far, A.R., and Schaefer, J., *Vancomycin and Oritavancin Have Different Modes of Action in Enterococcus faecium*. Journal of Molecular Biology, 2009. **392**(5): 1178-1191.

# Chapter 4

## Reversible CO<sub>2</sub> Capture Mechanism of a Humidity-Swing Polymeric Sorbent

### 4.1 Introduction

The atmospheric CO<sub>2</sub> concentration was around 280 ppm before the industrial revolution [1]. In 1958, when the earliest direct measurements of CO<sub>2</sub> in the atmosphere started at Mauna Loa Observatory in Hawaii, the atmospheric CO<sub>2</sub> concentration was 316 ppm (Figure 4.1) [2]. Since then, the atmospheric CO<sub>2</sub> concentration has increased rapidly, surpassing 400 ppm in 2015 (Figure 4.1) [2].

The atmospheric CO<sub>2</sub> concentration for the past 800,000 years (Figure 4.2) was obtained by analyzing CO<sub>2</sub> in air bubbles trapped in an Antarctic ice core [3, 4]. Measurements showed a natural variation in CO<sub>2</sub> concentration between 170 and 300 ppm during this extended period (Figure 4.2). However, shortly after the industrial revolution, the atmospheric CO<sub>2</sub> concentration began increasing in an accelerated manner (Figure 4.2) largely due to human activities. The atmospheric CO<sub>2</sub> concentration is projected to increase to 550 ppm to 900 ppm by the end of this

century (Figure 4.2). The rate and extent of the current rise in atmospheric CO<sub>2</sub> concentration are unparalleled, and pose unprecedented challenges to our environment.

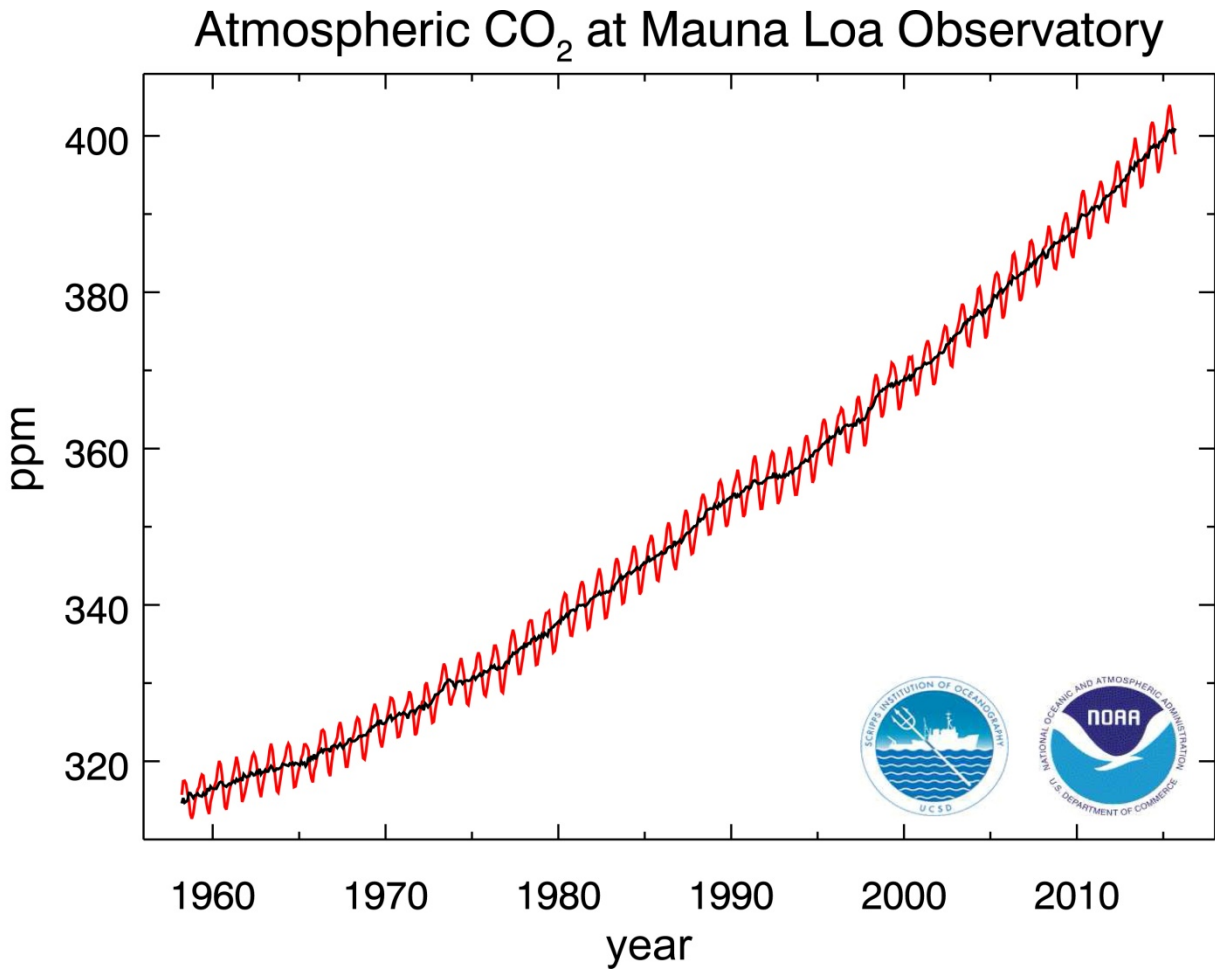


Figure 4.1 Atmospheric CO<sub>2</sub> concentration measured at Mauna Loa Observatory in Hawaii [2].

The black curve represents the seasonally corrected data.

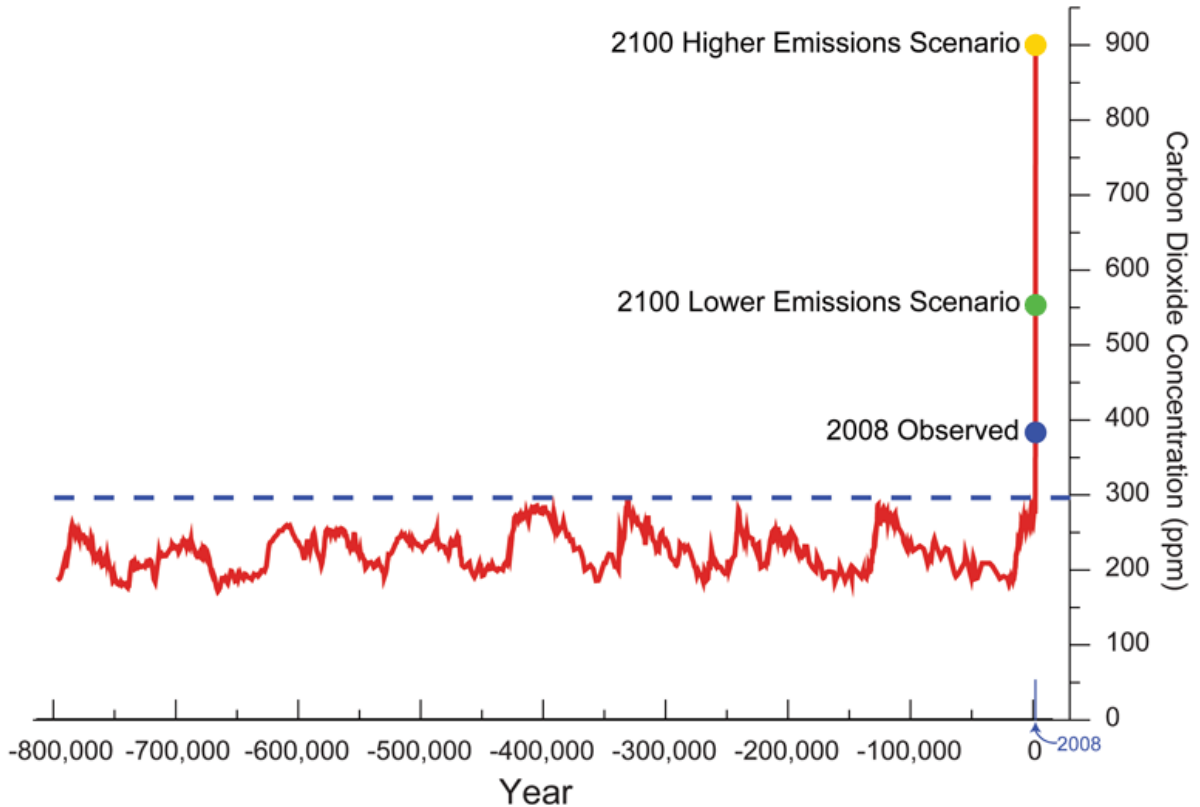


Figure 4.2 800,000 year record of atmospheric CO<sub>2</sub> concentration [2-4].

Carbon dioxide is a greenhouse gas. Along with the rise of the atmospheric CO<sub>2</sub> concentration, the global temperature has increased  $\sim 0.8$  °C in the past century [5]. During this period, slow global warming occurred up to 1975, followed by rapid warming at a rate of  $\sim 0.2$  °C per decade [5]. Global warming causes the retreat of glaciers, the rise of sea levels [3, 6-16], and profoundly changes the climate [17] including more frequent occurrence of extreme weather (heat waves, droughts, record rains and floods, *etc*) [18-24], increased likelihood of strong El Niños [5], higher intensity of tropical storms [25], *etc*. Global warming and climate change put the ecosystem under stress and cause extinction of species [5, 26-31]. Permafrost in Siberia, Northern Canada, and Greenland is at high risk to thaw due to global warming, and can

potentially release huge amounts of CO<sub>2</sub> and CH<sub>4</sub> [32-34]. CH<sub>4</sub> is a potent greenhouse gas and has 25 times more warming potential than CO<sub>2</sub> [32]. Thus the melting of the permafrost will in turn accelerate global warming [33, 34].

A study has revealed that global warming may not be alleviated immediately following the cessation of CO<sub>2</sub> emissions [35]. This means that global warming and climate change due to CO<sub>2</sub> emissions is potentially irreversible [35], and the study estimates that following the termination of CO<sub>2</sub> emissions, the atmospheric temperature will not drop significantly for at least 1,000 years [35].

Agriculture will be directly impacted by global warming and climate change. Recent studies indicate that the global yields of wheat, maize, barley, and rice decline with increased temperatures [36, 37]. More frequent extreme weather also impairs crop yields, *e.g.* the drought in the midwest region of the United States in 2012 [18]. One conjecture argues that the global crop yield losses caused by global warming and climate change can be offset by the direct fertilization effect from the rising CO<sub>2</sub> concentration in the atmosphere [38]. However, recent studies indicate that the crop yield increase caused by the rising CO<sub>2</sub> concentration is much lower than expected and is unlikely to offset the losses caused by global warming and climate change [38, 39].

Furthermore, the increased CO<sub>2</sub> concentration affects the environment not only by causing global warming and climate change, but also by directly acidifying the ocean, putting the ocean ecosystem under enormous stress [40-42].

The consequences of the rising CO<sub>2</sub> concentration in the atmosphere are serious and urgent, calling for our immediate actions to reduce emissions, switch to clean and renewable energy sources, and develop economical and effective methods to capture and sequester CO<sub>2</sub> from the atmosphere. Traditionally, liquid hydroxide solutions have been used to capture CO<sub>2</sub> from power plant flue gas by transforming CO<sub>2</sub> to carbonate species [43, 44]. However, this method is costly, involving multiple steps, and can not capture CO<sub>2</sub> directly from the atmosphere. In recent years, research on using solid sorbents to capture CO<sub>2</sub> has flourished, and many sorbents have been developed or repurposed such as zeolites, metal-organic frameworks (MOFs), carbon nanotubes (CNTs), amine-modified mesoporous silica, calcium oxide, hydrotalcites, alkali ceramics *etc* [44-46]. Among these CO<sub>2</sub> sorbents, we are especially interested in a polymeric sorbent containing quaternary ammonium cations [47]. Its monomeric chemical structure is shown in Figure 4.3.

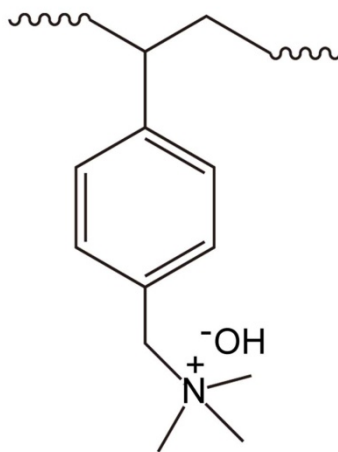


Figure 4.3 The chemical structure of the sorbent's monomeric unit.

Unlike many other sorbents, which are costly to make and require high temperature or high pressure to capture CO<sub>2</sub> [44-46], this sorbent containing quaternary ammonium cations can be

produced through simple steps at a low cost [47]. It captures and releases CO<sub>2</sub> at room temperature and atmospheric pressure [47]. The absorption and desorption of CO<sub>2</sub> is accomplished simply by varying the humidity level (Figure 4.4) [47].

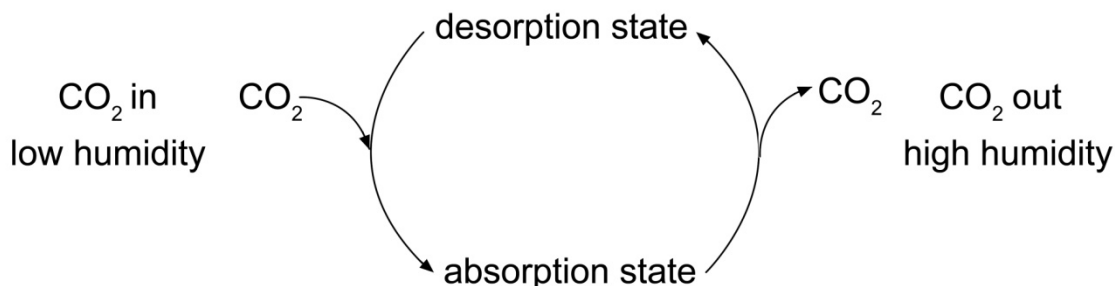


Figure 4.4 The scheme of the sorbent's CO<sub>2</sub> capture/release cycle driven by the humidity swing.

Recently, the polymeric sorbent has been synthesized by high internal phase emulsion polymerization [48], grafted on carbon black [49] and colloidal crystal templates [50] to make the sorbent's structure more porous [51]. Accordingly, its CO<sub>2</sub> absorption/desorption capacity and kinetics have been greatly improved [51], bringing the sorbent one step closer towards the actual implementation.

The sorbent exhibits promising potential. However, the chemical mechanism of the CO<sub>2</sub> absorption/desorption process remains largely elusive despite thermodynamic analysis [52, 53]. Here we apply solid-state NMR to probe the CO<sub>2</sub> absorption/desorption mechanism directly, and hope detailed understanding of the mechanism yields insights for developing better sorbents.

## 4.2 Materials and Methods

### 4.2.1 The Polymeric Sorbent

The polymeric sorbent was provided by Professor Krzysztof Matyjaszewski and Professor Tomas Kowalewski at Carnegie Mellon University. The sorbent is in the form of a powder.

### 4.2.2 Solid-State NMR Experiments

*$^{13}\text{C}$  CPMAS echo,  $^{13}\text{C}$  CPMAS echo  $^1\text{H}$  interrupted decoupling, and  $^2\text{H}$  Hahn echo experiments.*

The NMR spectrometer has an 89-mm bore, 12-T static field ( $^1\text{H}$  at 500 MHz, Magnex, Agilent, Santa Clara, CA), a Tecmag (Houston, TX) Apollo console, and a homebuilt four-channel ( $^1\text{H}$ ,  $^{19}\text{F}$ ,  $^{13}\text{C}$ ,  $^2\text{H}$ ) transmission-line probe equipped with a 5 mm Chemagnetics/Varian stator and zirconium rotors. Radio frequency pulses for  $^1\text{H}$  were amplified first by a 50-W American Microwave Technology (AMT, Anaheim, CA) power amplifier and then by a 2-kW Creative Electronics tube amplifier. AMT amplifiers (2 kW) were used for  $^{13}\text{C}$  and  $^2\text{H}$  pulses. In all the NMR experiments, 71 kHz pulses (7  $\mu\text{s}$  for  $\pi$  pulses) were used for  $^1\text{H}$ ,  $^{13}\text{C}$  and  $^2\text{H}$ , and the proton decoupling strength was 71 kHz. Matched cross-polarization transfers were made at 71 kHz in 1.5 ms in the  $^{13}\text{C}$  CPMAS echo and  $^{13}\text{C}$  CPMAS echo  $^1\text{H}$  interrupted decoupling experiments. Adamantane was used as an external  $^{13}\text{C}$  chemical shift reference [54]. Spinning rates were actively controlled to  $8000\pm 2$  Hz. All RF pulse amplitudes were under active control ( $\text{H}_1$  control) to eliminate long-term drifts due to component aging or changes in temperature [55].

*$^{13}\text{C}\{^{15}\text{N}\}$  REDOR experiments.* Experiments were performed at 12 T with a six-frequency transmission-line probe having a 12-mm long, 6-mm inner-diameter analytical coil, and a

Chemagnetics/Varian ceramic spinning module. Samples were spun using a thin-wall Chemagnetics/Varian (Fort Collins, CO/Palo Alto, CA) 5-mm outer diameter-zirconia rotor at 7143 Hz, with the speed under active control and maintained to within  $\pm 2$  Hz. A Tecmag Libra pulse programmer (Houston, TX) controlled the spectrometer. 2-kW American Microwave Technology (AMT) power amplifiers were used to produce radio-frequency pulses for  $^{13}\text{C}$  (125 MHz) and  $^{15}\text{N}$  (50 MHz). The  $^1\text{H}$  (500 MHz) radio frequency pulses were generated by a 2-kW Creative Electronics tube amplifiers driven by 50-W AMT amplifiers. All final-stage amplifiers were under active control [55]. The  $\pi$ -pulse lengths were 9  $\mu\text{s}$  for  $^{13}\text{C}$  and  $^1\text{H}$ , 8  $\mu\text{s}$  for  $^{15}\text{N}$ . Proton carbon-matched cross-polarization transfers were made in 4 ms at 56 kHz. Proton dipolar decoupling was 100 kHz during data acquisition. The  $S$  and  $S_0$  alternate-scan strategy compensated for short-term drifts in REDOR experiments. Standard XY-8 phase cycling [56] was used for all refocusing observe-channel  $\pi$  pulses (inserted at the end of each rotor period during dipolar evolution) and dephasing  $\pi$  pulses (inserted in the middle of each rotor period) to compensate for pulse imperfections [57, 58].

### 4.3 Results and Discussion

The polymeric sorbent was vacuum dried and exposed to 90%  $^{13}\text{C}$  enriched pure  $\text{CO}_2$  ( $^{13}\text{CO}_2$ ) gas in a sealed container connected to a Schleck line (vacuum gas manifold). The  $^{13}\text{C}$  CPMAS echo spectra of the polymeric sorbent before (Figure 4.5, top spectrum) and after (Figure 4.5, middle spectrum) the absorption of  $^{13}\text{CO}_2$  unambiguously indicate that the  $^{13}\text{CO}_2$  has been chemically absorbed due to the appearance of a new intense peak at 161 ppm (Figure 4.5, middle spectrum). Bubbling humidified  $\text{N}_2$  gas through the  $\text{CO}_2$  absorbed sorbent for 25 minutes almost completely desorbed the  $\text{CO}_2$  (Figure 4.5, bottom spectrum). Thus the  $^{13}\text{C}$  CPMAS echo measurements clearly prove the reversible  $\text{CO}_2$  capture/release cycle of the sorbent simply by varying the humidity level.

The sorbent's chemical structure remains intact through the  $\text{CO}_2$  capture/release process, as evidenced by the fact that the intensities and chemical shifts of the sorbent  $^{13}\text{C}$  peaks remain unchanged (Figure 4.5). The possibility of physical adsorption of  $\text{CO}_2$  is ruled out because physically adsorbed  $\text{CO}_2$  would exhibit a chemical shift around 125 ppm. The 161 ppm chemical shift value suggests that the  $\text{CO}_2$  has been absorbed as carbonate ( $\text{CO}_3^{2-}$ ) or bicarbonate ( $\text{HCO}_3^-$ ), consistent with the nature of the sorbent as an anion exchange resin.

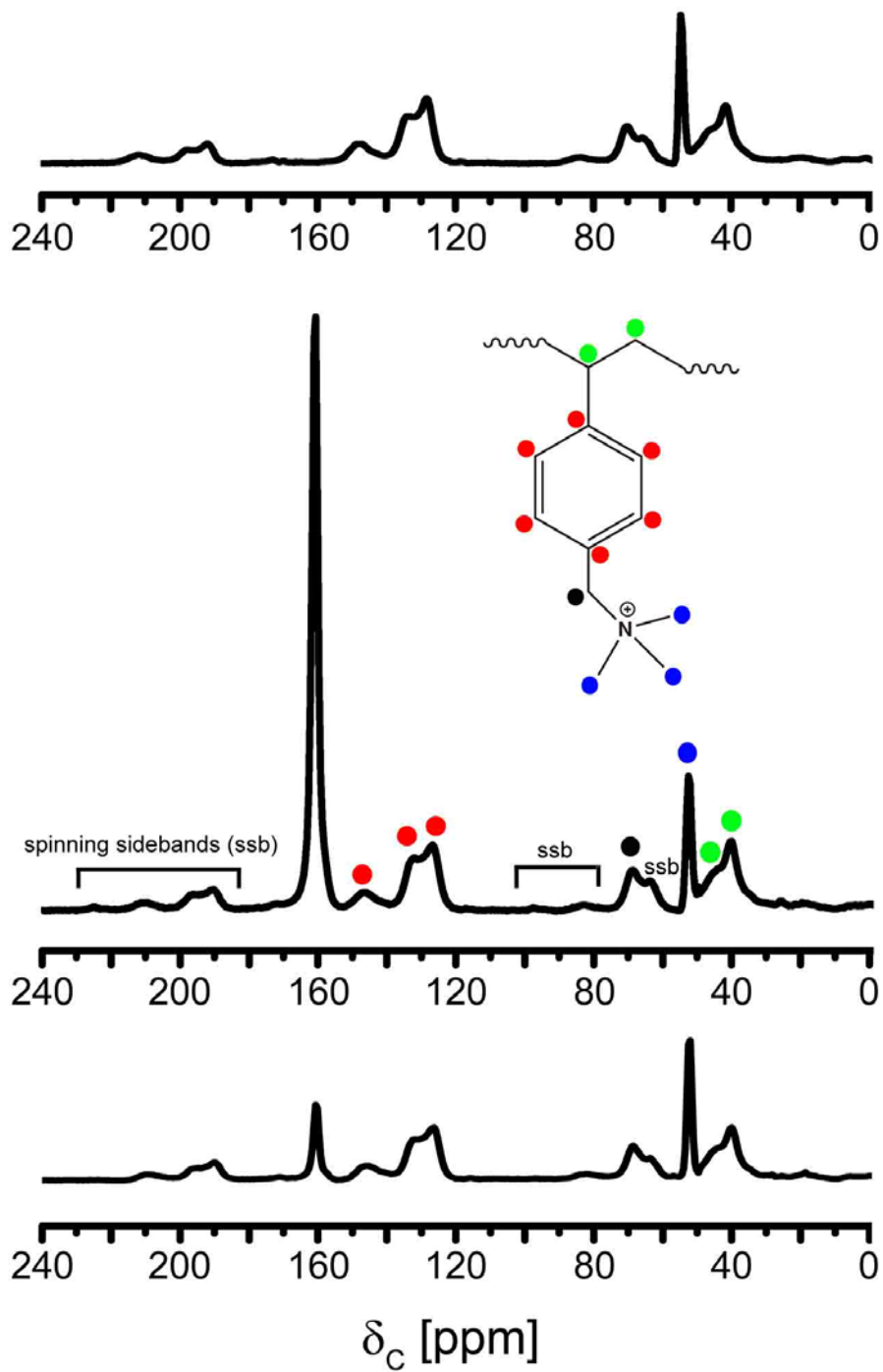


Figure 4.5  $^{13}\text{C}$  CPMAS echo spectra of the sorbent before (top) and after (middle) the absorption of  $^{13}\text{CO}_2$ . Bubbling humidified  $\text{N}_2$  gas through the  $^{13}\text{CO}_2$  absorbed sorbent for 25 minutes led to  $\text{CO}_2$  desorption (bottom).

The chemical shift value by itself is unable to distinguish between  $\text{CO}_3^{2-}$  and  $\text{HCO}_3^-$ . Thus,  $^{13}\text{C}$  CPMAS echo  $^1\text{H}$  interrupted decoupling experiments were used to probe the chemical nature of the absorbed 161 ppm  $^{13}\text{C}$  peak. The pulse sequence of the  $^{13}\text{C}$  CPMAS echo  $^1\text{H}$  interrupted decoupling experiment is shown in Figure 4.6. Here the  $^1\text{H}$  decoupling is turned off for a small duration to allow the recoupling between the  $^{13}\text{C}$  spin and homogeneous  $^1\text{H}$  spins. This recoupling results in relaxation and an intensity reduction for the observed  $^{13}\text{C}$  peaks.

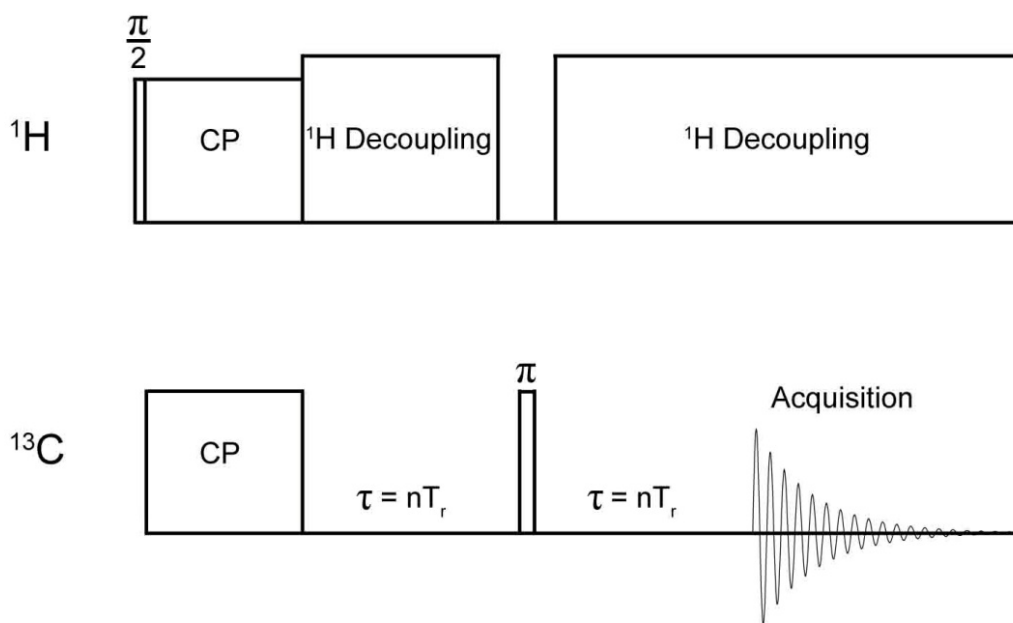


Figure 4.6 The pulse sequence of the  $^{13}\text{C}$  CPMAS echo  $^1\text{H}$  interrupted decoupling experiment.

The key difference between  $\text{CO}_3^{2-}$  and  $\text{HCO}_3^-$  is that  $\text{HCO}_3^-$  has a nearby proton about 1.9 Å away from the carbon (Figure 4.7, inset structure of the right spectrum) [59]. If the absorbed 161 ppm carbon is  $\text{HCO}_3^-$ , similar peak intensity reduction compared to that of a  $\text{NaHCO}_3$  standard would be expected in the  $^{13}\text{C}$  CPMAS echo  $^1\text{H}$  interrupted decoupling experiments. On the other hand, if the absorbed 161 ppm carbon is  $\text{CO}_3^{2-}$ , smaller peak intensity reduction compared to that of a  $\text{NaHCO}_3$  standard would be expected. In the  $^{13}\text{C}$  CPMAS echo  $^1\text{H}$  interrupted decoupling experiments with an interrupted decoupling duration of 80 μs, an 8% peak reduction was observed for the 161 ppm  $^{13}\text{C}$  peak (Figure 4.7, left spectrum), whereas a 35% peak reduction was observed for the  $\text{NaHCO}_3$  standard (Figure 4.7, right spectrum). The measurements suggest that the absorbed 161 ppm  $^{13}\text{C}$  peak is likely  $\text{CO}_3^{2-}$ .

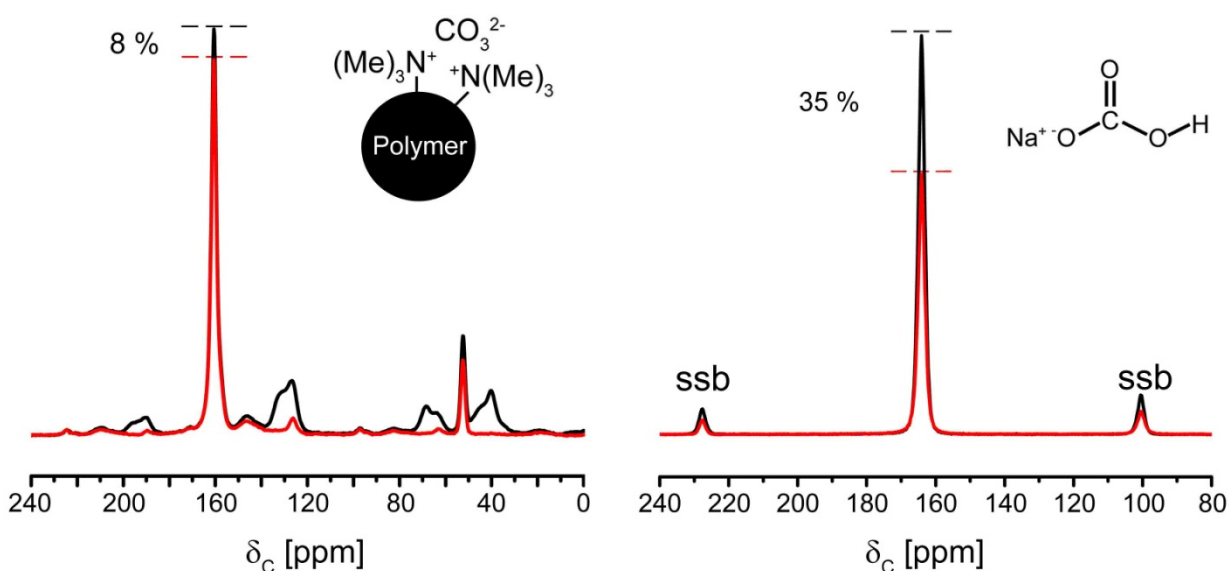


Figure 4.7  $^{13}\text{C}$  CPMAS echo  $^1\text{H}$  interrupted decoupling spectra of the  $^{13}\text{CO}_2$  absorbed sorbent (left) and a  $\text{NaHCO}_3$  standard (right) with an interrupted decoupling duration of 80 μs.

If CO<sub>2</sub> is absorbed as carbonate (CO<sub>3</sub><sup>2-</sup>), which serve as the counter ions of the quaternary ammonium cations, the 161 ppm <sup>13</sup>C would be spatially close to the nitrogen (Figure 4.7, inset structure of the left spectrum). This proximity is probed by <sup>13</sup>C{<sup>15</sup>N} REDOR experiments. The observed dephasing (Figure 4.8) confirms that the absorbed <sup>13</sup>C is spatially close to the nitrogen of the quaternary ammonium cations. Thus it is clear that the quaternary ammonium cations are the functional groups responsible for the CO<sub>2</sub> capture in the sorbent, and the CO<sub>2</sub> is absorbed as CO<sub>3</sub><sup>2-</sup> counter ions.

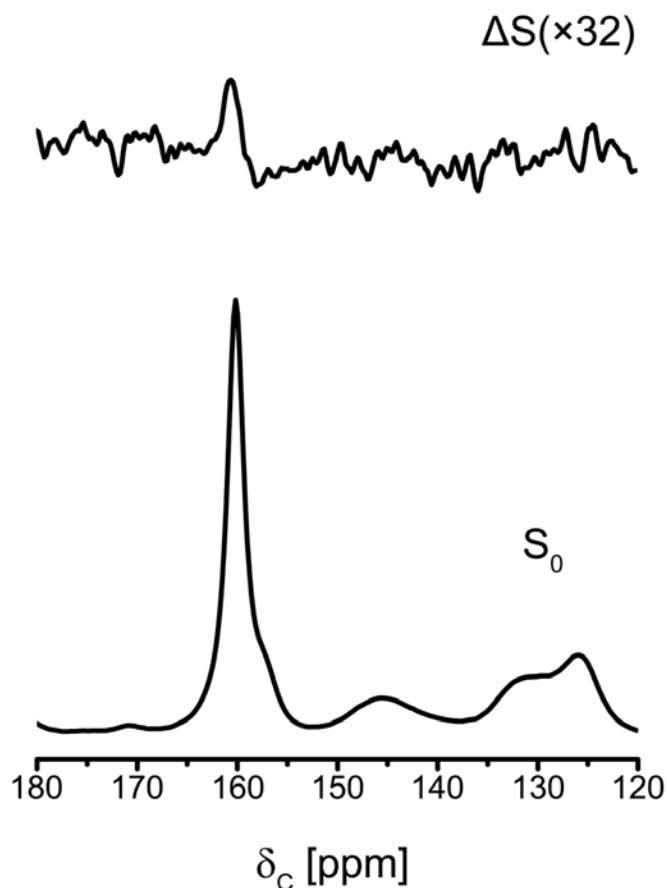


Figure 4.8 <sup>13</sup>C{<sup>15</sup>N} REDOR spectra of the <sup>13</sup>CO<sub>2</sub> absorbed sorbent with 4.48 ms dephasing time and ~ 200,000 scans.

The  $^{13}\text{C}$  CPMAS echo spectrum of the  $\text{CO}_2$  desorbed sorbent (Figure 4.5, bottom spectrum) clearly indicates the release of the absorbed  $\text{CO}_2$  after exposing the sorbent to humidified air. Upon desorption, the  $\text{CO}_3^{2-}$  anions must be replaced by a different kind of anion to serve as the counter ions of the quaternary ammonium cations. Since only humidified  $\text{N}_2$  gas is present upon  $\text{CO}_2$  desorption, it is plausible that  $\text{CO}_3^{2-}$  has been replaced by  $\text{OH}^-$ . To probe the chemical nature of the desorbed sorbent,  $\text{D}_2\text{O}$  humidified  $\text{N}_2$  gas was used to remove the absorbed  $\text{CO}_2$ . The deuterium Hahn echo spectrum of the  $\text{CO}_2$  desorbed sorbent indicates the deuterium labels have been absorbed by the sorbent upon  $\text{CO}_2$  desorption (Figure 4.9). In the deuterium Hahn echo spectrum, two types of deuterium were observed (Figure 4.9). The immobile deuterium is the major component and shows an obvious Pake pattern (Figure 4.9), which is a characteristic of deuterium in solid state. The immobile deuterium is assigned as  $\text{OD}^-$ , and the strong attraction between the  $\text{OD}^-$  anions and quaternary ammonium cations probably restricts the molecular motions of the  $\text{OD}^-$  and makes the deuterium immobile. The mobile deuterium is a minor component (Figure 4.9). Unlike the Pake pattern, the mobile deuterium shows more intensity in the center bands (Figure 4.9) due to the averaging effect of the molecular motions on the anisotropic quadrupolar interaction. The mobile deuterium is assigned as physically adsorbed  $\text{D}_2\text{O}$ . The weak adsorption force allows molecular motions for  $\text{D}_2\text{O}$ , making the deuterium mobile.

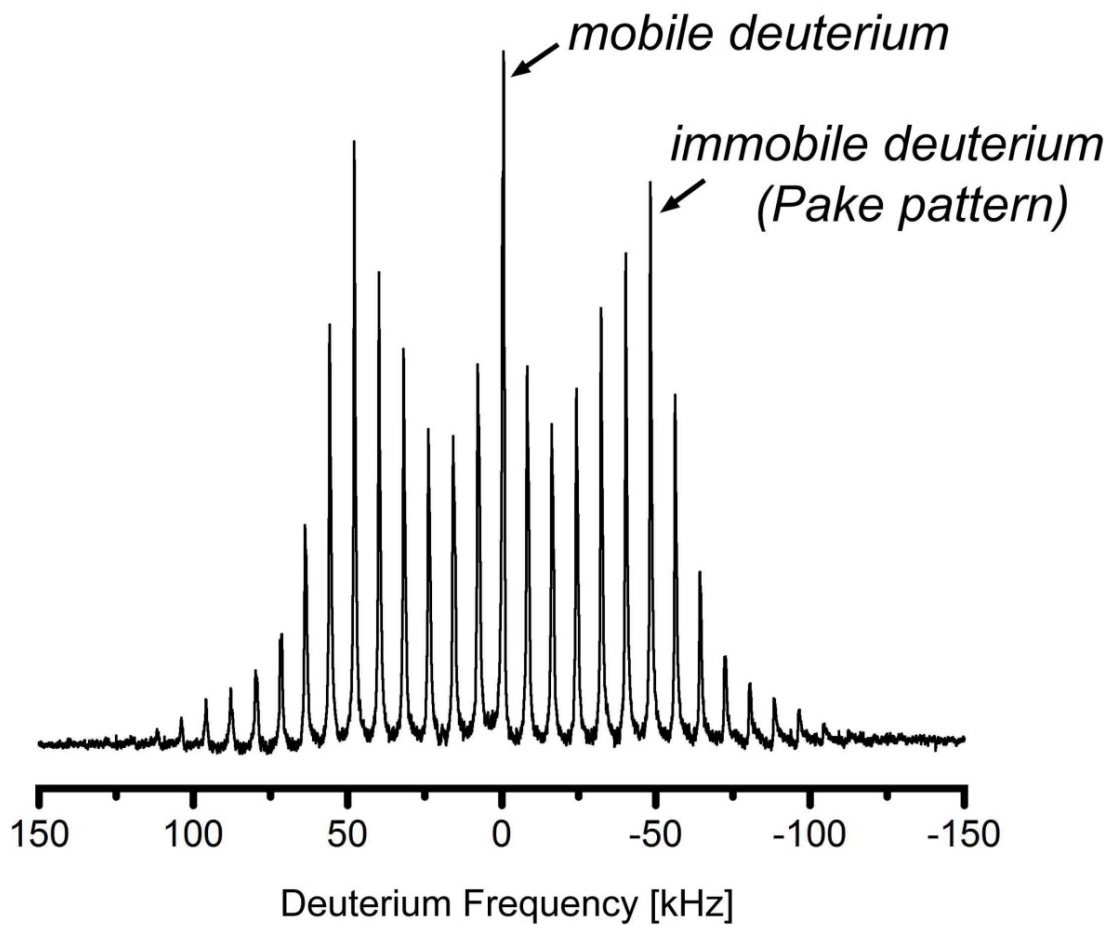


Figure 4.9 The deuterium Hahn echo spectrum of the CO<sub>2</sub> desorbed sorbent. Exposure of the sorbent to D<sub>2</sub>O humidified N<sub>2</sub> gas led to CO<sub>2</sub> desorption.

By putting all the NMR evidence together, the detailed mechanism of the sorbent's CO<sub>2</sub> capture/release cycle driven by the humidity swing is elucidated (Figure 4.10 and 4.11). This process can be readily explained by the principle of chemical equilibrium. When the humidity level in the environment is low, the sorbent prefers to capture CO<sub>2</sub> and release water into the environment. Conversely, when the humidity level is high, the sorbent prefers to release CO<sub>2</sub> and capture water from the environment.

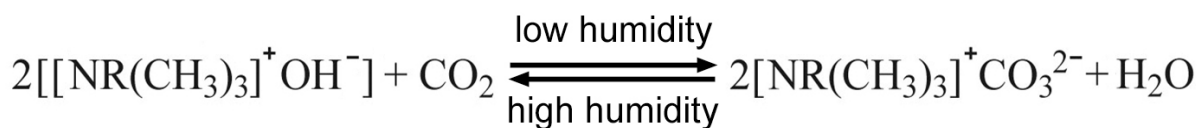


Figure 4.10 The chemical equation of the sorbent's CO<sub>2</sub> capture/release cycle driven by the humidity swing.

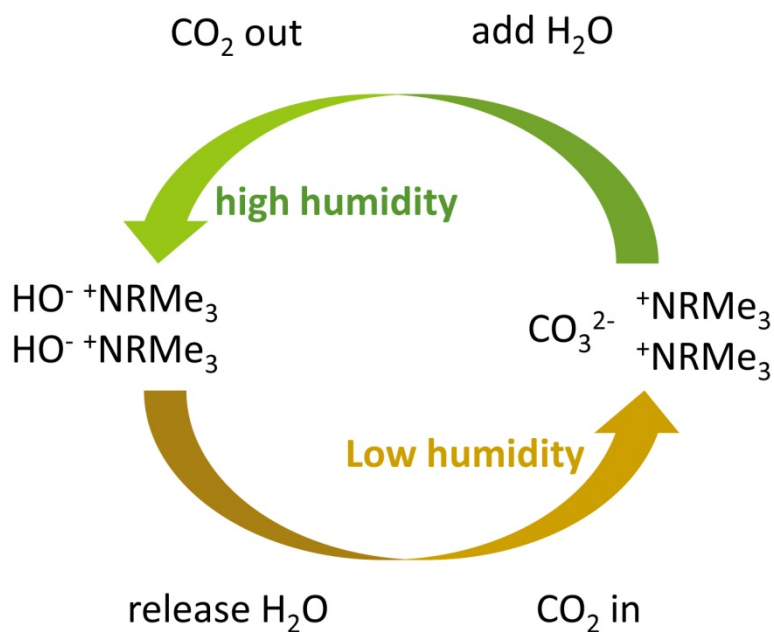


Figure 4.11 The scheme of the CO<sub>2</sub> capture/release mechanism for the humidity-swing sorbent.

## 4.4 Conclusion

In conclusion, solid-state NMR spectroscopy has been used to investigate the CO<sub>2</sub> capture/release mechanism of a humidity-swing sorbent successfully. The mechanism is readily explained by the principle of chemical equilibrium (Figure 4.10 and 4.11). The sorbent itself is economical to make. It captures and releases CO<sub>2</sub> at room temperature and atmospheric pressure by simply varying the humidity level. These advantages significantly lower the cost of the CO<sub>2</sub> capture and make the sorbent a competitive candidate for actual implementation [43, 60]. The elucidation of the detailed CO<sub>2</sub> capture mechanism certainly provides insights for the further improvement of the sorbent's performance.

To capture CO<sub>2</sub> from air is only the first step. The subsequent sequestration is also crucial. We envision using the captured CO<sub>2</sub> to provide above-ambient CO<sub>2</sub> levels for growing genetically-engineered algae to produce biofuels and fine chemicals [61-64]. After the separation and collection of the biofuels and fine chemicals, the algal remains can be converted to biochar through exothermic pyrolysis and dumped underground to serve as a carbon reservoir, thus preventing much of the algal carbon from being reintroduced into the atmosphere. Biochar is stable for hundreds to thousands of years, and has been shown to improve the structure and fertility of soils [65]. These advantages make biochar an ideal sequestration option after the CO<sub>2</sub> capture.

## 4.5 References

1. Monastersky, R., *Global Carbon Dioxide Levels near Worrisome Milestone*. *Nature*, 2013. **497**(7447): 13-14.
2. Dr. Pieter Tans, NOAA/ESRL ([www.esrl.noaa.gov/gmd/ccgg/trends/](http://www.esrl.noaa.gov/gmd/ccgg/trends/)) and Dr. Ralph Keeling, Scripps Institution of Oceanography ([scrippsco2.ucsd.edu/](http://scrippsco2.ucsd.edu/)).
3. Karl, T.R., *Global Climate Change Impacts in the United States*. 2009: Cambridge University Press.
4. Luthi, D., Le Floch, M., Bereiter, B., Blunier, T., Barnola, J.M., Siegenthaler, U., Raynaud, D., Jouzel, J., Fischer, H., Kawamura, K., and Stocker, T.F., *High-Resolution Carbon Dioxide Concentration Record 650,000-800,000 Years before Present*. *Nature*, 2008. **453**(7193): 379-382.
5. Hansen, J., Sato, M., Ruedy, R., Lo, K., Lea, D.W., and Medina-Elizade, M., *Global Temperature Change*. *Proceedings of the National Academy of Sciences of the United States of America*, 2006. **103**(39): 14288-14293.
6. IPCC, *Climate Change 2001: The Scientific Basis*. 2001: Cambridge University Press.
7. Strauss, B.H., Kulp, S., and Levermann, A., *Carbon Choices Determine US Cities Committed to Futures Below Sea Level*. *Proceedings of the National Academy of Sciences*, 2015. **112**(44): 13508-13513.
8. Church, J.A. and White, N.J., *A 20th Century Acceleration in Global Sea-Level Rise*. *Geophysical Research Letters*, 2006. **33**(1).

9. Overpeck, J.T., Otto-Bliesner, B.L., Miller, G.H., Muhs, D.R., Alley, R.B., and Kiehl, J.T., *Paleoclimatic Evidence for Future Ice-Sheet Instability and Rapid Sea-Level Rise*. Science, 2006. **311**(5768): 1747-1750.
10. Rahmstorf, S., *A Semi-Empirical Approach to Projecting Future Sea-Level Rise*. Science, 2007. **315**(5810): 368-370.
11. Meier, M.F., Dyurgerov, M.B., Rick, U.K., O'Neel, S., Pfeffer, W.T., Anderson, R.S., Anderson, S.P., and Glazovsky, A.F., *Glaciers Dominate Eustatic Sea-Level Rise in the 21st Century*. Science, 2007. **317**(5841): 1064-1067.
12. Domingues, C.M., Church, J.A., White, N.J., Gleckler, P.J., Wijffels, S.E., Barker, P.M., and Dunn, J.R., *Improved Estimates of Upper-Ocean Warming and Multi-Decadal Sea-Level Rise*. Nature, 2008. **453**(7198): 1090-U6.
13. Pfeffer, W.T., Harper, J.T., and O'Neel, S., *Kinematic Constraints on Glacier Contributions to 21st-Century Sea-Level Rise*. Science, 2008. **321**(5894): 1340-1343.
14. Nicholls, R.J. and Cazenave, A., *Sea-Level Rise and Its Impact on Coastal Zones*. Science, 2010. **328**(5985): 1517-1520.
15. Rignot, E., Velicogna, I., van den Broeke, M.R., Monaghan, A., and Lenaerts, J., *Acceleration of the Contribution of the Greenland and Antarctic Ice Sheets to Sea Level Rise*. Geophysical Research Letters, 2011. **38**.
16. Church, J.A. and White, N.J., *Sea-Level Rise from the Late 19th to the Early 21st Century*. Surveys in Geophysics, 2011. **32**(4-5): 585-602.
17. Meehl, G.A., Zwiers, F., Evans, J., Knutson, T., Mearns, L., and Whetton, P., *Trends in Extreme Weather and Climate Events: Issues Related to Modeling Extremes in*

- Projections of Future Climate Change*. Bulletin of the American Meteorological Society, 2000. **81**(3): 427-436.
18. Tang, Q.H., Zhang, X.J., and Francis, J.A., *Extreme Summer Weather in Northern Mid-Latitudes Linked to a Vanishing Cryosphere*. Nature Climate Change, 2014. **4**(1): 45-50.
  19. Stott, P.A., Stone, D.A., and Allen, M.R., *Human Contribution to the European Heatwave of 2003*. Nature, 2004. **432**(7017): 610-614.
  20. Goswami, B.N., Venugopal, V., Sengupta, D., Madhusoodanan, M.S., and Xavier, P.K., *Increasing Trend of Extreme Rain Events over India in a Warming Environment*. Science, 2006. **314**(5804): 1442-1445.
  21. Luber, G. and McGeehin, M., *Climate Change and Extreme Heat Events*. American Journal of Preventive Medicine, 2008. **35**(5): 429-435.
  22. Schiermeier, Q., *Increased Flood Risk Linked to Global Warming*. Nature, 2011. **470**(7334): 316.
  23. Min, S.K., Zhang, X.B., Zwiers, F.W., and Hegerl, G.C., *Human Contribution to More-Intense Precipitation Extremes*. Nature, 2011. **470**(7334): 378-381.
  24. Pall, P., Aina, T., Stone, D.A., Stott, P.A., Nozawa, T., Hilberts, A.G.J., Lohmann, D., and Allen, M.R., *Anthropogenic Greenhouse Gas Contribution to Flood Risk in England and Wales in Autumn 2000*. Nature, 2011. **470**(7334): 382-385.
  25. Emanuel, K.A., *The Dependence of Hurricane Intensity on Climate*. Nature, 1987. **326**(6112): 483-485.
  26. Root, T.L., Price, J.T., Hall, K.R., Schneider, S.H., Rosenzweig, C., and Pounds, J.A., *Fingerprints of Global Warming on Wild Animals and Plants*. Nature, 2003. **421**(6918): 57-60.

27. Walther, G.R., Post, E., Convey, P., Menzel, A., Parmesan, C., Beebee, T.J.C., Fromentin, J.M., Hoegh-Guldberg, O., and Bairlein, F., *Ecological Responses to Recent Climate Change*. Nature, 2002. **416**(6879): 389-395.
28. Parmesan, C. and Yohe, G., *A Globally Coherent Fingerprint of Climate Change Impacts across Natural Systems*. Nature, 2003. **421**(6918): 37-42.
29. Parmesan, C., *Ecological and Evolutionary Responses to Recent Climate Change*. Annual Review of Ecology Evolution and Systematics, 2006. **37**: 637-669.
30. Pounds, J.A., Bustamante, M.R., Coloma, L.A., Consuegra, J.A., Fogden, M.P.L., Foster, P.N., La Marca, E., Masters, K.L., Merino-Viteri, A., Puschendorf, R., Ron, S.R., Sanchez-Azofeifa, G.A., Still, C.J., and Young, B.E., *Widespread Amphibian Extinctions from Epidemic Disease Driven by Global Warming*. Nature, 2006. **439**(7073): 161-167.
31. Walther, G.R., *Community and Ecosystem Responses to Recent Climate Change*. Philosophical Transactions of the Royal Society B-Biological Sciences, 2010. **365**(1549): 2019-2024.
32. Schuur, E.A.G., Abbott, B., and Permafrost Carbon, N., *High Risk of Permafrost Thaw*. Nature, 2011. **480**(7375): 32-33.
33. Schuur, E.A.G., Bockheim, J., Canadell, J.G., Euskirchen, E., Field, C.B., Goryachkin, S.V., Hagemann, S., Kuhry, P., Lafleur, P.M., Lee, H., Mazhitova, G., Nelson, F.E., Rinke, A., Romanovsky, V.E., Shiklomanov, N., Tarnocai, C., Venevsky, S., Vogel, J.G., and Zimov, S.A., *Vulnerability of Permafrost Carbon to Climate Change: Implications for the Global Carbon Cycle*. Bioscience, 2008. **58**(8): 701-714.
34. Koven, C.D., Ringeval, B., Friedlingstein, P., Ciais, P., Cadule, P., Khvorostyanov, D., Krinner, G., and Tarnocai, C., *Permafrost Carbon-Climate Feedbacks Accelerate Global*

- Warming*. Proceedings of the National Academy of Sciences of the United States of America, 2011. **108**(36): 14769-14774.
35. Solomon, S., Plattner, G.K., Knutti, R., and Friedlingstein, P., *Irreversible Climate Change Due to Carbon Dioxide Emissions*. Proceedings of the National Academy of Sciences of the United States of America, 2009. **106**(6): 1704-1709.
36. Lobell, D.B. and Field, C.B., *Global Scale Climate - Crop Yield Relationships and the Impacts of Recent Warming*. Environmental Research Letters, 2007. **2**(1).
37. Peng, S.B., Huang, J.L., Sheehy, J.E., Laza, R.C., Visperas, R.M., Zhong, X.H., Centeno, G.S., Khush, G.S., and Cassman, K.G., *Rice Yields Decline with Higher Night Temperature from Global Warming*. Proceedings of the National Academy of Sciences of the United States of America, 2004. **101**(27): 9971-9975.
38. Long, S.P., Ainsworth, E.A., Leakey, A.D.B., Nosberger, J., and Ort, D.R., *Food for Thought: Lower-Than-Expected Crop Yield Stimulation with Rising CO<sub>2</sub> Concentrations*. Science, 2006. **312**(5782): 1918-1921.
39. Dirks, R.C., Singh, M., Potter, G.S., Sobotka, L.G., and Schaefer, J., *Carbon Partitioning in Soybean (Glycine Max) Leaves by Combined <sup>11</sup>C and <sup>13</sup>C Labeling*. New Phytologist, 2012. **196**(4): 1109-1121.
40. Orr, J.C., Fabry, V.J., Aumont, O., Bopp, L., Doney, S.C., Feely, R.A., Gnanadesikan, A., Gruber, N., Ishida, A., Joos, F., Key, R.M., Lindsay, K., Maier-Reimer, E., Matear, R., Monfray, P., Mouchet, A., Najjar, R.G., Plattner, G.K., Rodgers, K.B., Sabine, C.L., Sarmiento, J.L., Schlitzer, R., Slater, R.D., Totterdell, I.J., Weirig, M.F., Yamanaka, Y., and Yool, A., *Anthropogenic Ocean Acidification over the Twenty-First Century and Its Impact on Calcifying Organisms*. Nature, 2005. **437**(7059): 681-686.

41. Hoegh-Guldberg, O., Mumby, P.J., Hooten, A.J., Steneck, R.S., Greenfield, P., Gomez, E., Harvell, C.D., Sale, P.F., Edwards, A.J., Caldeira, K., Knowlton, N., Eakin, C.M., Iglesias-Prieto, R., Muthiga, N., Bradbury, R.H., Dubi, A., and Hatziolos, M.E., *Coral Reefs under Rapid Climate Change and Ocean Acidification*. *Science*, 2007. **318**(5857): 1737-1742.
42. Doney, S.C., Fabry, V.J., Feely, R.A., and Kleypas, J.A., *Ocean Acidification: The Other CO<sub>2</sub> Problem*. *Annual Review of Marine Science*, 2009. **1**: 169-192.
43. Socolow, R., Desmond, M., Aines, R., Blackstock, J., Bolland, O., Kaarsberg, T., Lewis, N., Mazzotti, M., Pfeffer, A., and Sawyer, K., *Direct Air Capture of CO<sub>2</sub> with Chemicals: A Technology Assessment for the APS Panel on Public Affairs*, 2011, American Physical Society.
44. Wang, Q.A., Luo, J.Z., Zhong, Z.Y., and Borgna, A., *CO<sub>2</sub> Capture by Solid Adsorbents and Their Applications: Current Status and New Trends*. *Energy & Environmental Science*, 2011. **4**(1): 42-55.
45. Choi, S., Drese, J.H., and Jones, C.W., *Adsorbent Materials for Carbon Dioxide Capture from Large Anthropogenic Point Sources*. *Chemosuschem*, 2009. **2**(9): 796-854.
46. Hedin, N., Chen, L.J., and Laaksonen, A., *Sorbents for CO<sub>2</sub> Capture from Flue Gas- Aspects from Materials and Theoretical Chemistry*. *Nanoscale*, 2010. **2**(10): 1819-1841.
47. Lackner, K.S., *Capture of Carbon Dioxide from Ambient Air*. *European Physical Journal-Special Topics*, 2009. **176**: 93-106.
48. He, H.K., Li, W.W., Lamson, M., Zhong, M.J., Konkolewicz, D., Hui, C.M., Yaccato, K., Rappold, T., Sugar, G., David, N.E., Damodaran, K., Natesakhawat, S., Nulwala, H., and

- Matyjaszewski, K., *Porous Polymers Prepared Via High Internal Phase Emulsion Polymerization for Reversible CO<sub>2</sub> Capture*. *Polymer*, 2014. **55**(1): 385-394.
49. He, H.K., Zhong, M.J., Konkolewicz, D., Yacatto, K., Rappold, T., Sugar, G., David, N.E., and Matyjaszewski, K., *Carbon Black Functionalized with Hyperbranched Polymers: Synthesis, Characterization, and Application in Reversible CO<sub>2</sub> Capture*. *Journal of Materials Chemistry A*, 2013. **1**(23): 6810-6821.
50. He, H.K., Zhong, M.J., Konkolewicz, D., Yacatto, K., Rappold, T., Sugar, G., David, N.E., Gelb, J., Kotwal, N., Merkle, A., and Matyjaszewski, K., *Three-Dimensionally Ordered Macroporous Polymeric Materials by Colloidal Crystal Templating for Reversible CO<sub>2</sub> Capture*. *Advanced Functional Materials*, 2013. **23**(37): 4720-4728.
51. He, H.K., Li, W.W., Zhong, M.J., Konkolewicz, D., Wu, D.C., Yacatto, K., Rappold, T., Sugar, G., David, N.E., and Matyjaszewski, K., *Reversible CO<sub>2</sub> Capture with Porous Polymers Using the Humidity Swing*. *Energy & Environmental Science*, 2013. **6**(2): 488-493.
52. Wang, T., Lackner, K.S., and Wright, A., *Moisture Swing Sorbent for Carbon Dioxide Capture from Ambient Air*. *Environmental Science & Technology*, 2011. **45**(15): 6670-6675.
53. Wang, T., Lackner, K.S., and Wright, A.B., *Moisture-Swing Sorption for Carbon Dioxide Capture from Ambient Air: A Thermodynamic Analysis*. *Physical Chemistry Chemical Physics*, 2013. **15**(2): 504-514.
54. Morcombe, C.R. and Zilm, K.W., *Chemical Shift Referencing in MAS Solid State NMR*. *Journal of Magnetic Resonance*, 2003. **162**(2): 479-486.

55. Stueber, D., Mehta, A.K., Chen, Z.Y., Wooley, K.L., and Schaefer, J., *Local Order in Polycarbonate Glasses by  $^{13}\text{C}\{^{19}\text{F}\}$  Rotational-Echo Double-Resonance NMR*. Journal of Polymer Science Part B-Polymer Physics, 2006. **44**(19): 2760-2775.
56. Gullion, T., Baker, D.B., and Conradi, M.S., *New, Compensated Carr-Purcell Sequences*. Journal of Magnetic Resonance, 1990. **89**(3): 479-484.
57. Gullion, T. and Schaefer, J., *Elimination of Resonance Offset Effects in Rotational-Echo, Double-Resonance NMR*. Journal of Magnetic Resonance, 1991. **92**(2): 439-442.
58. Weldeghiorghis, T.K. and Schaefer, J., *Compensating for Pulse Imperfections in REDOR*. Journal of Magnetic Resonance, 2003. **165**(2): 230-236.
59. Sharma, B.D., *Sodium Bicarbonate and Its Hydrogen Atom*. Acta Crystallographica, 1965. **18**: 818-&.
60. Lackner, K.S., *Washing Carbon out of the Air*. Scientific American, 2010. **302**(6): 66-71.
61. Mata, T.M., Martins, A.A., and Caetano, N.S., *Microalgae for Biodiesel Production and Other Applications: A Review*. Renewable & Sustainable Energy Reviews, 2010. **14**(1): 217-232.
62. Brennan, L. and Owende, P., *Biofuels from Microalgae-a Review of Technologies for Production, Processing, and Extractions of Biofuels and Co-Products*. Renewable & Sustainable Energy Reviews, 2010. **14**(2): 557-577.
63. Bomgardner, M.M., *Algae Plans Bloom*. Chemical & Engineering News, 2011. **89**(29): 19-20.
64. Haag, A.L., *Algae Bloom Again*. Nature, 2007. **447**(7144): 520-521.
65. Lehmann, J., *A Handful of Carbon*. Nature, 2007. **447**(7141): 143-144.